Title

Numerical Simulations of Bubble Dynamics and Heat Transfer in Pool Boiling--Including the Effects of Conjugate Conduction, Level of Gravity, and Noncondensable Gas Dissolved in the Liquid

Author

Aktinol, Eduardo

Publication Date

2014

UNIVERSITY OF CALIFORNIA

Los Angeles

Numerical Simulations of Bubble Dynamics and Heat Transfer in Pool Boiling—Including the Effects of Conjugate Conduction, Level of Gravity, and Noncondensable Gas Dissolved in the Liquid

A dissertation submitted in partial satisfaction of the
requirements for the degree Doctor of Philosophy
in Mechanical Engineering

by

Eduardo Aktinol

2014

ABSTRACT OF THE DISSERTATION

Numerical Simulations of Bubble Dynamics and Heat Transfer in Pool Boiling—Including the Effects of Conjugate Conduction, Level of Gravity, and Noncondensable Gas Dissolved in the Liquid

by

Eduardo Aktinol
Doctor of Philosophy in Mechanical Engineering
University of California, Los Angeles, 2014
Professor Vijay K. Dhir, Chair

Due to the complex nature of the subprocesses involved in nucleate boiling, it has not been possible to develop comprehensive models or correlations despite decades of accumulated data and analysis. Complications such as the presence of dissolved gas in the liquid further confound attempts at modeling nucleate boiling. Moreover, existing empirical correlations may not be suitable for new applications, especially with regards to varying gravity level. More recently, numerical simulations of the boiling process have proven to be capable of reliably predicting bubble dynamics and associated heat transfer by showing excellent agreement with experimental data.

However, most simulations decouple the solid substrate by assuming constant wall temperature. In the present study complete numerical simulations of the boiling process are performed—including conjugate transient conduction in the solid substrate and the effects of dissolved gas in the liquid at different levels of gravity. Finite difference schemes are used to discretize the governing equations in the liquid, vapor, and solid phases. The interface between liquid and vapor phases is tracked by a level set method. An iterative procedure is used at the interface between the solid and fluid phases.

Near the three-phase contact line, temperatures in the solid are observed to fluctuate significantly over short periods. The results show good agreement with the data available in the literature. The results also show that waiting and growth periods can be related directly to wall superheat. The functional relationship between waiting period and wall superheat is found to agree well with empirical correlations reported in the literature. For the case of a single bubble in subcooled nucleate boiling, the presence of dissolved gas in the liquid is found to cause noncondensables to accumulate at the top of the bubble where most condensation occurs. This results in reduced local saturation temperature and condensation rates. The numerical predictions show reasonable agreement with the results from experiments performed at microgravity. For nucleate boiling at microgravity the simulations predict a drastic change in vapor removal pattern when compared to Earth normal gravity. The predictions match well with experimental results. However, simulated heat transfer rates were significantly under-predicted.

The dissertation of Eduardo Aktinol is approved.

Adrienne Lavine

Xiaolin Zhong

Stanley Osher

Vijay Dhir, Committee Chair

University of California, Los Angeles

2014

Table of Contents

List of Figures

List of Tables

Nomenclature

A = dispersion constant

c_p = thermal capacity

C_g = mass fraction of gas

d_c = cavity depth

f = bubble release frequency

$\mathbf{g}$ = gravity vector

h = grid spacing

h_{fg} = latent heat of vaporization

H = Heaviside function

H_g = Henry's law coefficient

Ja = Jakob number

k = thermal conductivity

l_0 = characteristic length

L = thickness of solid

$\vec{m}$ = evaporation/condensation rate

M = molar mass

N_a = active nucleation site density

Nu = Nusselt number

p = pressure

q = heat flux

r = radial coordinate

r_c = cavity radius

R = radial size of domain

$\bar{R}$ = universal gas constant

R_0 = radius of dry region beneath bubble

R_1 = radial location of liquid vapor interface at $y = h/2$

Ra = Rayleigh number

t = time

t_0 = characteristic time

T = temperature

$\vec{u}$ = velocity vector

u_0 = characteristic velocity

$\dot{V}_{micro}$ = evaporation rate in microlayer

ΔV_{micro} = vapor side control volume

x_g = mole fraction of gas

y = vertical coordinate

Y = vertical size of domain

Greek symbols

α = thermal diffusivity

β = coefficient of thermal expansion

δ = microlayer thickness

δ_t = thermal boundary layer thickness

δ^2 = central difference operators

ϕ = level set function

φ = contact angle

κ = interface curvature

μ = kinematic viscosity

ρ = density

σ = surface tension

Subscripts

0 = characteristic value

b = bubble

d = departure

e = earth

g = growth

i, j = computational indices

int = interface

l = liquid

m = mixture

ref = reference value

s = solid

sat = saturation

v = vapor

w = waiting or wall

Superscripts

n = old time step

n+1 = new time step

T = transpose

Acknowledgments

I would like to extend my sincere gratitude to Professor Dhir for his patience, his able guidance, and for providing the necessary financial support through NASA's microgravity fluid physics research program.

Vita

B.S., Mechanical Engineering, Winter 2008
University of California, Los Angeles

M.S., Mechanical Engineering, Spring 2013
University of California, Los Angeles

Journal Publications

Nam, Y., Aktinol, E., Dhir, V.K., and Ju, Y.S., "Single bubble dynamics on a superhydrophilic surface with artificial nucleation sites." International Journal of Heat and Mass Transfer, 54(7), 1572-1577. (2011).

Aktinol, E., and Dhir, V. K., "Numerical simulation of nucleate boiling phenomenon coupled with thermal response of the solid." Microgravity Science and Technology, 24(4), 255-265. (2012).

Dhir, V. K., Warrier, G. R., Aktinol, E., Chao, D., Eggers, J., Sheredy, W., and Booth, W., "Nucleate Pool Boiling Experiments (NPBX) on the International Space Station." Microgravity Science and Technology, 24(5), 307-325. (2012).

Dhir, V.K., Warrier, G.R., Aktinol, E., "Bubble dynamics during pool boiling under microgravity conditions," Computational Thermal Sciences, 4 (6): 525–538 (2012).

Dhir, V. K., Warrier, G. R., and Aktinol, E., "Numerical Simulation of Pool Boiling: A Review." Journal of Heat Transfer, 135(6), 061502. (2013).

Aktinol, E., Warrier, G.R., and Dhir, V.K., "Single bubble dynamics under microgravity conditions in the presence of dissolved gas in the liquid." Submitted: International Journal of Heat and Mass transfer. (2014).

Conference Publications

Aktinol, E., Dhir, V.K., "Numerical Simulation of Nucleate Boiling Phenomenon Coupled With Thermal Response of the Solid." Keynote presented at Fifth ITT Workshop on Two-Phase Systems for Ground and Space Applications. Kyoto, Japan, (2010).

Aktinol, E., Dhir, V.K., "Numerical Simulation of the Effect of Varying Contact Angle on Thermal Response of the Solid During Nucleate Pool Boiling." Poster presented at Sixth ITT

Workshop on Two-Phase Systems for Ground and Space Applications. Cava de' Tirreni, Italy (2011).

Dhir, V.K., Warrier, G.R., Aktinol, E., Chao, D., Eggers, J., Sheredy, W., and Booth, W., "Nucleate Pool Boiling Experiment (NPBX) on the International Space Station (ISS)." Presented at Sixth International Conference on Two Phase Systems for Ground and Space Applications, Cava de'Tirreni, Italy (2011).

Dhir, V. K., Warrier, G. R., Aktinol, E., Chao, D. F., Sheredy, W., Eggers, J., and Booth, W., "Observations on ISS of Bubble Dynamics during Boiling." 50th AIAA Aerospace Sciences Meeting, (2012).

Aktinol, E., Warrier, G.R., and Dhir, V.K., "Single Bubble Dynamics Under Microgravity Conditions." Presented at 29th American Society for Gravitational and Space Research and 5th International Symposium for Physical Sciences in Space. Orlando, Florida, USA (2013).

1 Introduction

Heat transfer processes are prevalent in engineering applications. Due to its efficacy, phase change heat transfer is ideal for applications that demand substantial heat dissipation. Although complex in nature, the versatile process of boiling has proven to be particularly useful. A fundamental understanding of the process is greatly desirable and phase change heat transfer has thus been studied extensively through experimental investigations over the past several decades, and more recently through numerical analysis. However, because of the complexity of the processes involved, a fully mechanistic model capable of predicting the desired engineering parameters such as heat transfer coefficients has not yet been developed and engineering design involving boiling phase change still relies almost exclusively on experimental correlations.

1.1 Boiling regimes

A typical version of the boiling curve, originally introduced by Nukiyama (1934), is shown in Figure 1.1 as illustrated by Ghiaasiaan (2008). It plots wall heat flux as a function of wall superheat (defined as wall temperature minus saturation temperature) and identifies the different boiling regimes observed at different applied wall heat fluxes. In the first region, at low wall superheat and heat flux, the energy supplied is not enough to initiate nucleation. In this region, energy is removed from the wall through simple diffusion. As the temperature of the liquid adjacent to the wall increases, differences in liquid density due to temperature variations lead to what is referred to as natural convection. As the heat flux is increased and the wall temperature increases, eventually a point is reached where bubbles begin to nucleate and grow at the heater surface. This regime of isolated bubbles nucleating, growing, and eventually departing is what is known as partial nucleate boiling. As wall heat flux and temperature increase further, fully developed nucleate boiling is achieved. In this regime, the formerly isolated bubbles grow larger and at more locations until they begin to merge with each other vertically to form vapor columns and laterally to form large mushroom-shaped bubbles. Point C on the boiling curve marks what is usually referred to as the critical heat flux or maximum heat flux during nucleate boiling. Further increase in wall heat flux results in more lateral mergers and the formation of intermittent vapor films that separate the liquid from the solid wall. In contrast to the previous trend where wall heat flux increased with increasing wall temperature, when a vapor film forms, the wall temperature increases drastically as the heat transfer rates drop fast. This chaotic regime of growing and collapsing films is usually referred to as transition boiling because it marks the evolution from fully developed nucleate boiling to the final regime known as film boiling. In film boiling the wall is temperature is high enough that the previously intermittent film can be sustained. The positive correlation between wall temperature and heat flux returns but the heat transfer coefficient is much smaller compared to that of nucleate boiling.

The regime of most interest to the majority of engineering applications is nucleate boiling because high heat transfer coefficients are attainable at relatively low temperatures. Therefore, a fundamental understanding of all the different processes involved in nucleate boiling is essential. The ability to accurately predict heat transfer coefficients for any fluid and general conditions is also crucial. Reflecting the engineering interest in nucleate boiling and boiling in general, over the past several decades extensive research has been carried out to correlate the wall heat flux with other relevant parameters. Although the correlations tend to fit the experimental data well, they are always limited in their applicability because the conditions of interest such as working fluid or heater geometry may not fit exactly with the original experimental conditions.

In the next few sections, a brief review of models and theory regarding the cycle of bubble nucleation, growth, and departure during nucleate pool boiling is provided.

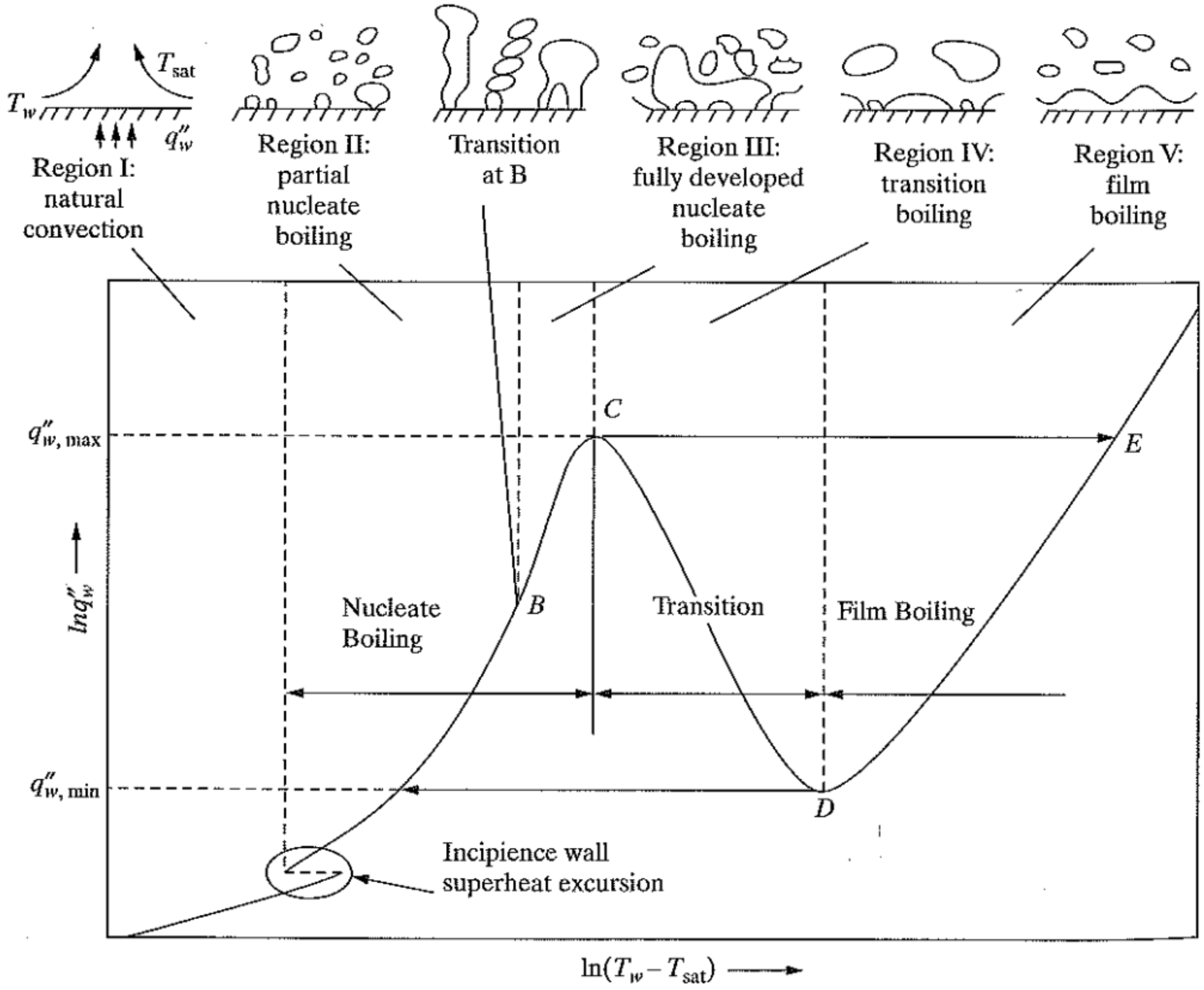

Figure 1.1 Typical boiling curve and associated regimes (Ghiaasiaan, 2008).

1.2 Heterogeneous bubble nucleation and active nucleation sites

Microscopic defects such as cavities and crevices found on solid surfaces may trap air when submerged in a liquid. These pockets of trapped air become the nuclei that provide interfaces through which superheated liquid can evaporate. This phenomenon is referred to as heterogeneous bubble nucleation and is the means by which partial nucleate boiling occurs on a heated solid surface. Thus, characterization of partial nucleate boiling for a given solid-fluid combination is dependent on gas entrapment in the microscopic defects on the solid surface. Some mechanistic models for gas entrapment have been developed and reported in the literature.

The geometric size and shape of a given surface defect, combined with the wetting characteristics of the liquid-solid combination, determine whether gas will be trapped when the surface is submerged in the liquid. The case of a cylindrical cavity is illustrated in Figure 1.2. In this case, the criterion for gas entrapment is obtained simply by the geometry of the cavity combined with the advancing contact angle at the fluid-solid interface. The criterion can be written as,

$$\tan\varphi > \frac{2r_c}{d_c} \tag{1}$$

where r_c is the radius of the cavity and d_c is the cavity depth. Gas entrapment is more complex, however, for more complex cavity geometries such as reentrant cavities. Wang and Dhir (1993) developed a criterion for the entrapment of gas in a cavity of arbitrary geometry in a uniform temperature field based on an analysis of Helmholtz free energy. The criterion is given as

$$\varphi > \psi_{\min} \tag{2}$$

where $\psi_{\min}$ is the minimum cavity side angle defined as the mouth angle for spherical and conical cavities. For sinusoidal cavities the minimum cavity side angle as defined by the authors lies inside the cavity.

Once a gas entrapment criterion has been established, the next parameter of interest for a mechanistic modeling of partial nucleate boiling is the minimum superheat required to initiate bubble growth. Hsu (1962) proposed that, for a nucleus to grow, the embryo must be surrounded by liquid that is everywhere hotter than the saturation temperature corresponding to the pressure inside the bubble. For illustration purposes, the case shown in Figure 1.3 of a chopped sphere on a cylindrical cavity will be analyzed in the context of Hsu's criterion. In this case, the bubble height and bubble radius can both be related to the cavity radius as,

$$y_b = c_1 r_c \tag{3}$$

$$r_b = c_2 r_c \tag{4}$$

where

$$c_1 = \left(1 + \cos\varphi\right) / \sin\varphi \tag{5}$$

$$c_2 = 1 / \sin\varphi \tag{6}$$

Due to the surface tension at the liquid-vapor interface, the pressure inside the bubble is higher than that in the surrounding liquid. The pressure difference is given by the Young-Laplace equation ($\Delta p = 2\sigma / r_b$). The corresponding saturation temperature inside the bubble can be approximated using the Clausius-Clapeyron equation,

$$T_b = T_{sat} + \frac{2\sigma T_{sat}}{r_b \rho_v h_{fg}} \tag{7}$$

If the temperature drop in the thermal boundary layer adjacent to the wall is assumed to be linear, the temperature profile can be expressed as,

$$T = T_l + \left(T_w - T_l\right)\left(1 - \frac{y}{\delta_t}\right) \tag{8}$$

Combining Eqs. (3) through (8) with Hsu's criterion (which states that $T|_{y=y_b} \geq T_b$), it can be shown that,

$$r_{c,\min},\ r_{c,\max} = \frac{\delta_t\left(T_w - T_{sat}\right)}{2c_1\left(T_w - T_l\right)}\left[1 \mp \sqrt{1 - \frac{8c_1}{c_2}\frac{\left(T_w - T_l\right)T_{sat}\sigma}{\left(T_w - T_{sat}\right)^2 \delta_t \rho_v h_{fg}}}\right] \tag{9}$$

where the thermal boundary layer thickness, δ_t, can be approximated as $\delta_t = k_l / h_{NC}$ (where h_{NC} is the natural convection heat transfer coefficient for the liquid).

Therefore, according to Hsu's criterion, for a given wall temperature, T_w, and bulk liquid temperature, T_l, only cavities in the range of $r_{c,\min} \leq r_c \leq r_{c,\max}$ will actually result in growing bubbles. However, the criterion is conservative, as noted by Howell and Siegel (1967), since the temperature requirements imposed are higher than what they measured experimentally. The authors provided less conservative criteria for bubble growth based on the argument that evaporation need not occur throughout the bubble interface but that the net heat exchange between the bubble and the surrounding liquid should be in favor of bubble growth. Wang and Dhir (1993) provide a minimum superheat required to initiate nucleation based on the stability of the liquid-vapor interface of preexisting nuclei for spherical cavities. The criterion is given as

$$\Delta T_w = \frac{4\sigma T_{sat}}{\rho_v h_{fg} D_c} K_{\max} \tag{10}$$

where $K_{\max}$ is the maximum value attained by what the authors define as a nondimensional modified curvature. $K_{\max}$ is given by

$$
\begin{aligned}
K_{\max} &= 1 \qquad \varphi \le 90^{\circ} \\
&= \sin\varphi \quad \varphi > 90^{\circ}
\end{aligned}
\tag{11}
$$

More recently, Basu et al. (2002) generalized minimum superheat criterion by proposing that the minimum wall superheat required diminishes as the wettability increases. The form remains the same as in Eq. (10) but the factor accounting for wettability is included with the cavity diameter as follows

$$\Delta T_w = \frac{4\sigma T_{sat}}{\rho_v h_{fg} D_c^0 F} \tag{12}$$

where D_c^0 is the smallest cavity diameter to nucleate based on Hsu's criterion explained previously, and the function F is given by

$$
\begin{aligned}
D_c^0 &= \left[\frac{8\sigma T_{sat} k_l}{\rho_v h_{fg} q_w}\right]^{1/2} \\
F &= 1 - \exp\left[-\left(\frac{\pi\varphi_s}{180}\right)^3 - 0.5\left(\frac{\pi\varphi_s}{180}\right)\right]
\end{aligned}
\tag{13}
$$

Note that, as the static contact angle, φ_s, approaches zero all cavities will be flooded so the function F also approaches zero. On the other hand, for a static contact angle of 90°, the function F is equal to 1.

After gas entrapment and nucleus growth are established, the last parameter of interest in heterogeneous nucleation is the number density of nucleation sites on the surface. However, due to the fact that the number density depends on factors such as surface material, surface finish, and level of oxidation or contamination, this represents one of the toughest challenges when it comes to the mechanistic modeling of nucleate boiling. Magrini and Nannei (1975) studied the effects of both the wall thickness and the thermal properties of different solids on nucleate boiling. They concluded that both parameters strongly influence nucleation site density. Further complications arise due to interactions between neighboring sites. The bubble growth pattern at neighboring sites during nucleate pool boiling of water on a copper surface was studied Sultan and Judd (1983). The authors found that the elapsed time between the start of bubble growth at two neighboring sites was a function of the distance separating the two sites. They proposed that this behavior is a consequence of the thermal diffusion in the heater substrate in the immediate vicinity of the boiling surface. As reported later by Judd and Chopra (1993), interactions lead to activation of inactive sites and deactivation of active sites.

Despite the difficulties involved in predicting active site density, models and empirical correlations exist and are generally given in the following form

$$N_a \sim \Delta T^m \tag{14}$$

where the exponent, *m*, varies from 2 to 6. Wang and Dhir (1993) provide a relationship in the form of Eq. (14) and more recently Basu et al. (2002) provided an empirical correlation using the same contact angle dependence. The number of sites per square centimeter is given by

$$\begin{aligned} N_a &= 3.4\times10^{-1}\left[1-\cos\left(\varphi_s\right)\right]\Delta T_w^{2.0} \qquad \Delta T_{w,ONB} < \Delta T_w < 15^\circ \\ N_a &= 3.4\times10^{-5}\left[1-\cos\left(\varphi_s\right)\right]\Delta T_w^{5.3} \qquad \Delta T_w \geq 15^\circ \end{aligned} \tag{15}$$

where φ_s is the static contact angle in degrees. The authors report that most of the data are correlated within 40 percent.

Therefore, although mechanistic models have been developed to predict active nucleation site density during nucleate boiling, it is clear that a fully mechanistic prediction remains a challenge. It is also worth noting that, although mechanistic models exist for gas entrapment and bubble nucleus growth, these models do not account for the possibility of thermal interaction between neighboring sites. This means that, even if the heated surface is fully characterized such that all defects and their geometries are known well enough to predict whether gas can be trapped and at what temperature each defect would become activated, the interaction between neighboring sites has yet to be modeled.

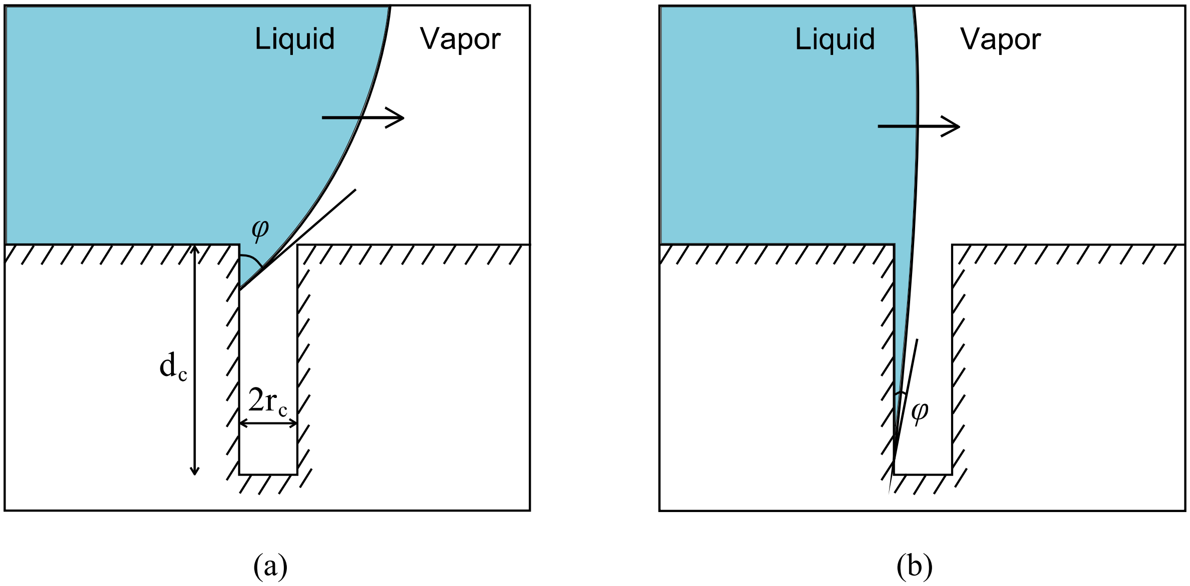

Figure 1.2 Schematic representation of vapor or gas entrapment in a cylindrical cavity for contact angles of (a) 60^o, and (b) 10^o.

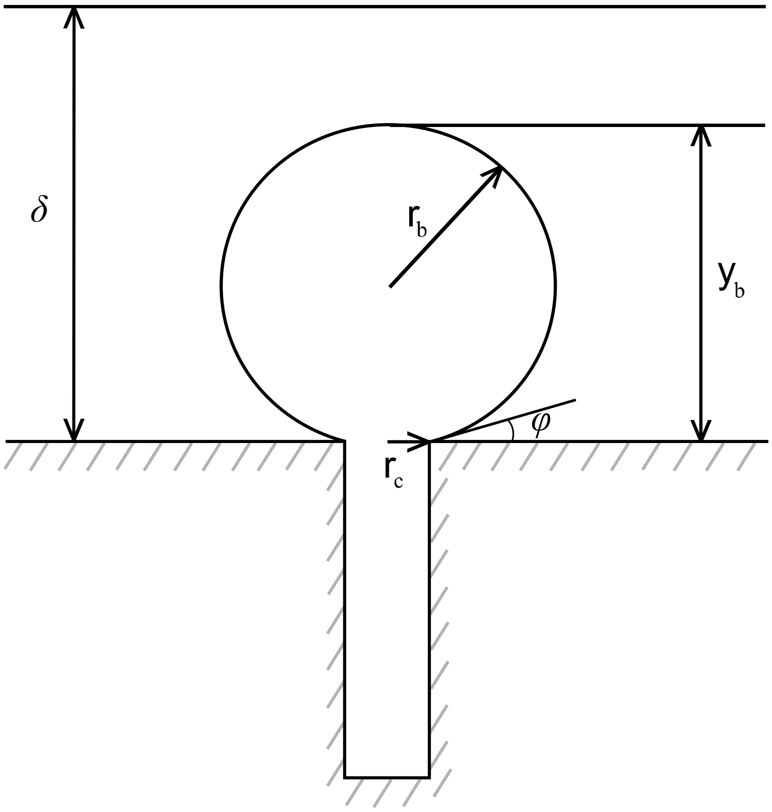

Figure 1.3 Schematic representation of a chopped spherical bubble embryo atop a cylindrical cavity.

1.3 Bubble Growth Period and Departure Diameter

With gas entrapment and minimum temperature to initiate bubble growth established, the next fundamental part of the mechanisms involved in nucleate boiling is the growth and departure of bubbles. Several authors have attempted to model bubble growth analytically. Plesset and Zwick (1954) and Forster and Zuber (1954) developed solutions capable of predicting growth rates for a spherical bubble surrounded by a superheated liquid with uniform temperature. For a more realistic prediction, Mikic et al. (1970) derived an analytical solution that accounts for the nonuniform temperature around a bubble growing while attached to a wall as well as its nonspherical shape. However, their model assume that all of the vapor production occurs around the bubble as it is surrounded by superheated liquid. The possible existence of a thin layer of liquid located between the bubble and the heated surface (microlayer) is not considered. Moore and Mesler (1961) showed experimentally that local wall temperature fluctuations can be significant during high heat flux nucleate boiling (up to 17 ^{o}C in 2 ms) and attributed them to microlayer evaporation. Cooper and Lloyd (1969) observed similar behavior in their experiments even for isolated vapor bubbles. Lay and Dhir (1995) developed a model for describing the liquid flow in an evaporating interface during nucleate boiling which is capable of predicting microlayer shape and evaporative heat flux.

Despite not accounting for microlayer evaporation, the models for bubble growth described can generally predict bubble growth rates fairly well. As a bubble that is attached to a wall grows, it is subjected to a number of different forces. Bubble departure occurs when forces that tend to dislocate the bubble overcome the forces that resist bubble detachment. The main forces that tend to dislocate the bubble are buoyancy and the wake left behind by the preceding bubble. Conversely, surface tension, drag, and inertia are the main forces resisting the detachment of the bubble from the surface. Accounting for only buoyancy on one hand and surface tension on the other, Fritz (1935) developed a correlation for the diameter of the bubble at departure.

$$D_d = 0.0208\theta\sqrt{\frac{\sigma}{g\Delta\rho}} \tag{16}$$

where the contact angle is in degrees. Many of the correlations that attempt to account for other forces need information about the bubble growth rate. As a simple modification of Fritz's correlation, Cole and Shulman (1966) proposed the following

$$D_d = 0.0208\theta\sqrt{\frac{\sigma}{g\Delta\rho}}\left[1+0.0025\left(\frac{dD_b}{dt}\right)^{3/2}\right] \tag{17}$$

where the bubble growth rate, dD_b/dt is in millimeters per second. For further examples and reviews of proposed bubble departure diameter correlations, see Hsu and Graham (1986) and Carey (2008). The models developed for the prediction of bubble departure diameters also produce acceptable results. However, they remain semi-empirical in nature, requiring the use of coefficients and/or exponents that can only be obtained through experiments.

1.4 Waiting Period and Bubble Release Frequency

The departing bubble displaces the superheated boundary layer and cooler liquid from the ambient surroundings rushes in to replenish the space previously occupied by the vapor. Models for waiting period were developed assuming that the next bubble would begin to grow once the superheated boundary layer was reestablished. The development of the thermal layer was modeled by Hsu and Graham (1961) as simple transient conduction in a slab with thickness equal to that of the original thermal layer. Han and Griffith (1965) used the solution for one-dimensional transient conduction into a semi-infinite medium to obtain the time-dependent thermal layer thickness. The authors also assumed that, for initiating bubble growth, the mean temperature of the thermal layer surrounding the nucleus must be above the temperature of the vapor in the nucleus. When combined, the time-dependent thermal layer thickness and the criterion for growth lead to the following expression for the waiting period

$$t_w = \frac{9}{4\pi\alpha_l}\left\{\frac{\left(T_w - T_\infty\right)r_c}{T_w - T_{sat}\left[1+\left(2\sigma/r_c\rho_v h_{fg}\right)\right]}\right\}^2 \tag{18}$$

However, these models do not take into account the thermal interaction between the fluid and the solid. As will be shown, cooling of the solid substrate can be substantial and therefore conjugate conduction in the solid plays an important role in the determination of waiting time.

Waiting period is often referred to indirectly through the frequency of the bubble growth and release cycles. The growth period is defined as the time taken for a bubble to grow from it's nucleation to its departure and the waiting period is defined as the time taken for another bubble to nucleate after the previous one has departed. The bubble release frequency, therefore, is the inverse of the sum of the growth and waiting periods.

$$f = \frac{1}{t_g + t_w} \tag{19}$$

Predictions of bubble release frequency are often associated with the bubble departure diameter. Zuber (1963) suggested the following relation based on an analogy between the bubble release process and natural convection

$$fD_d = 0.59\left(\frac{\sigma g \Delta\rho}{\rho_l^2}\right)^{1/4} \tag{20}$$

Mikic and Rohsenow (1969) developed a model for heat-transfer-controlled growth of a bubble in a non-uniform temperature field near a heated surface. Based on their model they evaluated the waiting and growth times and derived the following relation for the bubble frequency

$$f^{1/2}D_d = \left(\frac{4}{\pi}\right) Ja\sqrt{3\pi\alpha_l}\left[\left(\frac{t_g}{t_w + t_g}\right)^{1/2} + \left(1 + \frac{t_g}{t_w + t_g}\right)^{1/2} - 1\right] \tag{21}$$

where *Ja* is the Jakob number defined as

$$Ja = \frac{\rho_l c_{pl}\left[T_\infty - T_{sat}\left(p_\infty\right)\right]}{\rho_v h_{fg}} \tag{22}$$

Note that, in this case, growth and waiting periods have to be known in order to obtain frequency.

It is apparent that the models remain incomplete and cannot predict bubble dynamics without making a number of simplifying assumptions that have been shown to be unjustifiable. Furthermore, none of the models described take into account the local cooling of the heater substrate. As mentioned in the previous section, it was shown by Moore and Mesler (1961) that surface temperature fluctuations can be significant during fully developed nucleate boiling. Rogers and Mesler (1964) refined the same experiments to show that similar surface temperature fluctuations exist even under the low heat flux conditions encountered during partial nucleate boiling. The authors showed visually through the use of high speed photography that the temperature drops observed accompany the motion of the three phase line as the bubble base expands then shrinks during bubble growth.

Instead of modeling the waiting time based on transient conduction in the thermal boundary layer of the fluid, an alternative approach is to model it based on transient conduction inside the heater substrate. With this approach, nucleation criteria such as those introduced in section 1.2 could be used in determining the waiting period between successive bubbles. However, this significantly increases the complexity of the model by requiring the problem of conjugate conduction in the solid to also be solved.

1.5 Bubble Growth in Microgravity

As explained previously in section 1.3, buoyancy is one of the main forces tending to dislocate a growing bubble from the surface it is attached to. Buoyancy force is directly related to the gravitational acceleration. Therefore, under reduced gravity conditions, buoyancy force is also reduced and mechanistic models predict larger bubble departure diameters. The correlation given by Fritz (Eq. (16)), for example, predicts bubble departure diameter to vary as $D_d \propto \left(1/\sqrt{g}\right)$. In order to verify that the model predictions are correct, some experimental data is required.

Since the 1960's, various investigators have reported results from nucleate pool boiling experiments under microgravity conditions, some of which will be briefly reviewed in section 1.7. However, knowledge of single bubble dynamics and its dependence on gravity can be very instructive in understanding the boiling mechanism under microgravity conditions. Qiu et al. (2000) performed experiments on parabolic flights that focused on single bubble dynamics. They found that under reduced gravity conditions the growth period was longer and the bubble departure diameter larger than at earth normal gravity. It was found that bubble departure diameter can be approximately related to gravitational acceleration through the relation $D_d \propto \left(1/\sqrt{g}\right)$ and that the growth period scales as $t_g/t_{g_e} = \left(g/g_e\right)^{-1.05}$. The remarkable agreement with mechanistic models should be noted. However, these relations are still only experimentally verified at gravity levels ranging from $0.01g_e \le g \le 1.8g_e$.

More recently, Dhir et al. (2012) reported results of the Nucleate Pool Boiling Experiment (NPBX) on the International Space Station (ISS) which included single bubble dynamics as well as nucleate boiling heat transfer. On the ISS the gravity level was 4-5 orders of magnitude smaller than on parabolic flights, 2-3 orders of magnitude smaller than on sounding rockets and drop towers, and comparable to that encountered in space shuttle orbital missions. Additionally, the duration of the experiments performed on the ISS was significantly longer than the previously used reduced gravity environments. Unfortunately, the boiling chamber size used in the experiments was too small to allow the bubbles to grow large enough to reach the departure diameter predicted by the simulations. Therefore, the validity of the mechanistic models for bubble departure diameter could not be experimentally verified under such a low gravity level.

1.6 Effects of noncondensables

The deterioration of condensation heat transfer due to the presence of noncondensable gases was quantified by Othmer (1929). The author investigated the simple case of condensation on a cooled horizontal cylinder of pure steam and of different mixtures ratios of steam and air. The effect of mass fraction of air in the bulk fluid was quantified. Also quantified was the effect of temperature difference between condensing surface and bulk fluid. Condensation heat transfer rate deterioration of over 50% was found for cases where the bulk mass fraction of air was less than 0.05.

Sparrow and Lin (1964) mathematically formulated the problem of condensation heat transfer on a cooled vertical wall in the presence of a noncondensable gas obtaining self-similar boundary layer solutions. The problem was simplified by assuming that the thickness of the condensate layer was known, and the resulting differential equations were integrated to simplify the numerical solution procedure. The equations were solved for parametrically varied values of the temperature of the condensate interface. Minkowycz and Sparrow (1966) extended the solutions to include the effect of variable properties. The authors showed that the deterioration of condensation heat transfer rate can be predicted with satisfactory accuracy without utilizing any empirical data.

In the context of subcooled nucleate pool boiling, the presence of noncondensable gases dissolved in the fluid may lead to an analogous accumulation of gas. For a bubble growing while attached to the heater surface, the noncondensable gases may be expected to accumulate near the interface where condensation is occurring in the same manner that it accumulates near the film during film condensation. Wu and Dhir (2011) numerically studied the effects of noncondensable gases during subcooled nucleate pool boiling under various gravity levels. It was assumed that, for a bubble growing out of a cavity with trapped air, the initial mass fraction of noncondensable gas inside the bubble is large (up to 0.4). As the bubble grows, the mass fraction of air inside the bubble goes down due to the fact that the mass fraction of air dissolved in the evaporating liquid is much lower than the initial mass fraction of air inside the bubble. Nevertheless, due to condensation occurring predominantly in the top half of the bubble, there exists a gradient in the mass fraction of air inside the bubble. This gradient leads to changes in surface tension along the interface of the bubble. Although slight changes in bubble growth rates and interface heat transfer were reported, the authors highlighted the effect of variable surface tension leading to capillary flow around the bubble interface.

1.7 Nucleate boiling in microgravity

Due to size and weight constraints in space applications, phase change is the preferred mode of heat transfer for applications such as thermal management and power systems. However, the very low gravity conditions encountered in the space station, for example, result in a large reduction in buoyancy, which is one of the main driving forces in pool boiling heat transfer. With a goal of elucidating the scaling of boiling heat transfer with gravity level, several studies have been performed to reconstruct the boiling curve under different levels of reduced gravity ranging from 10^{-2} to 10^{-7} g_e.

Straub (2001) detailed the results of several different experiments exploring the effect of gravity on nucleate pool boiling. These experiments included parabolic flights, ballistic rockets, and space shuttle missions. It was found that critical heat flux deteriorated under reduced gravity, although it was significantly higher than what existing correlations would predict when extrapolated to microgravity. At low heat fluxes, however, heat transfer coefficients were found to be independent of gravitational conditions. It was concluded that the primary heat transfer mechanism during nucleate pool boiling must be unaffected by changing gravitational acceleration and is thus strongly related to the development of the microlayer during bubble growth. The mechanisms that are affected by gravity, on the other hand, include all means by which energy is transported from the surface to the bulk liquid. Under terrestrial conditions, this is driven mainly by buoyancy, while under reduced gravity it is driven by the dynamics of bubble mergers.

During space shuttle flights that provided gravity levels of the order of 10^{-4} g_e, Lee et al. (1997) conducted experiments designed to investigate the effect of gravity on subcooled nucleate pool boiling on a flat plate. Like Straub, they found that critical heat flux was reduced considerably when compared to the identical experiments performed on Earth. However, it was found that for a well wetting fluid such as R-113, the nucleate boiling heat transfer was significantly enhanced in reduced gravity. Different fluids and surface combinations were not explored and it was noted by the authors that changing wetting characteristics could produce different behavior than what was reported.

Oka et al. (1995) performed pool boiling experiments under the reduced gravity conditions obtained during parabolic flights where the gravity level is approximately 100 times less than that on Earth. A transparent heater was used along with a glass plate so that the surface could be observed from below as well as from the side. Three different fluids were used and it was found that critical heat fluxes deteriorate significantly in all cases with a reduction in gravity. However, during experiments with low heat flux, only one fluid—water—showed significant heat transfer deterioration in reduced gravity. The authors used observations on the rear side of the heater to justify the discrepancy, noting that the detachment behavior of large bubbles was different between water and the two organic fluids due to different wettability.

Ohta et al. (1999) performed pool boiling experiments on a flat circular disk made of sapphire glass. The experiments were carried out in a ballistic rocket as well as parabolic flights. The authors observed the same vapor removal patterns seen in the previous studies where a large bubble remains close to the heater surface and acts as a vapor reservoir, sucking in all the smaller bubbles forming and growing on the heated surface. It was concluded that steady state nucleate pool boiling is unattainable at microgravity unless the subcooling is high enough to avoid heater dryout.

Also in parabolic flights, Kim et al. (2002) studied the effect of gravity on nucleate pool boiling by using a microheater array. The fluid used was FC72 and the heated surface was a square with side length of 2.7 mm. The familiar bubble pattern was also observed despite the small heater size. However, due to the small overall heater size, dryout was observed even at high liquid subcoolings. Additionally, at high liquid subcoolings, a rising jet was reported over the large coalesced bubbles. The fluid was degassed until the measured mole fraction of dissolved gas in the liquid was below 1.5 x 10^{-3} but the jet was nevertheless attributed to Marangoni convection driving the flow upwards around the bubble interface. The positive correlation between critical heat flux and gravity was evident for any given experimental conditions and varying gravity levels. It was concluded that, other than the CHF, the boiling heat transfer was independent of subcooling and gravity level.

Zhao et al. (2009) investigated the effects of gravity on nucleate pool boiling heat transfer by conducting experiments on a recoverable satellite. The gravity level was estimated to lie between 10^{-3} to 10^{-5} g_e. Despite the large uncertainty in gravitational acceleration, the mid point of the range estimated is comparable to those obtained in previous sounding rocket experiments. As other investigators reported, when compared to identical conditions at earth normal gravity, the vapor removal pattern was observed to be entirely different, and the critical heat flux was achieved at much lower wall temperatures due to surface dryout.

Kannengieser et al. (2011) also conducted experiments under earth normal gravity conditions and parabolic flights where the gravity level was of the order of 10^{-2} g_e. The authors found results qualitatively similar to those reported by previous investigators. During nucleate pool boiling at low heat flux, comparable heat transfer coefficients were obtained at both gravity levels. However, as the heat flux was increased, the experiments conducted under reduced gravity conditions reached CHF significantly earlier than those under normal gravity conditions. In order to justify the lack of influence of gravity level on heat transfer coefficients, the authors distinguished two boiling regimes: isolated boiling regime and fully developed boiling regime. It was further stated that in the fully developed boiling regime, heat transfer mechanisms in the vicinity of the wall are dominant and are not limited by the vapor removal pattern. During the boiling experiments performed under microgravity conditions, it was found that heat transfer occurred only in the fully developed boiling regime. The authors concluded that, since a reduction in gravity level only affects vapor removal pattern and not heat transfer mechanisms in the vicinity of the wall, it has no effect on heat transfer coefficient. It was also proposed that correlations based on capillary length are unable to predict heat transfer rates in microgravity because they focus primarily on the mechanisms by which vapor is removed from the boiling surface.

Finally, in the aforementioned study by Dhir et al. (2012) nucleate pool boiling experiments were performed at a reduced gravity level of 10^{-7} g_e. The findings are consistent with the rest of the literature regarding the vapor removal patterns and the deterioration of the critical heat flux under reduced gravity. It is also reported that heat transfer coefficients deteriorate under reduced gravity conditions during all other regimes including natural convection, partial nucleate boiling, and fully developed nucleate boiling.

1.8 Numerical simulations of pool boiling

As outlined in the preceding sections, numerous mechanistic and semi-empirical models have been developed to predict nucleate boiling subprocesses. Empirical correlations and mechanistic models also have been developed to predict nucleate pool boiling heat transfer. Despite having been used extensively in the design of engineered systems, the predictive ability of empirical correlations becomes uncertain when applied to new situations. Mechanistic models of nucleate boiling, on the other hand, require knowledge of parameters such as number density of active sites and bubble release frequency. Due to the complexity and coupling of all the subprocesses involved, the development of comprehensive models for nucleate boiling has had limited success. Furthermore, the predictive methods developed have focused almost exclusively on the mechanisms occurring on the fluid side. However, the heat transfer processes occurring on the fluid side are tightly coupled to heat conduction in the solid. For example, bubble waiting time and bubble release frequency are strongly dependent on the temperature distribution in the solid.

Dhir (2006) has proposed the use of complete numerical simulations as an alternate method to predict the boiling curve. New modeling techniques have resulted in high fidelity computer simulations and advances in computing power have allowed for faster calculations with increasing complexity to be performed. Numerical simulations have been shown to be successful in predicting growth rates and departure diameters for single bubbles. They have also been used to predict vertical bubble mergers and formation of vapor columns, as well as lateral bubble mergers and formation of mushroom type bubbles. Finally, heat transfer rates during nucleate and film boiling have also been successfully predicted by numerical simulations.

Son et al. (1999) performed numerical simulations and experiments to study the dynamics and heat transfer associated with a single bubble during nucleate boiling on a horizontal surface. The simulated bubble growth and departure processes were found to agree with experimental results to a high degree of accuracy. With an entirely different approach, Yoon et al. (2001) performed simulations of the single bubble dynamics phenomenon and also obtained experimentally confirmed results.

However, one of the key assumptions that both numerical models share is that the surface temperature is constant in time and uniform in space, thereby completely decoupling the thermal response of the solid surface. This is likely to influence the cyclic behavior of bubble evolution, growth and departure processes. Furthermore, with the constant temperature assumption, the waiting time between successive nucleation of bubbles at a given site cannot be determined and must be specified empirically. This deprives the simulation from being able to predict the dependency of waiting time on wall superheat. Consequently, the prediction of heat transfer rates for various boiling regimes where the waiting time would not remain fixed is severely limited unless waiting time is specified empirically.

Guo and El-Genk (1994) developed a numerical model based on microlayer evaporation that predicts a strong influence of the wall’s thickness and thermal properties on initial bubble growth rates. More recently, Mann et al. (2000) conducted numerical simulations of a single bubble with a wedge-shaped micro region to study the influence that heat conduction in the wall has on nucleate boiling heat transfer. However, in both simulations, the contribution of the induced convection due to bubble growth and detachment is neglected. Likewise, quasi stationary heat transfer is assumed which results in unrealistic estimates of bubble growth and heat transfer.

Kunkelmann and Stephan (2010) performed transient numerical simulations that included the heat transfer between the fluid and solid phases. The authors showed the spatial variation in surface temperature and heat transfer rates but chose to impose the waiting time based on experimental values. Aktinol and Dhir (2012) also used numerical simulations to predict the spatial variation in surface temperature and heat transfer rates, and quantified the dependency of waiting time on different parameters such as wall heat flux, thickness, and thermophysical properties. The effect of contact angle was not explored by the authors.

For a recent and thorough literature review of numerical simulations of all regimes of boiling, please refer to Dhir et al. (2013).

1.9 Objectives

The objectives of this study are summarized in the following list:

- Perform complete numerical simulations of bubble dynamics on a single nucleation site coupled with the thermal response of the supporting horizontal surface.
- Parametrically quantify the dependency of the waiting time, growth period, and heat transfer on the wall's thermal properties, thickness, nucleation superheat, and contact angle.
- Study the dynamics of a single bubble under microgravity conditions including the effects on bubble dynamics of varying pressures, liquid and surface temperatures, and dissolved gas content.
- Perform preliminary three-dimensional numerical simulations with coarse grids to predict vapor removal patterns and nucleate pool boiling heat transfer under microgravity conditions.

2 Numerical Model

The numerical simulation of boiling must be able to account for all the processes involved in order to achieve realistic results. Bubbles must be able to nucleate, grow freely without shape limitations, detach, and float away without restrictions. Evaporation and condensation must be accounted for at the liquid-vapor interface, whether close to the heated wall or not. The induced fluid motion due to the growth and detachment of bubbles must also be accounted for along with the transient heating of the boundary layer after bubble departure. In most experimental setups and practical applications, power to the boiling surface is controlled. Since boiling is an inherently transient process, the fluid side heat flux varies both spatially and temporally resulting in wall temperature fluctuations. This phenomenon must also be captured by the numerical simulations through the solution of conjugate conduction in the solid substrate during bubble growth.

As proposed by Son et al. (1999), when simulating the processes the region of interest is subdivided into micro and macro regions. The solid substrate region is treated separately. The splitting of the computational domain is shown in Figure 2.1. All the three regions are coupled through boundary conditions. The micro region is comprised of the thin layer of liquid located in between the solid substrate and the liquid-vapor interface. Its thickness varies from the order of molecular size at its thinnest to the order of the grid spacing on the macro code (a few microns thick). The shape of the film is obtained by using lubrication theory and the energy supplied by the wall is conducted across the film and used for evaporation. The fluid side macro region contains the liquid and vapor phases. In both phases the complete conservation equations for mass, momentum, and energy are solved. The liquid-vapor interface is tracked through the use of a level set method. Finally, conduction in the solid substrate region is solved to account for the transient fluctuations in surface temperature and heat flux. In the next few sections the assumptions will be listed and the governing equations and boundary conditions will be provided along with the computational procedure implemented.

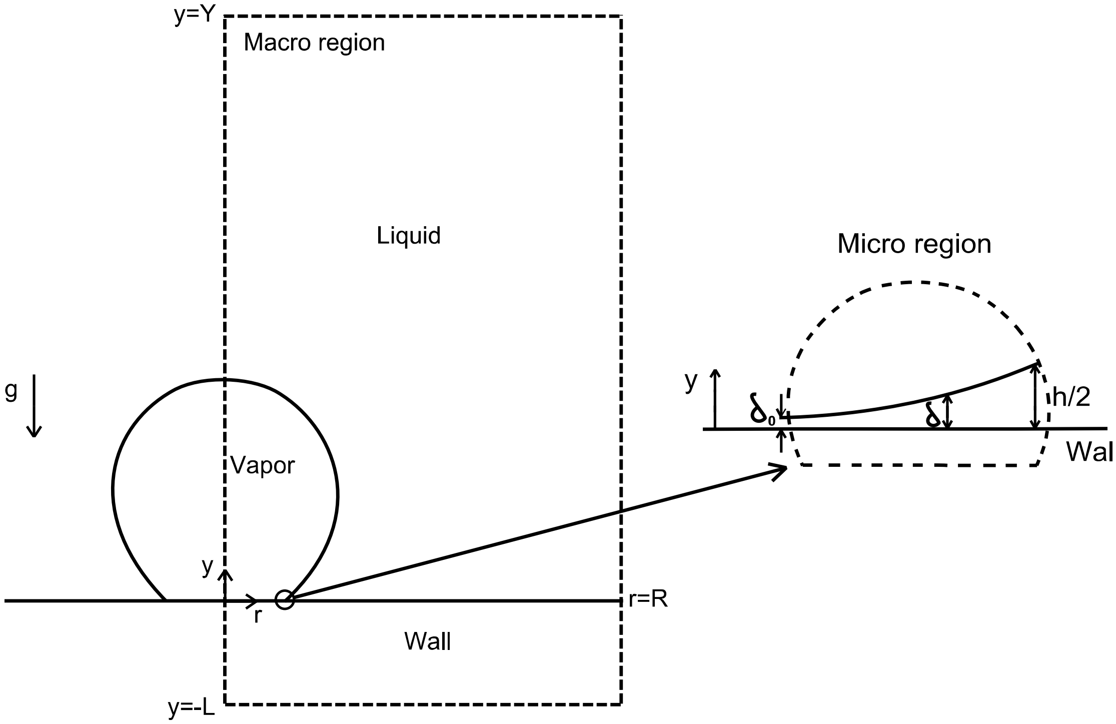

Figure 2.1 Different regions in the computational domain

2.1 Assumptions

In developing and implementing the numerical model the following assumptions were made:

(1) For a single cavity at the origin of the domain, all processes are assumed to be perfectly axisymmetric.

(2) In the solution of the conservation equations for the microlayer, inertia terms are neglected in the momentum equations and convection terms are neglected in the energy equation.

(3) Microlayer heat transfer varies linearly with the wall superheat.

(4) Static contact angles are used in the fluid side macro region.

(5) The flow is laminar.

(6) Although phase change occurs, the flow is incompressible in each individual phase.

(7) In the absence of dissolved gas in the liquid, the liquid-vapor interface in the macro region is assumed to remain at saturation temperature such that surface tension is constant and there is no capillary flow. Surface tension variation is accounted for only in the micro region.

(8) The thermodynamic properties of each individual phase are constant except for the surface tension variation close to the wall in the solution of the microlayer.

2.2 Macro Region

In solving for the macro region, the modified level set formulation is used. The interface separating the liquid and vapor phases is captured by solving the following equation for the level set function, ϕ,

$$\frac{\partial \phi}{\partial t} = -\vec{u}_{int} \cdot \nabla \phi \tag{23}$$

where the interface velocity is given by

$$\vec{u}_{int} = \vec{u} + \frac{\vec{m}}{\rho} \tag{24}$$

and the evaporation/condensation rate, $\vec{m}$, is calculated based on mass conservation at the interface

$$\vec{m} = \rho\left(\vec{u}_{\mathrm{int}} - \vec{u}\right) = k \nabla T / h_{fg} \tag{25}$$

The following level set reinitialization equation is solved until steady state is obtained to ensure that $\left|\nabla \phi\right| = 1$,

$$\frac{\partial \phi}{\partial t} = \frac{\phi_0}{\sqrt{\phi_0^2 + h^2}}\left(1 - \left|\nabla \phi\right|\right) \tag{26}$$

where ϕ_0 is a solution of Eq. (23). The fluid properties are given by

$$\begin{aligned} \rho &= \rho_m + \left(\rho_l - \rho_m\right) H = \rho_v + \rho_g + \left(\rho_l - \rho_v - \rho_g\right) H \\ \mu &= \mu_v + \left(\mu_l - \mu_v\right) H \\ k &= k_v + \left(k_l - k_v\right) H \end{aligned} \tag{27}$$

The mixture density, ρ_m, is the sum of the vapor and gas densities. In the sharp interface model employed here, the Heaviside function (H) is a step function given by,

$$\begin{aligned} H &= 1 \quad \mathit{if}\ \phi > 0 \\ H &= 0 \quad \mathit{if}\ \phi \le 0 \end{aligned} \tag{28}$$

The equations governing conservation of mass, momentum, energy, and species in the macro region are written as,

$$\frac{\partial \rho}{\partial t} + \nabla \cdot \left(\rho \vec{u} \right) = 0 \tag{29}$$

$$\rho \left(\frac{\partial \vec{u}}{\partial t} + \vec{u} \cdot \nabla \vec{u} \right) = -\nabla p + \rho \vec{g} - \rho \beta \left(T - T_{sat} \right) \vec{g} - \sigma \kappa \nabla H + \nabla \cdot \mu \nabla \vec{u} + \nabla \cdot \mu \nabla \vec{u}^{T} \tag{30}$$

$$\rho c_p \left(\frac{\partial T}{\partial t} + \vec{u} \cdot \nabla T \right) = \nabla \cdot k \nabla T \tag{31}$$

$$\begin{aligned} \rho \left(\frac{\partial C_g}{\partial t} + \vec{u} \cdot \nabla C_g \right) &= \nabla \cdot \rho D \nabla C_g \quad \mathit{for} \quad H = 0 \\ C_g &= C_{g,l} \quad \mathit{for} \quad H > 0 \end{aligned} \tag{32}$$

For the cases in which there is dissolved gas in the liquid, the energy conservation equation (Eq. (31)) is only solved in the liquid (*H > 0*). In these cases, the solution of Eq. (32) provides a mass fraction distribution of noncondensable gas inside the bubble. Assuming uniform pressure exists inside the bubble, the distribution of partial pressure of vapor is obtained from the distribution of noncondensable gas. Therefore, it should be noted that, although the energy conservation equation is not solved inside the bubble, due to the presence of the noncondensable gas, local partial pressures of vapor vary and therefore so do local saturation temperatures. Using the same approach employed by Wu and Dhir (2011), the mass conservation equation (29) can be rewritten as,

$$\begin{aligned} \nabla \cdot \vec{u} &= \frac{\vec{m}}{\rho^2} \cdot \nabla \rho + \dot{V}_{micro} = \frac{k \nabla T}{h_{fg} \rho^2} \cdot \nabla \rho + \dot{V}_{micro} && \mathit{for\ condensation} \\ &= \frac{k \nabla T}{h_{fg} \rho^2 \left(1 - C_{g,l} \right)} \cdot \nabla \rho + \dot{V}_{micro} && \mathit{for\ evaporation} \end{aligned} \tag{33}$$

where the term $\left(1-C_{g,l}\right)$ in the denominator accounts for the addition of gas during evaporation assuming that no extra energy is required for release of gas. The term $\dot{V}_{micro}$ is obtained from the microlayer solution as,

$$\dot{V}_{micro} = \int_{R_0}^{R_1} \frac{k_l\left(T_w - T_{\text{int}}\right)}{\rho_m h_{fg} \delta \Delta V_{micro}\left(1-C_{g,l}\right)} rdr \tag{34}$$

where ΔV_{micro} is a vapor-side control volume near the micro region. Another key assumption is that there is no gas concentration gradient in the liquid such that the mass fraction of dissolved gas just outside of the interface is the same as in the bulk liquid (i.e., the species conservation equation is not solved in the liquid).

The boundary conditions for the macro region are given at four sides (see Figure 2.1). They are (i) the axis of symmetry at $r = 0$, (ii) an insulated wall at $r = R$, (iii) a heated wall at $y = 0$, and (iv) an insulated wall at $y = Y$. A small opening at $y = Y$ (5 mm radius beginning at $r = 0$) is included to simulate the opening connecting the test chamber to the bellows (see section 3 Experimental setup). This open boundary is simulated by imposing a known constant pressure and zero velocity gradients. The fluid can flow freely into and out of the chamber through this opening at the top of the computational domain. As such, during bubble growth liquid gets pushed out through the opening and during bubble shrinking liquid flows back in.

2.3 Micro Region

Lay and Dhir (1995) have modeled and solved numerically for the shape of the microlayer using lubrication theory. Following their model, the conservation equations for mass, momentum, and energy are given as

$$\frac{q}{\rho_l h_{fg}} = -\frac{1}{r}\frac{\partial}{\partial r}\int_0^{\delta} r u_l dy \tag{35}$$

$$\frac{\partial p_l}{\partial r} = \mu_l \frac{\partial^2 u_l}{\partial y^2} \tag{36}$$

$$q = \frac{k_l\left(T_w - T_{\text{int}}\right)}{\delta} = h_{ev}\left[T_{\text{int}} - T_v + \frac{\left(p_l - p_v\right)T_v}{\rho_l h_{fg}}\right] \tag{37}$$

where h_{ev} is the evaporation heat transfer coefficient obtained by Wayner (1992) from kinetic theory as

$$h_{ev} = \frac{\left(2M/\pi \bar{R} T_v\right)^{0.5} \rho_v h_{fg}^2}{T_v} \tag{38}$$

and the pressures in the vapor and liquid phases satisfy the following relation

$$p_l = p_v - \sigma\kappa - \frac{A}{\delta^3} + \frac{q^2}{\rho_v h_{fg}^2} \tag{39}$$

where the surface tension, σ, is a function of temperature and A is the dispersion constant in the disjoining pressure. In equation (39), the second term on the right hand side accounts for the capillary pressure, the third term accounts for the disjoining pressure, and the last term accounts for the recoil pressure. The curvature of the interface is given by

$$\kappa = \frac{1}{r}\frac{\partial}{\partial r}\left[r\frac{\partial \delta}{\partial r}\Bigg/\sqrt{1+\left(\frac{\partial \delta}{\partial r}\right)^2}\right] \tag{40}$$

Combining the conservation equations in the microlayer yields a fourth order partial differential equation with respect to the radius, r

$$\delta'''' = f\left(\delta, \delta', \delta'', \delta'''\right) \tag{41}$$

The boundary conditions for the problem are specified at two locations. At the inner radius of the microlayer, $r = R_0$

$$\begin{aligned} &\delta = \delta_0 \\ &\delta' = \delta''' = 0 \end{aligned} \tag{42}$$

where δ_0 is of the order of a molecular size. At the outer radius of the microlayer, $r = R_1$

$$\begin{aligned} &\delta = h/2 \\ &\delta'' = 0 \end{aligned} \tag{43}$$

where $h/2$ is the vertical distance to the first computational node for the level set function in the macro region. The coupling between the macro and micro regions is accomplished through the implementation of the boundary conditions on each region. In order to implement two of the boundary conditions in the micro region, R_1 is required and obtained from the macro code. Likewise, in order to implement the contact angle boundary condition for the level set equation in the macro code, the location of R_0 is required and obtained from the micro code. The apparent contact angle is then defined as

$$\tan\varphi = \frac{0.5h}{R_1 - R_0} \tag{44}$$

The procedure to match the solutions for the macro and micro regions asymptotically is outlined by Son and Dhir (1999).

2.4 Solid Substrate Region

The quantity of interest in the solid region of the computational domain is the transient temperature and associated heat flux. Due to the lack of motion, the energy equation in cylindrical coordinates (assuming axisymmetry exists) reduces to the following

$$\rho c_{ps} \frac{\partial T}{\partial t} = k_s \left[\frac{1}{r} \frac{\partial}{\partial r} \left(r \frac{\partial T}{\partial r} \right) + \frac{\partial^2 T}{\partial y^2} \right] \tag{45}$$

In order to obtain second order accuracy in both space and time, the Crank-Nicolson scheme is used to discretize equation (45).

At the inner boundary corresponding to the origin of the domain, axisymmetry requires that the temperature gradient must be zero. At the outer boundary, perfect insulation is assumed. Thus, in both cases the gradient of the temperature can be written as

$$\frac{\partial T}{\partial r} = 0 \quad \text{at} \quad r = 0, R \tag{46}$$

At the bottom boundary corresponding to the base of the heated solid substrate, a constant heat flux is applied such that

$$k \frac{\partial T}{\partial y} = constant \quad \text{at} \quad y = -L \tag{47}$$

The top boundary corresponding to the surface of the plate is where the coupling between the solid and the fluid side is accomplished. This boundary condition is not only required in order to run the simulation, it is also an area of interest because the surface of the solid is where the highest temperature fluctuations are expected.

Initially, the fluid-side energy equation is solved assuming a constant wall temperature at the lower boundary of the computational domain in the liquid. Using that temperature boundary condition and the newly-solved temperature distribution inside the liquid, a heat flux into the fluid can be calculated from the definition of the heat flux

$$q\left(r,t\right)=-k\frac{\partial T}{\partial y} \quad \text{at} \quad y=0 \tag{48}$$

Once this heat flux is calculated, the energy conservation equation for the solid wall is solved using this heat flux at the upper boundary surface (it should be noted that the microlayer is coupled to the solid phase implicitly as it is already included in this heat flux boundary condition). A new temperature field is thus obtained inside the solid, and a new temperature boundary condition is available for use on the fluid side. In order to ensure that energy is conserved at the interface between the wall and the fluid at every time step, this procedure is repeated until both temperatures and heat fluxes display insignificant change between iterations such that the temperature is continuous in all phases and the heat flux going out of the solid matches exactly the heat flux going into the fluid. Once this is accomplished, the calculations proceed to the next time step.

2.5 Computational procedure and framework

The characteristic length, velocity, and time for the solution are defined as follows

$$\begin{aligned} l_0 &= \sqrt{\frac{\sigma}{g\left(\rho_l-\rho_v\right)}} \\ u_0 &= \sqrt{g l_0} \\ t_0 &= \frac{l_0}{u_0} \end{aligned} \tag{49}$$

The governing equations on the fluid side are normalized with the above determined characteristic quantities. On the solid side similar characteristic quantities were defined as

$$
\begin{aligned}
l_{0s} &= L \\
t_{0s} &= \frac{\alpha_s}{l_0^2} \\
\Delta T_{nuc} &= T_{nuc} - T_{sat}
\end{aligned}
\tag{50}
$$

However, in order to maintain consistency with the rest of the normalized equations, the characteristic time and length defined for the fluid are also used in nondimensionalizing the energy equation in the solid substrate.

Initially, the wall surface temperature is uniform ($T_w = T_{nuc}$). The temperature distribution inside the solid wall is calculated assuming steady state conduction between the applied heat flux at the base of the heated surface and the specified uniform surface temperature. This results in a linear temperature profile inside the solid. The liquid is assumed stationary and saturated everywhere except for a thermal boundary layer with linear temperature gradient adjacent to the wall. The initial thermal boundary layer thickness in the liquid is calculated by assuming that the rate of heat removal from the wall matches exactly the heat flux input. A bubble is placed at the origin of the domain at $t = 0$ and for every subsequent cycle the nucleation criterion used to determine when to place an embryo at the origin is the temperature of the surface at the cavity site. When that temperature reaches T_{nuc} a bubble embryo is placed over the cavity. The simulation then proceeds through several cycles until no more changes can be observed between each cycle.

A staggered-grid finite difference scheme was used to discretize the governing equations where the scalar variables (such as temperature, pressure, and level set) were defined at the cell centers and velocity components were stored at the cell edges. A projection method was used to decouple the pressure solution from the momentum equations. In this standard method, the mass and momentum conservation equations are combined and then split into a momentum and pressure (Poisson) equation. More details on the projection method including treatment at the liquid-gas interface can be found in Son and Dhir (2007). A multigrid method was used to achieve faster convergence of the pressure equation since it takes up most of the computational time. In general, convection terms were solved explicitly using a second order ENO scheme and diffusion terms were solved implicitly using a central difference scheme. For the level set advection and reinitialization equations (Eqs. (23) and (26), respectively), a fifth order WENO scheme is used for the spatial derivatives and a third order TVD-RK scheme is used for time derivatives since high accuracy is desired in order to reduce any spurious currents that may develop (see Fedkiw et al. (1999) for details).

In order to keep the explanation simple, the computational steps for the solutions including conjugate conduction in the solid and dissolved gas in the liquid will be summarized separately in the following lists.

Time step loop

1. Solve the level set advection equation (Eq. (23)) and reinitialize the level set function (by solving Eq. (26) to steady state).

Iteration loop for coupling of energy conservation in solid and fluid phases

a. Using initial surface temperature (or that obtained in the previous iteration) as the boundary condition, solve the energy conservation equation (Eq. (31)) for temperature on the liquid side. Calculate heat flux from solid to liquid based on the calculated temperature field in the liquid.

b. Using the heat flux distribution from solid to fluid as the boundary condition (obtained in step *a*), solve the energy conservation equation (Eq. (45)) for the temperature inside the solid.

c. Check the difference in surface temperature and heat flux between the solutions of the solid and fluid phases. If the differences are both within an order of magnitude of the machine accuracy, proceed to step *2*; otherwise, go back to step *a* for the next iteration.

Alternate iteration loop (for coupling of energy and species conservation)

a. Make appropriate guess for interface temperature for first iteration of first time step.

b. With guessed interface temperature as the boundary condition, solve the energy conservation equation (Eq. (31)) for temperature on the liquid side. Calculate heat transfer rate through bubble interface based on the calculated temperature field in the liquid.

c. Using the heat transfer through bubble interface as the boundary condition (obtained in step *b*), solve species conservation equation (Eq. (32)) for concentration inside the bubble.

d. Determine saturation temperature distribution inside bubble and at bubble interface using the distribution of noncondensable gas obtained in step *c* (by implementing the procedure detailed in Eqs. (51) through (55)).

e. Check the change in mass fraction of noncondensable gas between the previous two iterations. If the change is within an order of magnitude of the machine accuracy, proceed to step *2*; otherwise, go back to step *b* for the next iteration.

2. Solve the momentum equation for velocity terms.

3. Solve the Poisson equation for total pressure ($p_v + p_g$ inside bubble).

4. Correct the velocities with the new known pressure gradients to ensure mass is conserved.

5. Go back to step *1* for the next time step.

3 Experimental setup

Nucleate pool boiling experiments performed by Dhir et al. (2012) aboard the International Space Station used a diamond turned aluminum wafer with five artificial cavities on the boiling surface. The diameter of the wafer was 89.5 mm and its thickness was 1.0 mm. Five artificial cavities were etched on the heater surface using the Electrical Discharge Machining (EDM) technique. Four of the cavities were located at the corners of a square while the fifth cavity was located at the center. The diagonal distance between the central cavity and the other cavities was 27.0 mm. Single bubble departure diameters at 10^{-4} g_e, predicted using numerical simulations, were used to determine the spacing between the prefabricated cavities. The spacing chosen was such that lateral bubble merger would occur prior to departure when multiple nucleation sites were activated on the heater surface. Each of the cavities was designed to have the following nominal dimensions: diameter ~10 μm and depth ~100 μm.

The heating of the aluminum wafer was accomplished using strain gage heaters bonded to the back-side of the wafer. In addition, thermistors were also bonded to the backside of the wafer to monitor the wafer temperature at several locations. The strain gage heaters and thermistors were grouped such that each of the five cavities could be activated independently. The aluminum wafer was bonded to a G-11 base and four additional thermistors were placed in the epoxy filled G-11 base. These thermistors were placed at depths of 5.3, 8.6, 14.7, and 24.5 mm from the bottom of the aluminum wafer. The backside of G-11 base was filled with an insulating epoxy to a depth of approximately 19 mm such that three of the thermistors in the G-11 base were embedded in the insulating epoxy, while the fourth (at a depth of 24.5 mm below the wafer) was located in the fluid just below the insulating epoxy. The temperatures measured by the three thermistors in the insulation and the thermistor located in the fluid were used to estimate the heat loss through the backside of the heater assembly.

A schematic of the experimental apparatus is shown in Figure 3.1. It consists of the test chamber, heater assembly, bellows, bulk fluid heater and a pump. The heater assembly was mounted at the bottom of the test chamber. The pressure in the test chamber (measured using three pressure transducers) was controlled by changing the position of the bellows. The bellows were controlled by external means to minimize any oscillations. The temperature of the fluid in the test chamber was maintained by the fluid conditioning loop which consisted of the pump, three inline heaters (total power = 180 W) and associated plumbing. The test chamber was also provided with six thermistors (labeled #1 through #6 in Figure 3.1) for measurement of fluid temperatures. Four sapphire windows were provided on the four walls of the test section for visual observation. Two cameras were used to record two orthogonal views of the boiling process occurring on the aluminum wafer. The test fluid used was filtered, degassed Perfluoro-n-Hexane (PFH). Fluid properties for PFH (including molecular weight) are given in Table 1.

The amount of gas dissolved in the liquid was estimated in-situ at periodic intervals. This was done by expanding the bellows, causing flash boiling to occur and saturation conditions to be reached quickly in the liquid. The saturated liquid temperature ($T_{sat,PFH}$) and test chamber pressure (p_{total}) were then measured and recorded. At saturation conditions, the partial pressure of the PFH vapor is known,

$$p_{PFH} = p\left(T_{sat,PFH}\right) \tag{51}$$

Knowing the partial pressure of the PFH vapor and the total pressure in the system, the partial pressure of the gas in the vapor space can be obtained using Dalton's law of partial pressures.

$$p_g = p_{total} - p_{PFH} \tag{52}$$

where p_{total} is the aforementioned test chamber pressure that was measured in the liquid at saturated conditions. Once the partial pressure of the gas, p_g, is known Henry's law provides a relationship between the partial pressure of the gas in the vapor space and the corresponding mole fraction of the gas dissolved in the liquid,

$$x_g = H_g p_g \tag{53}$$

where Henry's coefficient, H_g, has inverse pressure units. Combining Eqs. (51), (52), and (53), the mole fraction of the gas in the liquid can be calculated as,

$$x_g = H_g \left[p_{total} - p\left(T_{sat,PFH}\right) \right] \tag{54}$$

Finally, the mass fraction of the gas dissolved in the liquid can be obtained from the mole fraction using molecular weights as follows,

$$C_g = \frac{x_g M_g}{x_g M_g + x_{PFH} M_{PFH}} \tag{55}$$

where x_{PFH} is the mole fraction of the liquid (= $1 - x_g$).

A sample calculation to obtain the dissolved gas in the liquid is presented next. In one of the tests, after expanding the bellows and causing flash boiling of the liquid, the liquid temperature and test chamber pressure were measured as $T_{sat,PFH} = 42\ °C$ and $p_{total} = 71.4\ kPa$. According to regression analysis from NIST data, the pressure of the PFH vapor is given by,

$$p_{PFH} = p\left(T_{sat,PFH}\right) = p\left(42\ °C\right) = 58.1\ kPa$$

The dissolved gas in the liquid can then be obtained directly from Eq. (54) as,

$$\begin{aligned} x_g &= H_g \left[p_{total} - p\left(T_{sat,PFH}\right) \right] \\ &= 5.4 \times 10^{-5}\ kPa^{-1} \left[71.4\ kPa - 58.1\ kPa \right] \\ &= 7.2 \times 10^{-4} \end{aligned}$$

The mole fraction, or concentration, is therefore 720 parts per million for this case. Similarly, Eq. (55) is used to convert the mole fraction of 720 ppm to a mass fraction of 6×10^{-5}. Note that, in the absence of gas under the same conditions, the saturation temperature would have been 5.5 ^{o}C higher at 47.5 ^{o}C.

For a more detailed description of the experimental setup, procedure, data reduction, and anomalies encountered during experiments please refer to Dhir et al. (2012).

	Water	PFH
T_{sat} (^oC)	100	56.6
ρ_l (kg/m^3)	958	1592
ρ_v (kg/m^3)	0.598	13.4
c_{pl} ($J/kg\ K$)	4216	1102
c_{pv} ($J/kg\ K$)	2080	236
k_l ($W/m\ K$)	0.679	0.0537
k_v ($W/m\ K$)	0.0251	0.00260
h_{fg} (J/kg)	2.26×10^6	0.0948×10^6
σ (N/m)	0.0589	0.00835
μ_l ($kg/m\ s$)	282×10^{-6}	434×10^{-6}
μ_v (kg/ms)	12.3×10^{-6}	11.6×10^{-6}
M (g/mol)	18	338
β_l ($1/K$)	7.5×10^{-4}	1.6×10^{-3}

Table 1 Properties of water and Perfluoro-n-hexane (PFH) at 1 atmosphere pressure.

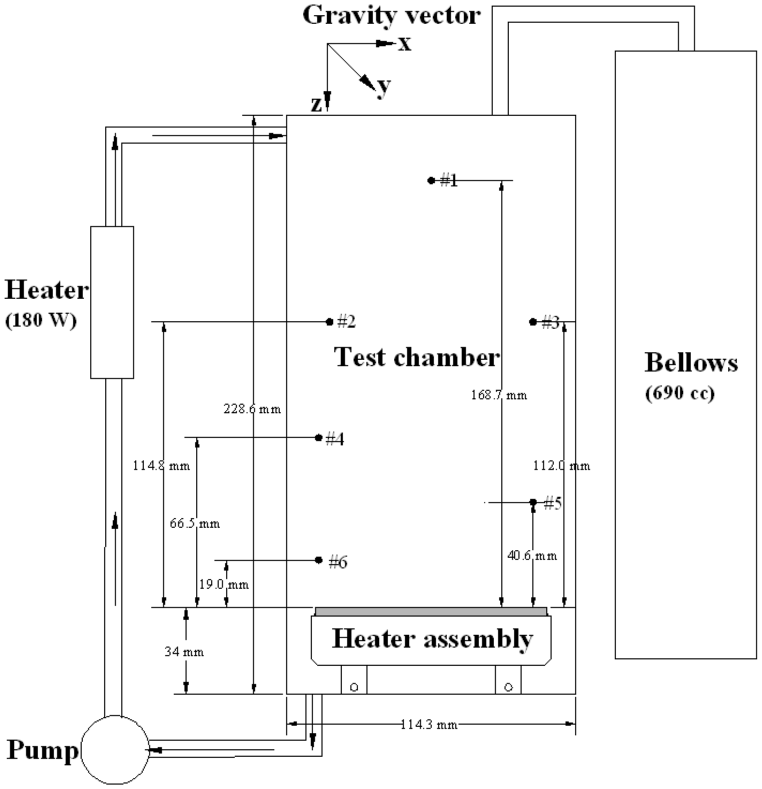

Figure 3.1 Schematic of Nucleate Pool Boiling Experiment (NPBX) apparatus.

4 Test problems and validation

4.1 Natural Convection under Microgravity Conditions

Buoyancy driven flows are usually described in terms of the Rayleigh number, *Ra*, given by

$$Ra = \frac{g\beta \Delta T L^3}{\upsilon \alpha} \tag{56}$$

where the length scale used (*L*) depends on the characteristic geometry of the particular problem being studied. For circular disc heaters, for example, the characteristic length used is generally the diameter of the disc or its area divided by perimeter. A critical Rayleigh number is defined as the value at which heat transfer changes from being primarily in the form of conduction to being primarily in the form of convection.

Correlations derived from experiments to predict heat transfer coefficients in natural convection are generally given in the following form

$$Nu = aRa^b \tag{57}$$

where *a* and *b* are correlated based on experimental data. For the case of a heated plate facing up, the McAdams (1954) recommends

$$\begin{aligned} Nu &= 0.54Ra^{1/4} \qquad 1\times10^5 < Ra < 2\times10^7 \\ Nu &= 0.14Ra^{1/3} \qquad 2\times10^7 < Ra < 3\times10^{10} \end{aligned} \tag{58}$$

where the characteristic length used in both the Nusselt number and Rayleigh number is the area of the heated surface divided by its perimeter. Also for the case of a heated plate facing up but for smaller Rayleigh numbers, Kobus and Wedekind (2001) provide the following

$$
\begin{aligned}
Nu &= 1.759 Ra^{0.13} && 3\times10^{2} < Ra < 1\times10^{4} \\
Nu &= 0.9724 Ra^{0.194} && 1\times10^{4} < Ra < 3\times10^{7}
\end{aligned}
\tag{59}
$$

Kobus and Wedekind performed experiments using circular discs and the correlations were developed using the diameter of the discs as a characteristic length in both Nusselt and Rayleigh numbers. During calibration, Dhir et al. (2012) performed natural convection experiments in the Nucleate Pool Boiling Experiment (NPBX) aboard the International Space Station (ISS). For the conditions and geometry present, the Rayleigh number using the wafer diameter as the characteristic length was of the order of 10^3 and is therefore within the range of applicability of Eq. (59). However, in the case of natural convection from a heated surface facing up (relative to gravitational acceleration), the critical Rayleigh number based on the thermal boundary layer thickness, δ_t, is reported by Sparrow et al. (1970) as being approximately equal to 1800. Assuming that initially heat transfer from the disc happens only by conduction, the thermal boundary layer thickness can be determined using transient conduction into a semi-infinite medium

$$\delta_t = \sqrt{\pi \alpha t} \tag{60}$$

The authors note that the value given for Ra_δ may be an over estimation due to the fact that the thermal layer growth time is not exactly known. A reasonable range proposed would go as low as $Ra_\delta = 1100$ as predicted in the previously performed analysis by Sparrow et al. (1964). The thermal boundary layer thickness as a function of time is shown in Figure 4.1 along with the corresponding Rayleigh number. The critical Rayleigh number range reported by Sparrow et al. is marked with dotted lines and it can be seen to be approached only after at least 22,000 seconds of conduction heat transfer. Since convection begins to dominate after the critical Rayleigh number is reached, the evolution of the thermal layer thickness is not valid beyond about 31,000 seconds. Nevertheless, this figure serves to illustrate that, since the duration of the experiments performed in the space station were never much higher than 1,000 to 1,500 seconds, it is not likely that significant fluid motion due to buoyancy was present during the natural convection calibration runs.

Figure 4.2 shows the Nusselt number as a function of time obtained from a numerical simulation of the conditions present in the experiments including temperature difference, fluid properties, heater dimensions, and gravity level. The Nusselt number is predicted to drop until approximately 21000 seconds, at which point it reaches a minimum and begins to rise. Eventually the Nusselt number becomes constant in time, indicating that steady state has been reached. The minimum Nusselt number indicates the beginning of convection heat transfer becoming more dominant over conduction and the time predicted for this to occur lies within the range of the critical Rayleigh number proposed by Sparrow et al. These results lend support to the ability of the present approach in predicting the evolution of buoyancy-driven fluid motion.

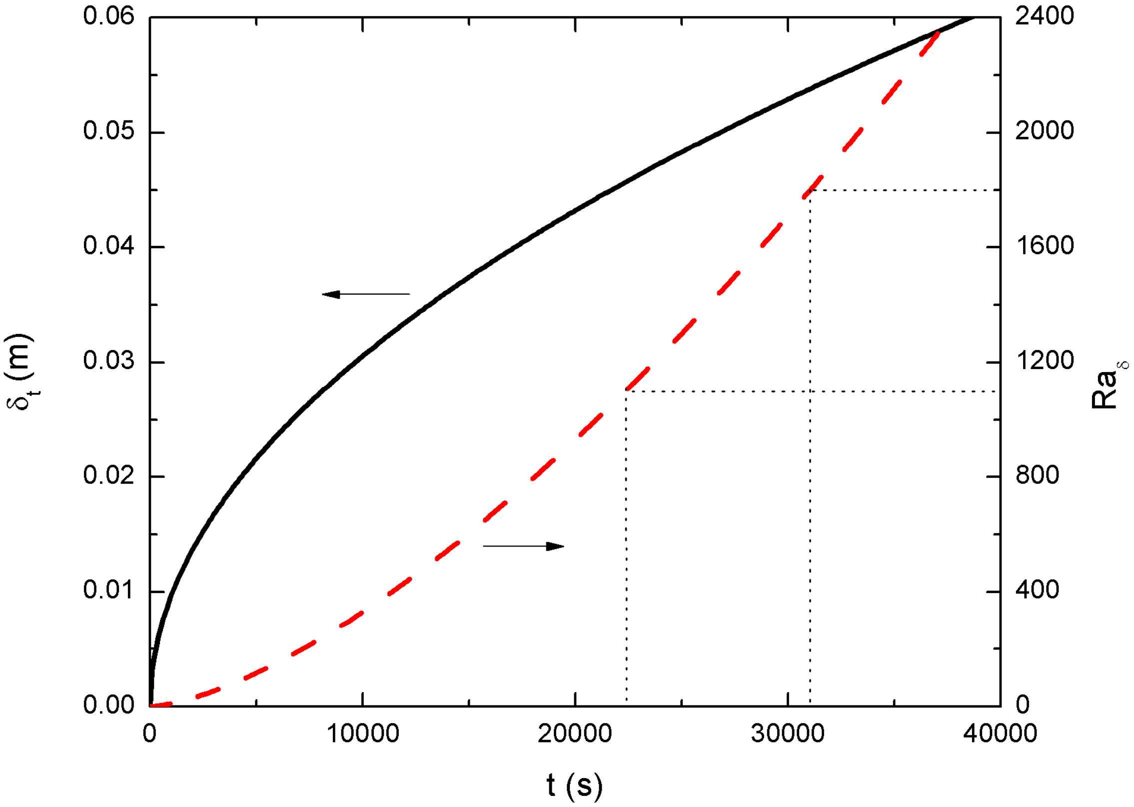

Figure 4.1 Evolution of thermal boundary layer thickness with time assuming transient conduction into a semi-infinite medium, and corresponding evolution of Rayleigh number with time.

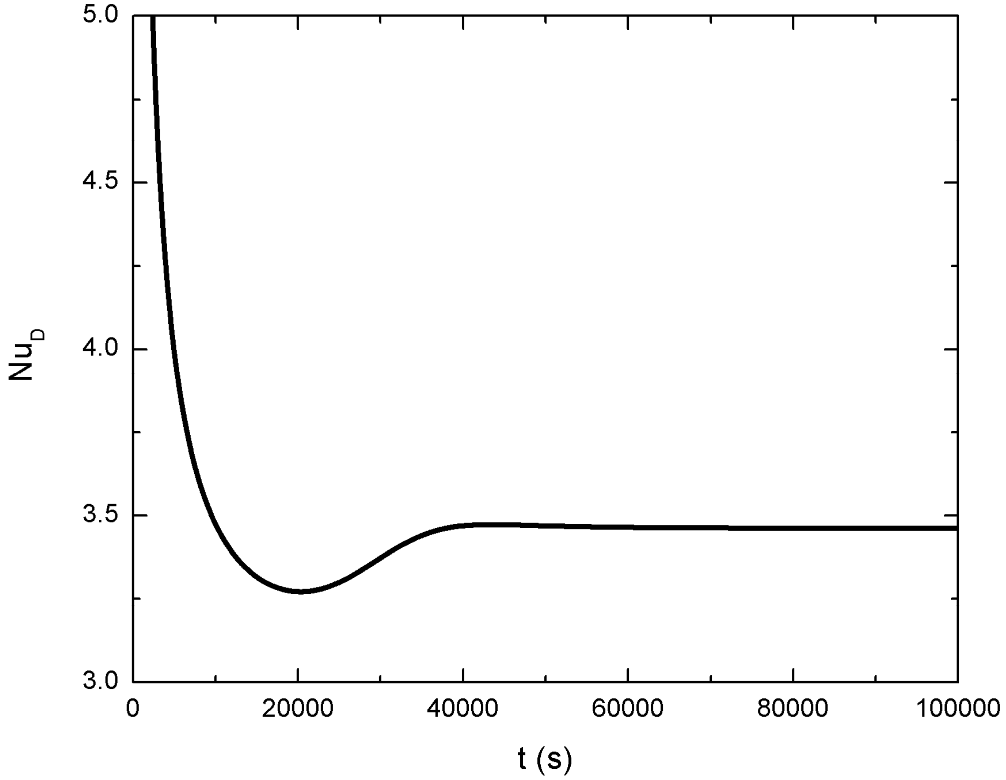

Figure 4.2 Simulated Nusselt number as a function of time for natural convection from a heated circular disc under microgravity conditions.

4.2 Condensation on a flat vertical wall in the presence of noncondensables

In order to test the accuracy of the simulation including the presence of the noncondensable gas, the standard problem of film condensation on a cooled vertical wall was studied. A schematic representation of the physical system is given in Figure 4.3. Numerical simulations were performed for the case of pure water vapor condensing on a cooled wall and the case of a vapor and air mixture under identical conditions. The reduction in rate of heat transfer due to the presence of the noncondensable gas (air) is then quantified for different wall temperatures and different bulk mass fractions of air. The present results are compared to the experimental results obtained by Othmer (1929) and the simplified problem solved analytically by Sparrow and Lin (1964) in Figure 4.4. The agreement observed between the numerical simulations and experimental results lends credibility to the approach employed presently. Figure 4.5 shows representative profiles of the mass fraction of noncondensable gas 5 mm downstream from the leading edge. The coordinate y is measured horizontally outwards from the liquid-vapor interface. The mass fraction of gas is seen to drop rapidly, reaching its bulk value within 2 mm. For otherwise identical conditions, the interface mass fraction of gas is seen to be strongly dependent on condensation rate (which is primarily dependent on the temperature difference between the saturated vapor and the wall).

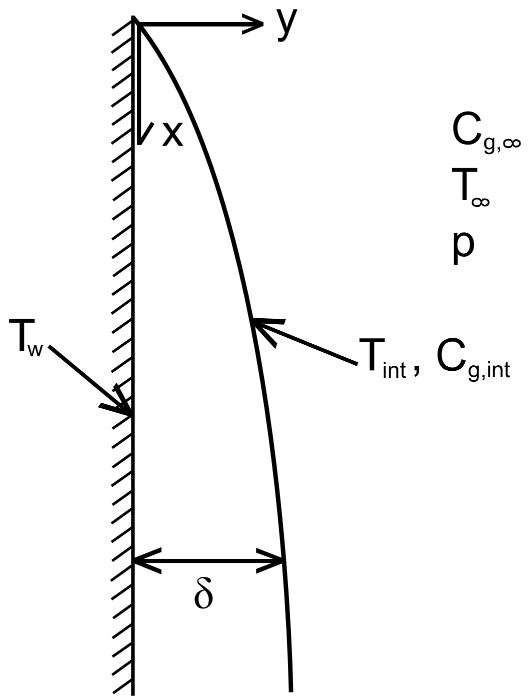

Figure 4.3 Schematic representation of the physical system for condensation on a flat vertical wall in the presence of noncondensables.

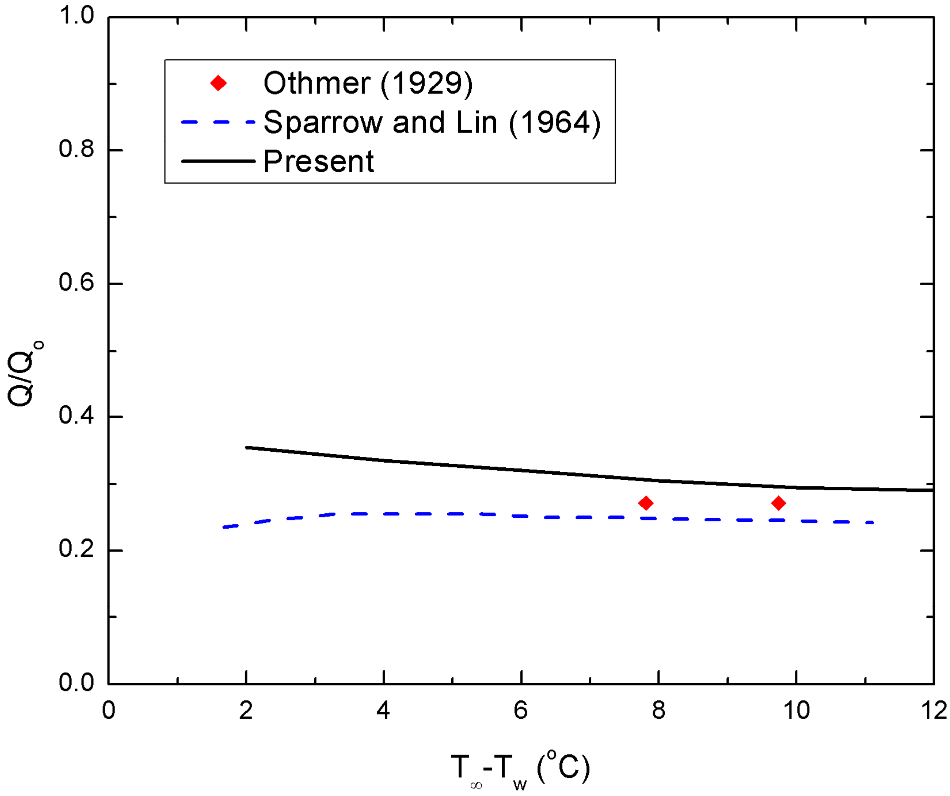

Figure 4.4 Comparison of heat transfer reductions obtained in experiments, analytical predictions, and present numerical simulations with $C_{g,\infty} = 0.05$.

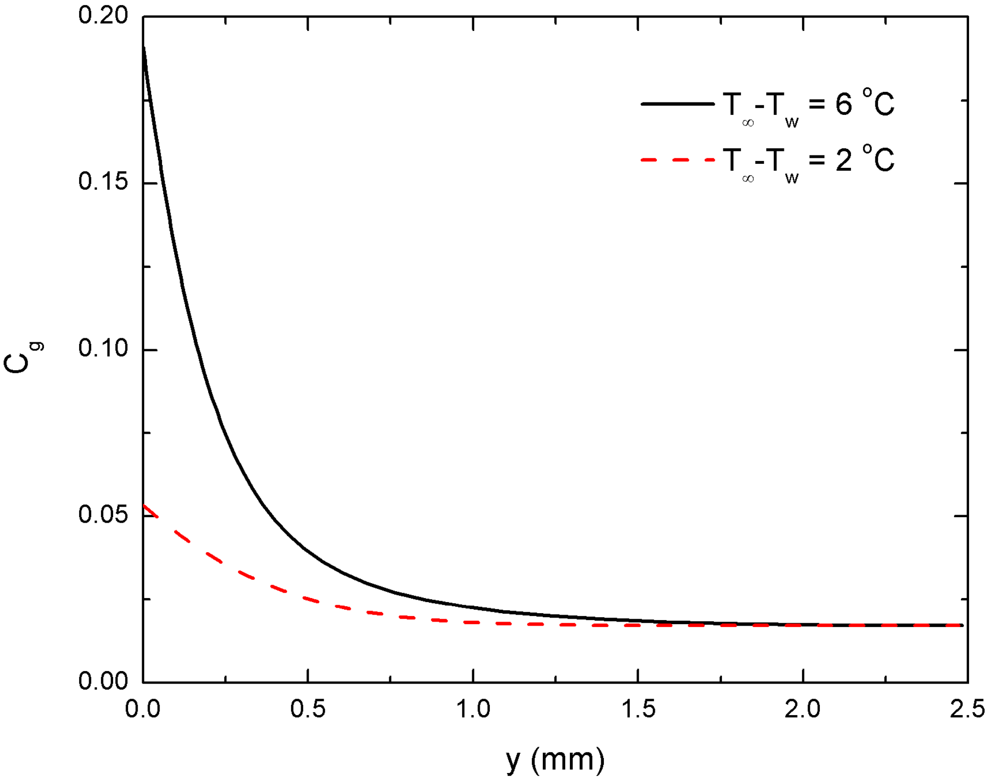

Figure 4.5 Representative profiles of noncondensable mass fraction and various wall temperatures 5 *mm* away from the leading edge (y is measured from the liquid-vapor interface) with $C_{g,\infty}$ = 0.017.

5 Results and discussion

5.1 Coupling of solid substrate

All simulations presented in this section were performed using the properties of saturated water at one atmosphere pressure and the contact angle was assumed to remain constant at 35^{o} even for the different solid substrates. The computational domain on the fluid side was chosen to be $\left(R/l_0, Y/l_0\right) = \left(1,4\right)$. This affords a compromise between being small enough to allow for practical computational time but large enough that the simulations are unaffected by the boundaries.

5.1.1 Surface Temperature Fluctuations

Figure 5.1 shows the temperature variation at the surface of the solid as a function of time for both the present study and the experimental findings of Moore and Mesler (1961). The experiments were run for high heat flux, fully developed nucleate boiling on a 1.6 *mm* thick nichrome strip, whereas the present study focuses on single cavity, isolated bubble cycles on a 1 *mm* thick steel surface. Both the thermal conductivity and diffusivity of steel are approximately 15% higher than those of nichrome. In the experiments, observed temperature drops at the location of the embedded thermocouple exceeded 15 ^{o}C and the time elapsed between successive cycles was as low as 10 *ms*. The location monitored in the present study is 0.4 *mm* away from the center of the cavity, approximately where the bubble base diameter reaches its maximum value. In the simulations the temperature drops rarely exceed 5 ^{o}C for a steel surface with $\Delta T_{nuc} = 6\ ^{o}C$.

Therefore, in order to compare the present study with the experimental results, the wall temperature and the time are normalized such that the graph shows two cycles and the entire temperature range for both cycles. Despite the differences in wall temperatures and time scales between the two cases, the overall behavior observed is very similar. At the surface of the solid, temperatures fluctuate noticeably over short periods as the bubble base first expands outwards then contracts inwards before departure.

A plot of the temperature field during bubble growth is shown in Figure 5.2 along with the vapor-liquid, liquid-solid, and solid-vapor interfaces for water boiling on a smooth 0.5 *mm* thick stainless steel disc with a single cavity in the middle and at one atmosphere pressure. In Figure 5.2 (b), a close-up of the area of interest is shown. It can be clearly seen from the temperature contours that the temperature drop in the solid is most pronounced at the point where the bubble interface comes into contact with the wall. This is where the microlayer is located and where significant evaporation takes place. Thus, the three-phase point is the approximate location with the highest rate of heat removal from the solid wall. Elsewhere on the surface of the wall, the phase change phenomenon affects the heat transfer indirectly due to fluid motion induced by growth and departure of bubbles.

Due to the sharp heat flux peak approximately accompanying the triple point, when the bubble base diameter reaches the monitored location the temperature drop is sharp. As the base diameter shrinks, the wall temperature rises. However, after the bubble ultimately departs, although the heat transfer is no longer aided by the evaporation of the microlayer, the wall is kept cool by the liquid that rushes in to replace the volume previously occupied by the bubble. As a result, the remaining temperature recovery is much slower as heat diffuses into the liquid and the thermal boundary layer develops in the liquid.

Moghaddam et al. (2009) performed experiments using an array of temperature sensors embedded within a dual layer wall. Their setup allowed them to study the details of the heat transfer mechanisms involved at an active site during nucleate boiling. They reported high frequency data including wall temperature and calculated heat flux at several locations distributed radially from the artificial cavity. The data obtained is ideal for comparison to numerical simulations as they provide a level of detail unprecedented in single bubble pool boiling experiments. The simulation conditions were imposed to match those of the experiments, including fluid properties, heater substrate properties and thickness, and wall temperature (imposed at the bottom of the heater substrate). Since the observed contact angle was not reported by the authors, it was assumed to be a static 10^o in the simulations (a common value reported by other studies using FC72 as the fluid). Additionally, although a constant temperature was imposed in the experiments below the 10 μm thick benzocyclobutene (BCB) surface, this temperature was not reported. In the simulations, the imposed temperature was approximated using the reported average surface temperature and the calculated transient heat flux. This resulted in a constant temperature boundary condition at the bottom of the BCB surface of 82^oC. Figure 5.3 shows local wall temperature and heat flux comparisons between the experiments of Moghaddam et al. (2009) and predictions from present numerical simulations. Despite the uncertainties in the experimental contact angle and imposed temperature, and the assumption of static contact angle, the simulated surface temperature fluctuations can be seen to closely resemble the experimental results in Figure 5.3. One noticeable difference is a result of the different growth periods observed. Since the growth period predicted by the simulations is almost 1 *ms* longer than in the experiments, the dips in local wall temperature and spikes in local wall heat flux do not exactly align during the second cycle.

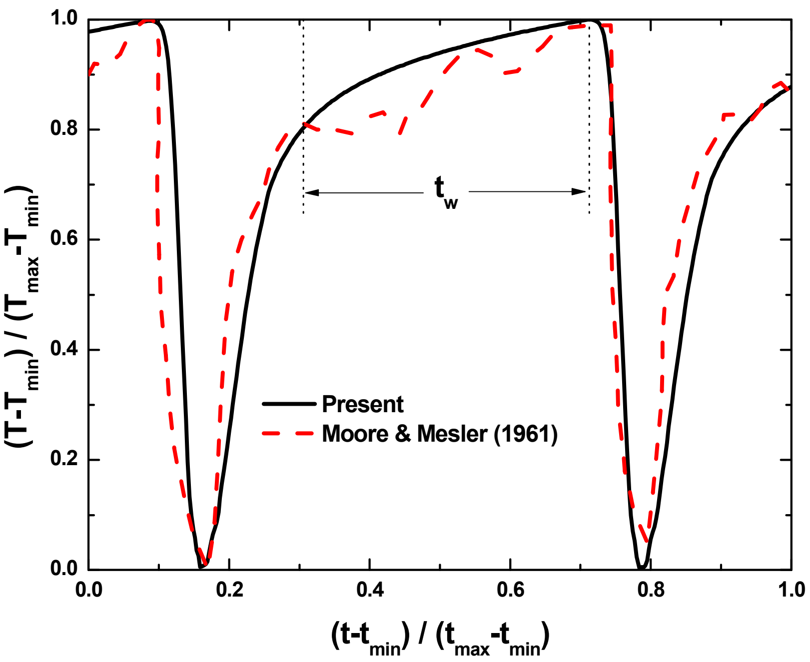

Figure 5.1 Comparison between numerical and experimental wall surface temperature fluctuations in time for a fixed radial location. The experiments were run on 1.6 *mm* nichrome at high heat flux fully developed nucleate boiling and the maximum temperature drop is approximately 15 ^oC. The numerical simulations are for low heat flux single bubbles on a 1 *mm* steel surface and the maximum temperature drop is 5 ^oC.

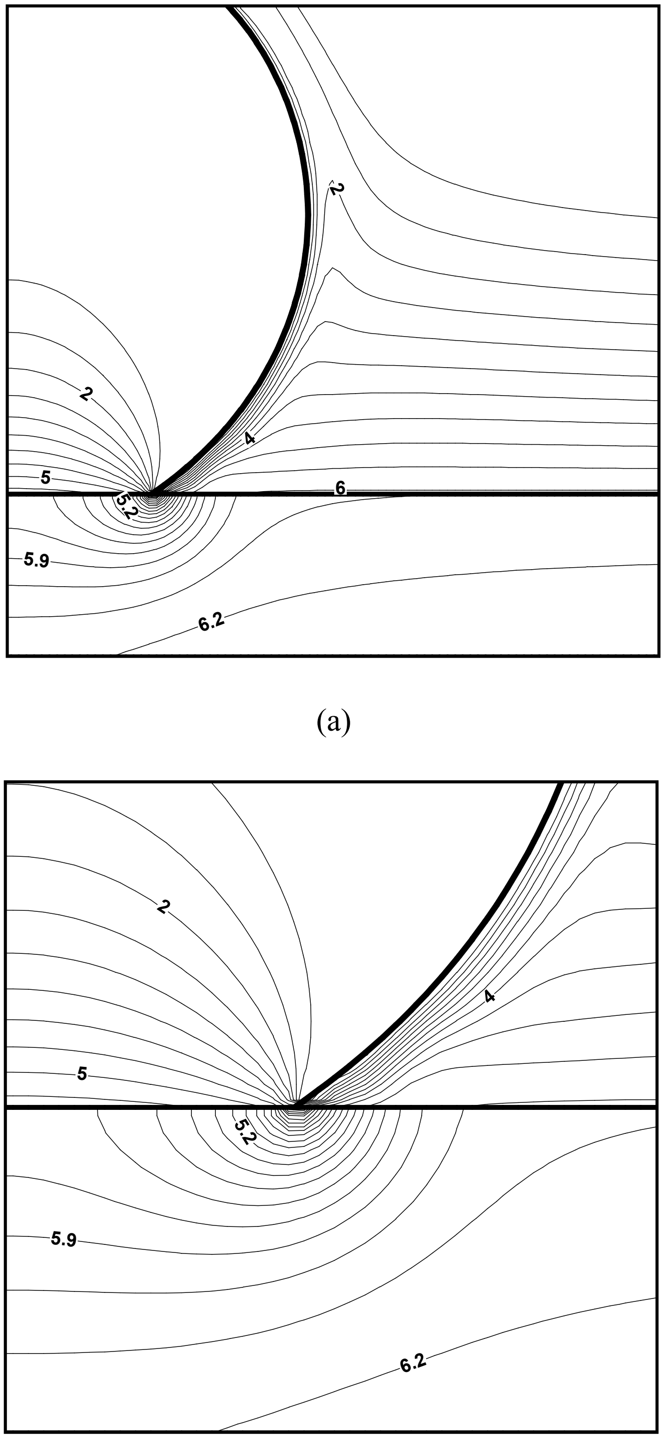

(a)

(b)

Figure 5.2 Temperature contours and phase interfaces for water boiling on a steel disc of 0.5 *mm* thickness at one atmosphere pressure, $q_{w,in}$ = 1.1 W/cm^2 with ΔT_{nuc} = 6 ^oC and $\varphi = 35^o$. Viewing dimensions are (a) 2 by 2 *mm*, and (b) 1 by 1 *mm*.

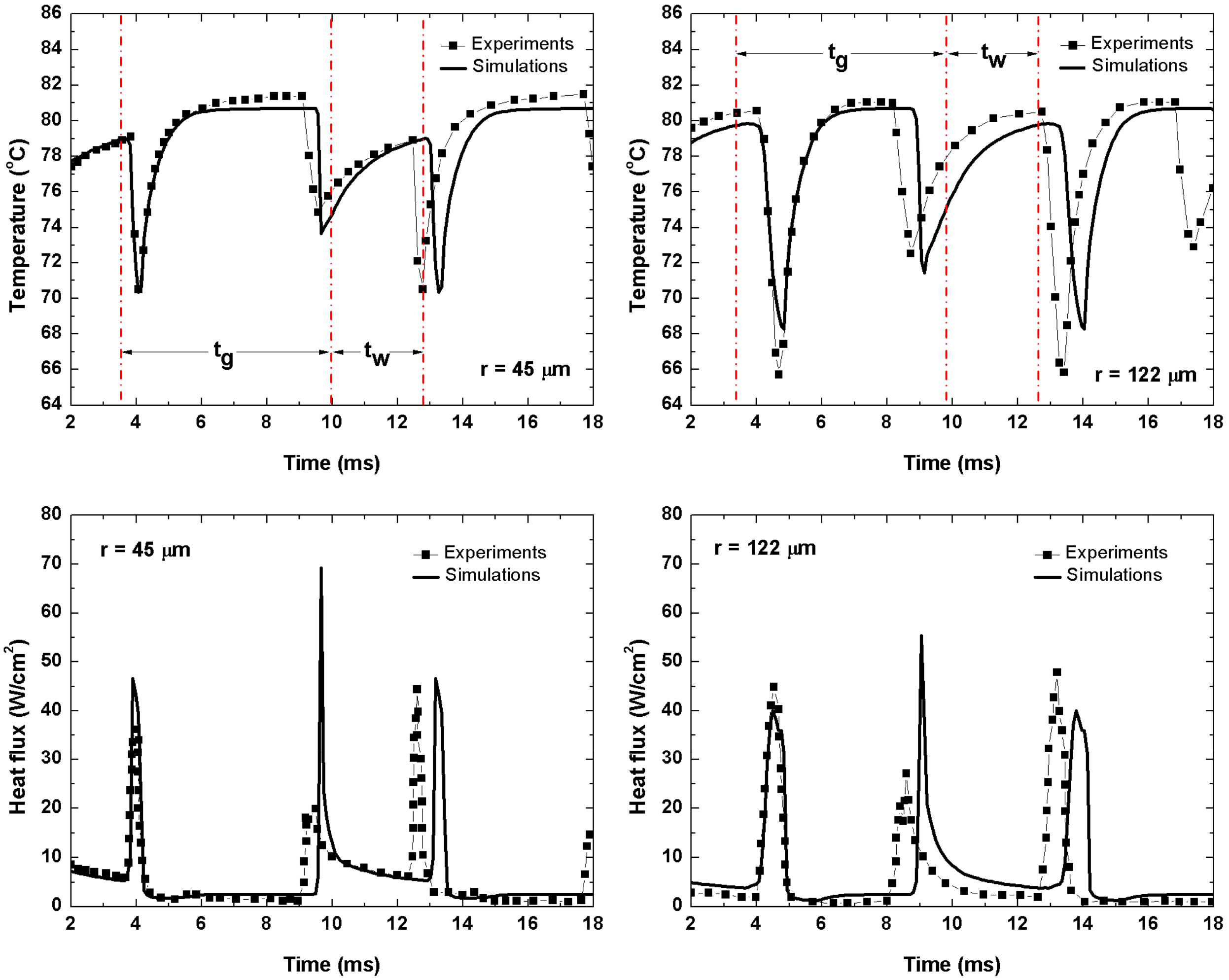

Figure 5.3 Local surface temperature and heat flux comparisons between experimental results of Moghaddam et al. (2009) and present numerical simulations. Fluid is FC-72, solid substrate is benzocyclobutene (BCB), and contact angle is 10°. Constant temperature of 82 °*C* is imposed at the bottom of the 10 *μm* BCB substrate. Results are reported at two different radial locations.

5.1.2 Validity of constant temperature assumption for studying bubble dynamics

In the previous section, significant surface temperature variations were shown to occur during nucleate pool boiling. In this section, the effect on bubble dynamics and heat transfer will be compared when the boundary condition changes from constant heat flux at the back side of the solid wall to constant surface temperature. For this comparison, the case with constant heat flux on a 1 *mm* thick copper wall was simulated first due to the fact that both the wall superheat and the waiting period are required inputs for running the constant wall temperature case and neither can be predicted exactly. The applied heat flux was 1.1 W/cm^2 and the nucleation superheat was 6 ^oC. Since the wall superheat varies both in time and space, the quantity reported is averaged over the entire radius of the computational domain (R = 2.5 *mm*) at the surface of the wall and over the span of a full ebullition cycle which includes both the growth and waiting periods.

$$\Delta T_w = \frac{1}{R^2\left(t_g + t_w\right)} \int_{t=0}^{t=t_g+t_w} \int_{r=0}^{r=R} \left(T - T_{sat}\right) r \; drdt \tag{61}$$

Using the calculated wall superheat and waiting period, the case with constant wall superheat was simulated to match the conditions as closely as possible. The results listed in Table 2 show that for identical wall superheats, the rate of heat removal from the wall is 7 percent higher in the constant wall superheat case. This indicates that the presence of the temperature fluctuations observed as a result of the coupling to the liquid side tend to slightly reduce the efficacy of the boiling process. Therefore, a wall that is artificially kept at a constant superheat only slightly over-predicts the rate of heat removal and the assumption of constant wall temperature to study bubble dynamics is not unrealistic.

The same procedure is repeated using a higher applied heat flux of 2 W/cm^2 and higher nucleation superheat of 8 ^oC (please refer to the next section for an explanation of how applied heat flux is related to nucleation superheat). Table 3 shows that the difference in heat flux obtained between the cases of constant wall temperature and conjugate conduction solution remained small. The changes in bubble departure diameter and growth period are also small at +2.6 percent and -1 percent, respectively.

	Constant q_w	Constant ΔT_w
ΔT_w (^oC)	6.63 (outcome)	6.63 (imposed)
D_d (mm)	2.21	2.26
t_g (ms)	22.4	22.2
q_w (W/cm^2)	1.10 (imposed)	1.18 (outcome)
t_w (ms)	40.6 (outcome)	40.6 (imposed)

Table 2 The effect of boundary conditions on heat transfer and bubble dynamics for a 1 *mm* thick copper plate with $\Delta T_{nuc} = 6\ ^oC$.

	Constant q_w	Constant ΔT_w
ΔT_w (^oC)	8.54 (outcome)	8.54 (imposed)
D_d (mm)	2.27	2.33
t_g (ms)	21.0	20.8
q_w (W/cm^2)	1.96 (imposed)	2.05 (outcome)
t_w (ms)	17.9 (outcome)	17.9 (imposed)

Table 3 The effect of boundary conditions on heat transfer and bubble dynamics for a 1 *mm* thick copper plate with ΔT_{nuc} = 8 ^oC.

5.1.3 Effect of Wall Superheat on Bubble Dynamics

Figure 5.4 shows growth histories and waiting periods for two cases with different imposed heat fluxes and resulting average wall temperatures but otherwise identical conditions. As it has been shown numerically by Son et al. (1999), with increasing wall superheat the growth period decreases and the bubble departure diameter increases. However, a new and more discernible feature is the significant decrease in waiting periods for the same change in wall superheat. The imposed nucleation superheats were 6 and 7 ^{o}C for the applied wall heat fluxes of 1.1 W/cm^2 and 1.5 W/cm^2, respectively. The nucleation superheats were based on the assumption that, at the onset of nucleate boiling, $q \sim \Delta T_w^2$ as predicted by combining Hsu's inception criterion with the assumption that the temperature profile adjacent to the wall is linear (see section 1.2 for details). However, the resulting wall superheats as calculated based on Eq. (61) were 6.63 and 8.54 ^{o}C and therefore do not have a linear dependence on nucleation superheat. Nevertheless, this relationship is used in predicting the nucleation superheats for the remainder of this section

$$\Delta T_{nuc} \sim \sqrt{q_{w,in}} \qquad (62)$$

As the heat flux supplied at the bottom of the solid is varied, Eq. (62) is used to determine the appropriate nucleation superheat at the cavity site. All other conditions remain unchanged. It should be noted that this relationship between nucleation superheat and applied heat flux is used presently solely for the purpose of investigating the dependence of single bubble dynamics on wall superheat and it may not be applicable at higher heat fluxes.

Figure 5.5 shows the effect of wall superheat on the growth period. Increasing wall superheat results in faster bubble growth rates. The result is that the time taken for bubble to attain departure diameter decreases with increasing wall superheat. However, the dependence of the growth period on wall superheat is weak as reflected by the magnitude of the power.

Figure 5.6 shows the effect of wall superheat on the bubble departure diameter. The correlation is seen to be positive as the departure diameter increases with increasing wall superheat. The positive correlation is in agreement with the prediction of Cole and Shulman as given by Eq. (17) in Section 1.3. However, the dependence is weak. For a relatively large range in superheats of 4 to 12 ^oC, the departure diameter varies by a total of less than 15 percent.

Figure 5.7 shows that the waiting period can also be related directly to the wall superheat. An increase in heat flux results in a higher average wall superheat and a smaller waiting period. The wall superheat reported was calculated in the same way as before by using equation (61). As seen in Figure 5.7, an inverse power law is observed to fit well with the results obtained from a simple parametric study. The experimental correlation developed by Basu et al (2005) for subcooled flow boiling corroborates this functional relationship.

The growth and waiting periods can be combined into a bubble release frequency in order to compare with semi-empirical correlations reported in the literature. Figure 5.8 shows the bubble release frequency, f, as a function of the wall superheat. The results from the simulations show that the bubble release frequency increased by a factor of almost 10 for a wall superheat increase from 4 ^oC to 12 ^oC. Since the growth and waiting periods both decrease with increasing wall superheat, it is reasonable to expect the bubble release frequency to increase with increasing wall superheat. However, the semi-empirical correlation of Zuber (1963) does not predict such a dependence. In Zuber's correlation (Eq. (20)), the product of bubble release frequency and bubble departure diameter is a constant that depends only on fluid properties and gravitational acceleration. Since bubble departure diameter is shown to increase with increasing wall superheat, bubble release frequency must decrease. The prediction of decreasing bubble release frequency with increasing wall superheat is incorrect and reveals that Zuber's correlation is not applicable in this case. Mikic and Rohsenow's correlation (Eq. (21)) include a Jakob number on the right hand side and therefore the effect of wall superheat is included. The bubble release frequency predicted by Mikic and Rohsenow's correlation is about two times higher than predictions from the simulations for the entire wall superheat range tested.

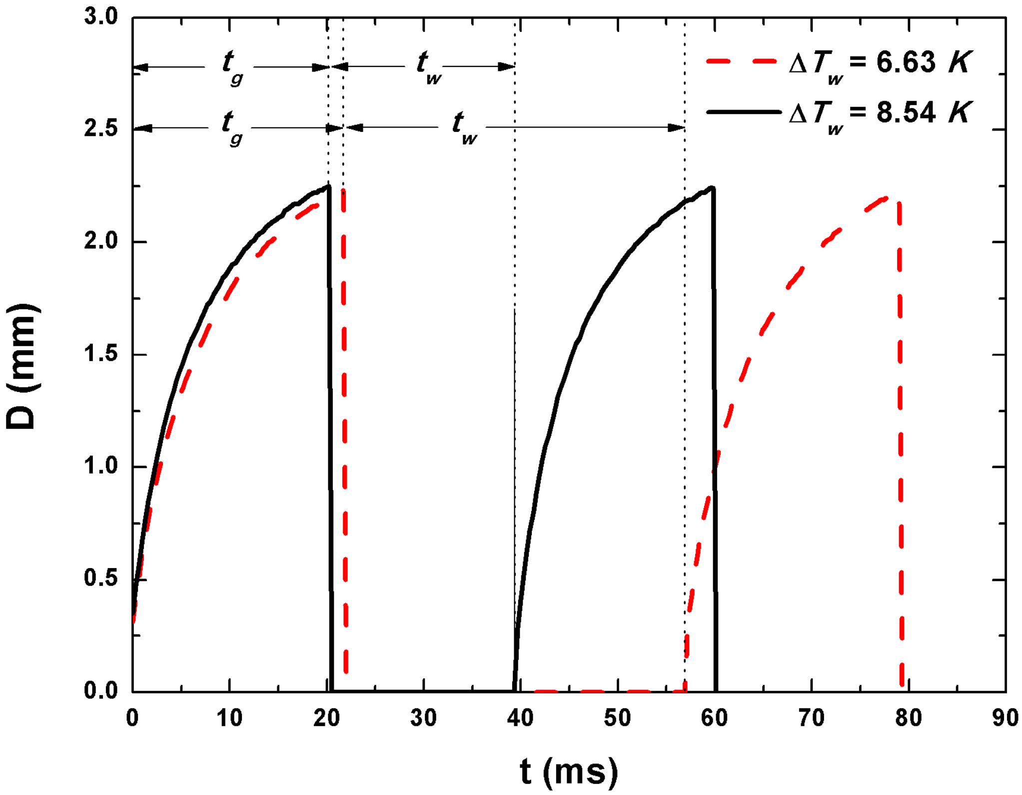

Figure 5.4 Effect of wall superheat on growth and waiting time for water boiling on a 1 mm thick copper disc with $\varphi = 35^o$ at one atmosphere pressure and two different input heat fluxes $q_{w,in}$ = 1.1 W/cm^2 and $q_{w,in}$ = 2.0 W/cm^2 and corresponding nucleation superheats ΔT_{nuc} = 6 ^oC and ΔT_{nuc} = 8 ^oC.

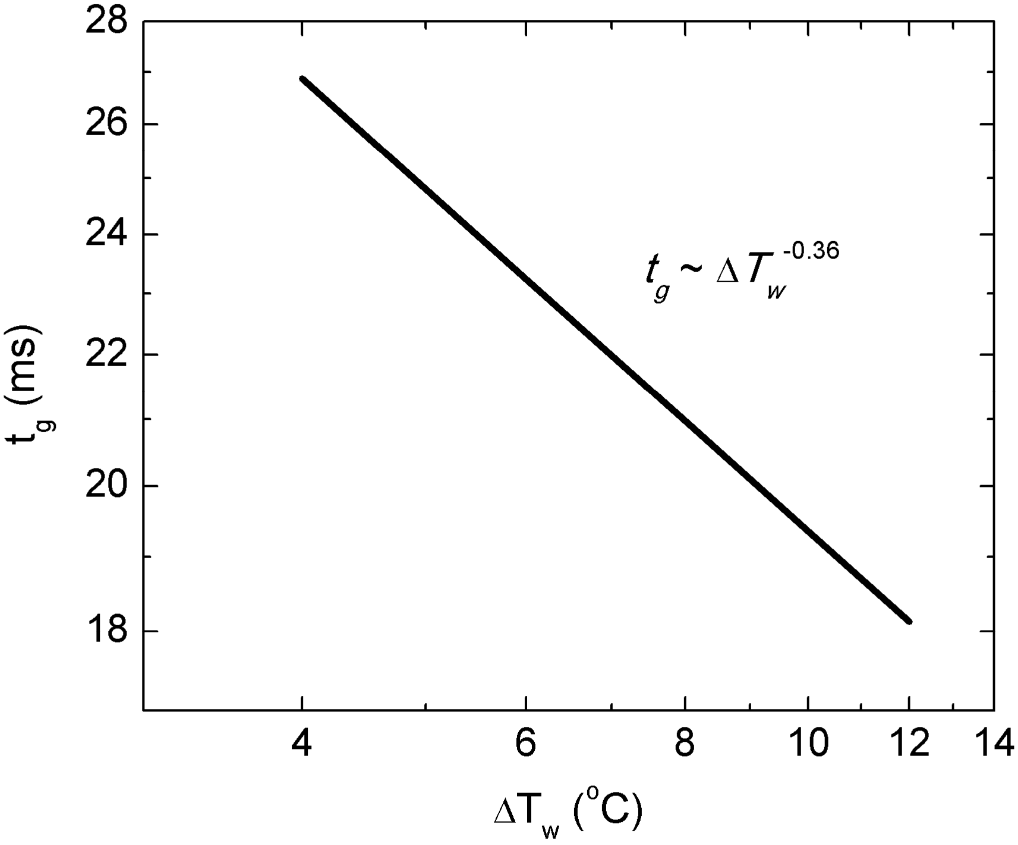

Figure 5.5 Growth period as a function of wall superheat for water boiling on a 1 *mm* thick copper plate with $\varphi = 35^o$ at one atmosphere pressure.

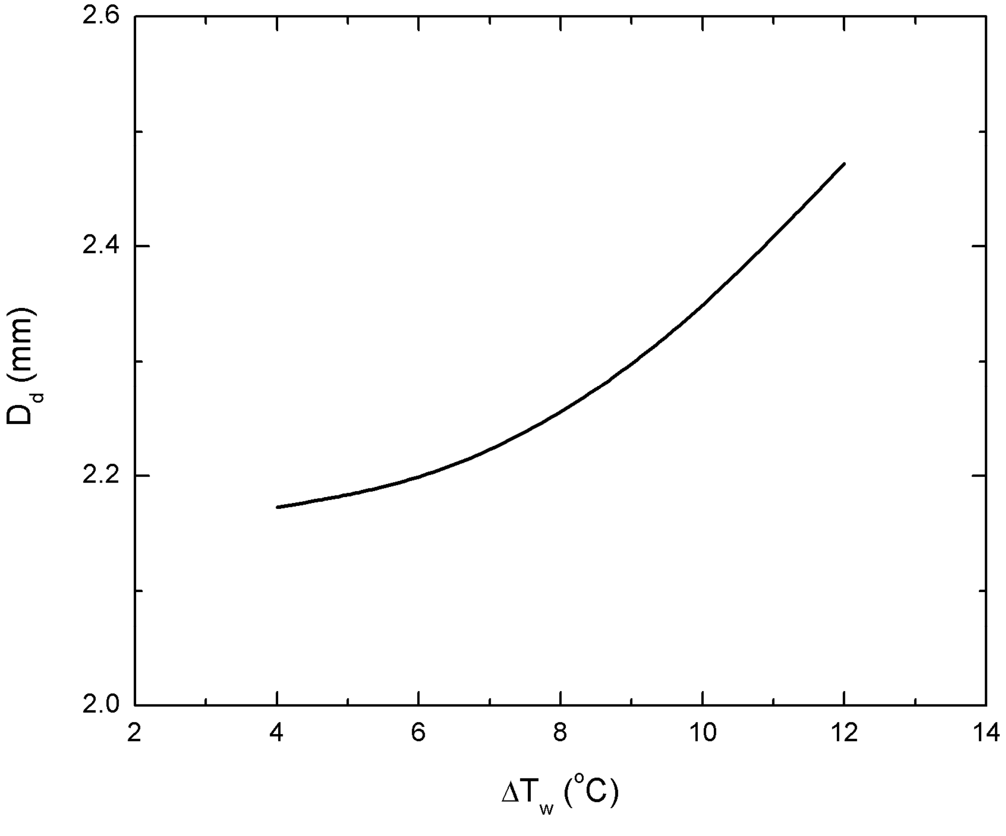

Figure 5.6 **Departure diameter as a function of Wall superheat for water boiling on a 1 *mm* thick copper plate with $\varphi = 35^o$ at one atmosphere pressure.**

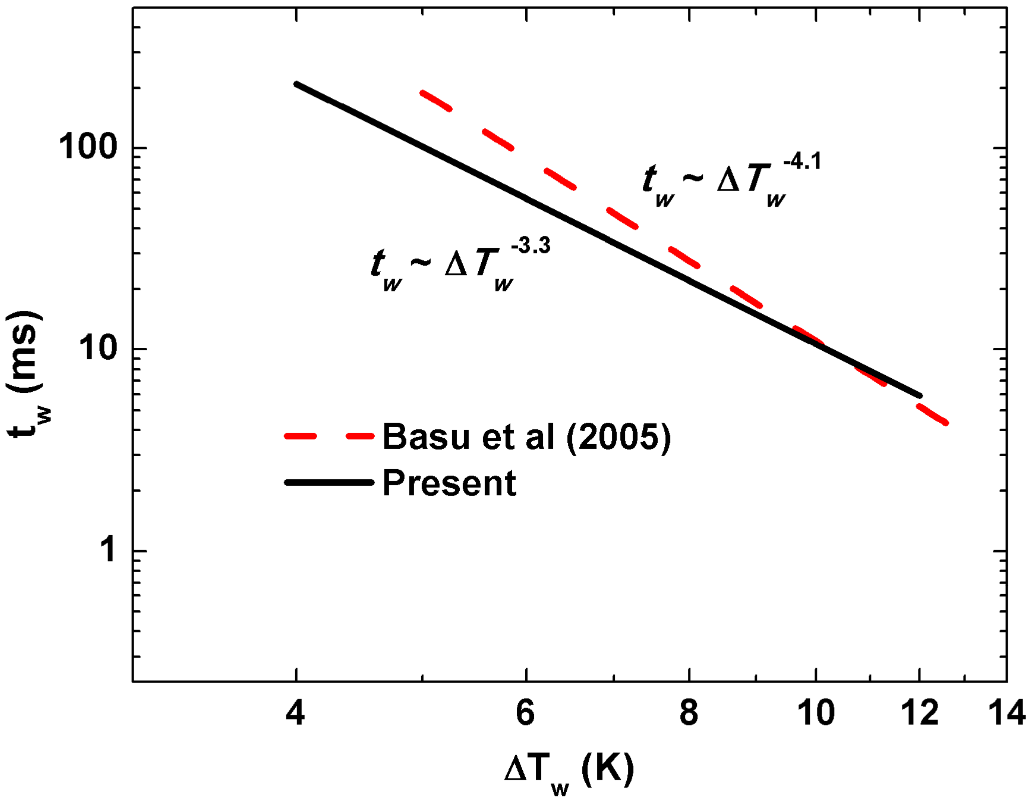

Figure 5.7 Comparison between numerical results and experimental correlation for waiting time as a function of wall superheat. The simulations were carried out using a 1 *mm* thick copper disc with $\varphi = 35^o$ at one atmosphere pressure.

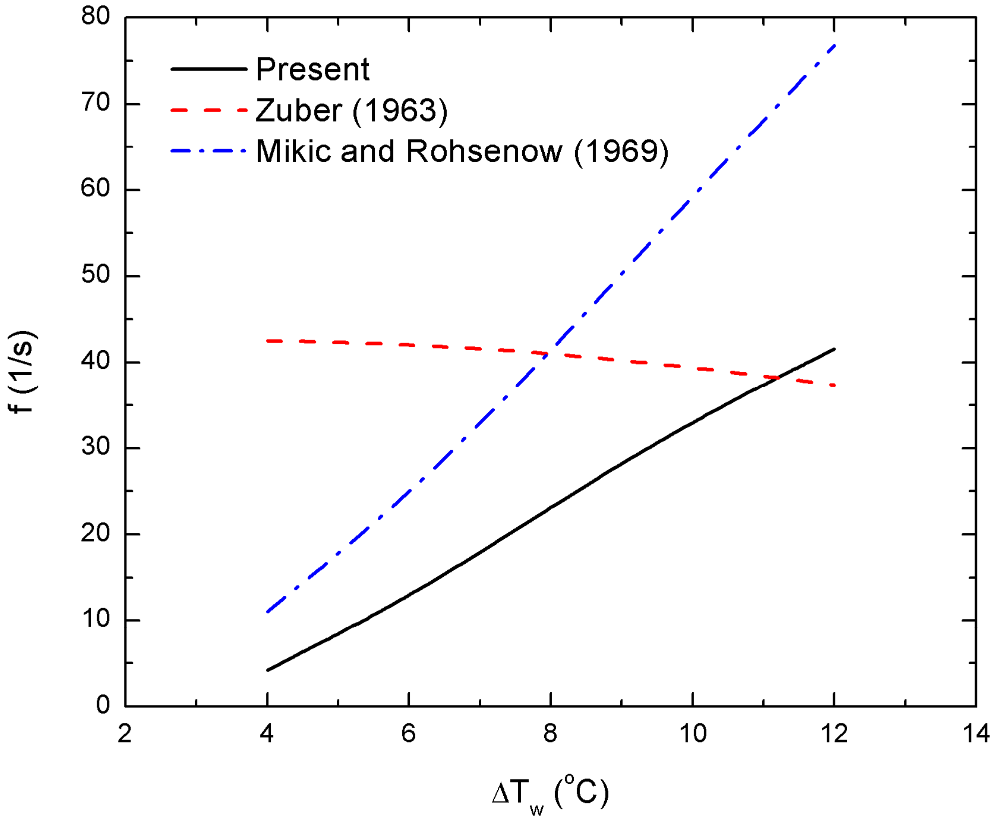

Figure 5.8 Bubble release frequency as a function of wall superheat from simulations of water boiling on a 1 *mm* thick copper disc with $\varphi = 35^{\circ}$ at one atmosphere pressure and semi-empirical correlations of Zuber (1963) and Mikic and Rohsenow (1969).

5.1.4 Effect of Substrate Thickness and Properties on Bubble Dynamics

Figure 5.9 shows the bubble growth history for copper, steel, and borosilicate glass when quasi steady condition is achieved while keeping all other conditions unchanged. The wall thickness is 0.3 *mm* and the input heat flux is $q_{w,in} = 1.1\ W/cm^2$. The clear pattern observed is that increasing wall thermal conductivity and diffusivity results in slower growth rates and smaller bubbles. The reason for this behavior is not immediately clear and it will be explained in detail in section 5.1.5. It is worth noting that due to inertial effects, a higher growth rate affects the departure diameter. According to the correlation of Cole and Shulman (1966) given in Eq. (17) the departure diameter increases with increasing growth rate. This pattern can also be observed in Figure 5.9.

Figure 5.10 shows the growth period as a function of substrate thickness for different materials. The input heat flux and nucleation superheats remained the same: $q_{w,in} = 1.1\ W/cm^2$ and $\Delta T_{nuc} = 6\ ^oC$. The almost straight horizontal lines indicate that the growth period is generally unaffected by the thickness of the wall. All variations obtained from the simulations were well within the cycle-to-cycle variations observed normally. However, it is clear that the thermophysical properties of the substrate's material have an effect on the growth period. The bubbles depart sooner for the less conducting materials. The bubble departure diameter is shown in Figure 5.11 for varying wall thicknesses and thermophysical properties. As with the growth period, the bubble departure diameter is almost unaffected by the thickness of the substrate but there is a noticeable effect from material properties.

In Figure 5.12, the effect of solid thickness on waiting time while a constant heat flux is applied at the base of the solid is shown. The results are shown for three solids with widely varying thermophysical properties but a fixed contact angle. The behavior is similar for both steel and borosilicate glass: waiting time decreases as the wall thickness increases. This can be attributed to the fact that a thicker wall provides more thermal mass to aid in a quicker recovery of the surface temperature. This behavior is explored in detail in section 5.2.3. As the thickness is increased further, the waiting time quickly attains an asymptotic value that becomes independent of thickness. The main trend between the different materials in Figure 5.12 is that with increasing thermal conductivity and diffusivity, the waiting time decreases. For the highly conductive copper, the time taken for the surface to recover its temperature is much smaller than it is for the thermally insulating borosilicate glass.

In Figure 5.13 the bubble release frequency is shown as a function of wall thickness for different substrate materials. The dependence of bubble release frequency on substrate thickness is weak, although it is seen to rise slightly between 0.3 *mm* and approximately 1.5 *mm* for both stainless steel and borosilicate glass. Its dependence on the thermophysical properties of the substrate is more pronounced with more highly conductive materials yielding higher bubble release frequencies. In section 1.4, semi-empirical correlations were given that predict that bubble release frequency is inversely proportional to the bubble departure diameter. Using the relation proposed by Mikic and Rohsenow (1963) given in Eq. (21) combined with the departure diameter predicted from the relation proposed by Fritz (1935) given in Eq. (16), the frequency can be predicted as approximately 35 bubble cycles per second. If the bubble departure diameter obtained presently is used instead, the frequency predicted is 23 bubbles per second. The highest frequency shown in Figure 5.13 (for copper) under-predicts this value by 20 percent. Nevertheless, the semi-empirical models are dependent solely on fluid properties and therefore unable to predict variations in frequency due to substrate changes.

	Glass	Steel	Copper
k (W/mK)	1.09	15	401
α x 10^6 (m^2/s)	0.510	3.88	117

Table 4 Thermo-physical properties for different materials studied

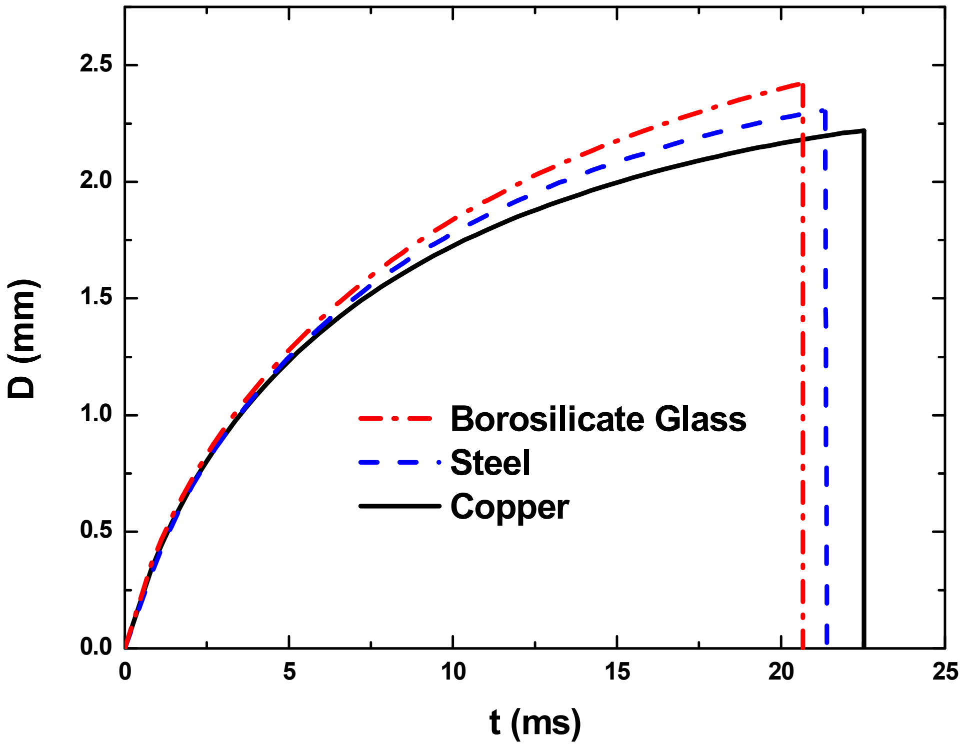

Figure 5.9 Growth history for different wall materials with 0.3 *mm* wall thickness under identical conditions: $q_{w,in}$ = 1.1 W/cm^2 and ΔT_{nuc} = 6 ^oC at one atmosphere pressure with $\varphi = 35^o$.

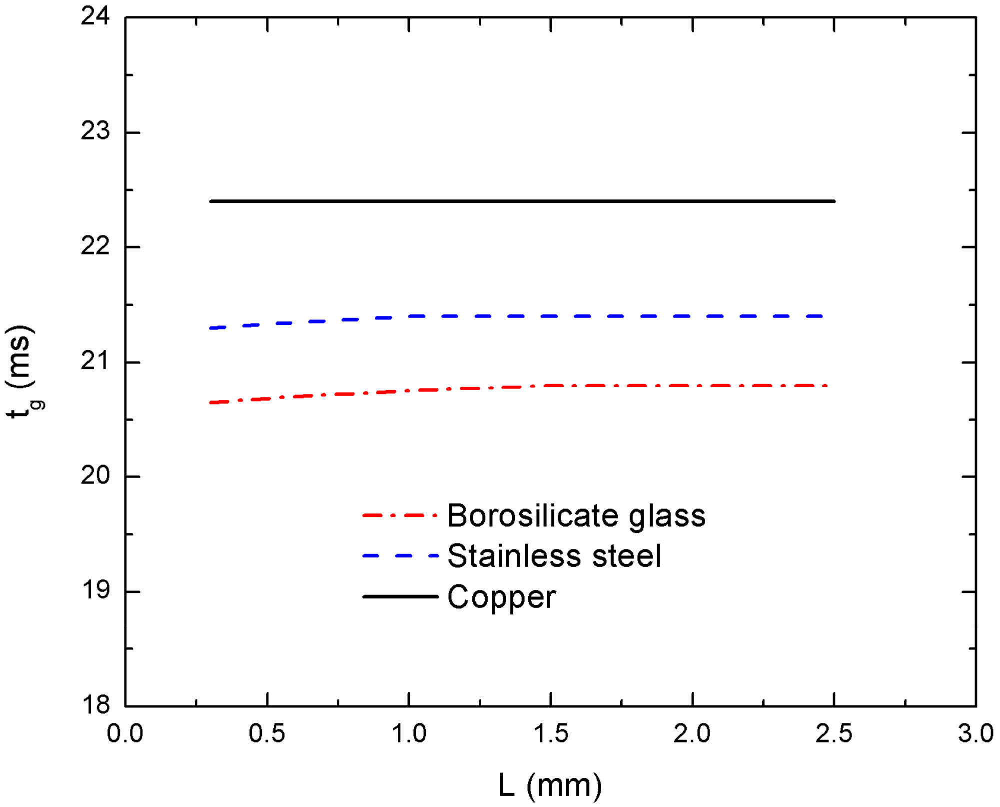

Figure 5.10 Growth period as a function of solid substrate thickness for water boiling on different materials with $q_{w,in}$ = 1.1 W/cm^2 and ΔT_{nuc} = 6 ^oC and $\varphi = 35^o$.

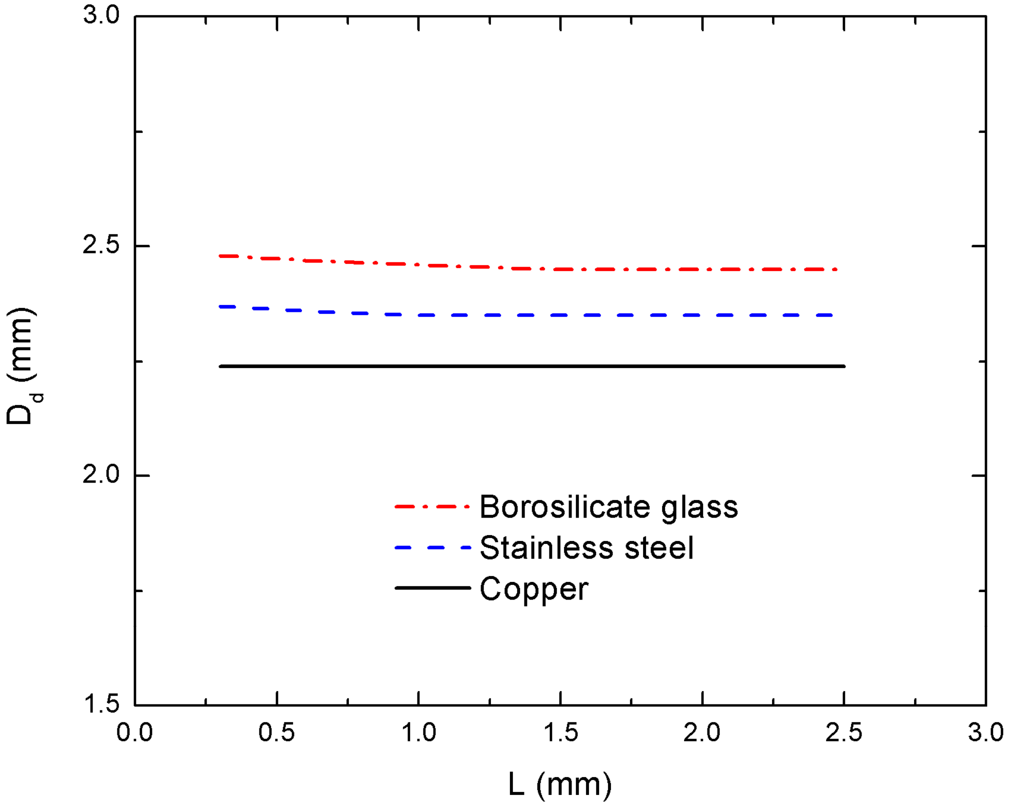

Figure 5.11 Bubble departure diameter as a function of solid substrate thickness for water boiling on different materials with $q_{w,in}$ = 1.1 W/cm^2 and ΔT_{nuc} = 6 ^oC and φ = 35^o.

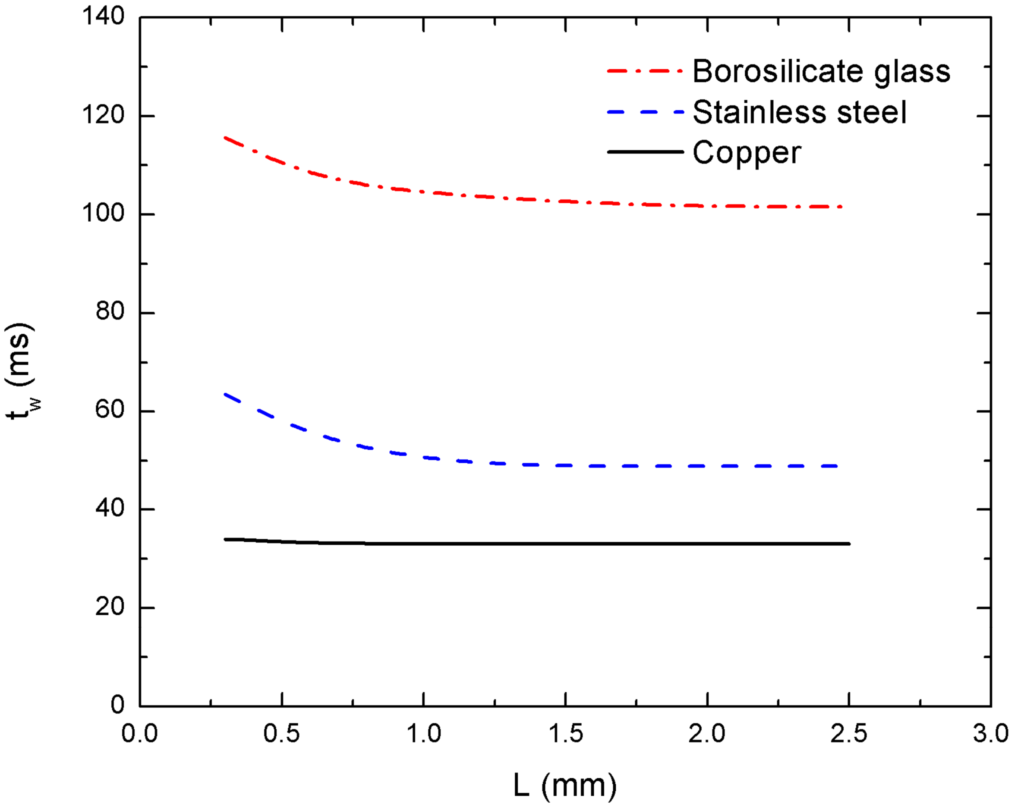

Figure 5.12 Waiting time as a function of solid wall thickness for different materials with $q_{w,in}$ = 1.1 W/cm^2 and ΔT_{nuc} = 6 ^oC at one atmosphere pressure and $\varphi = 35^o$.

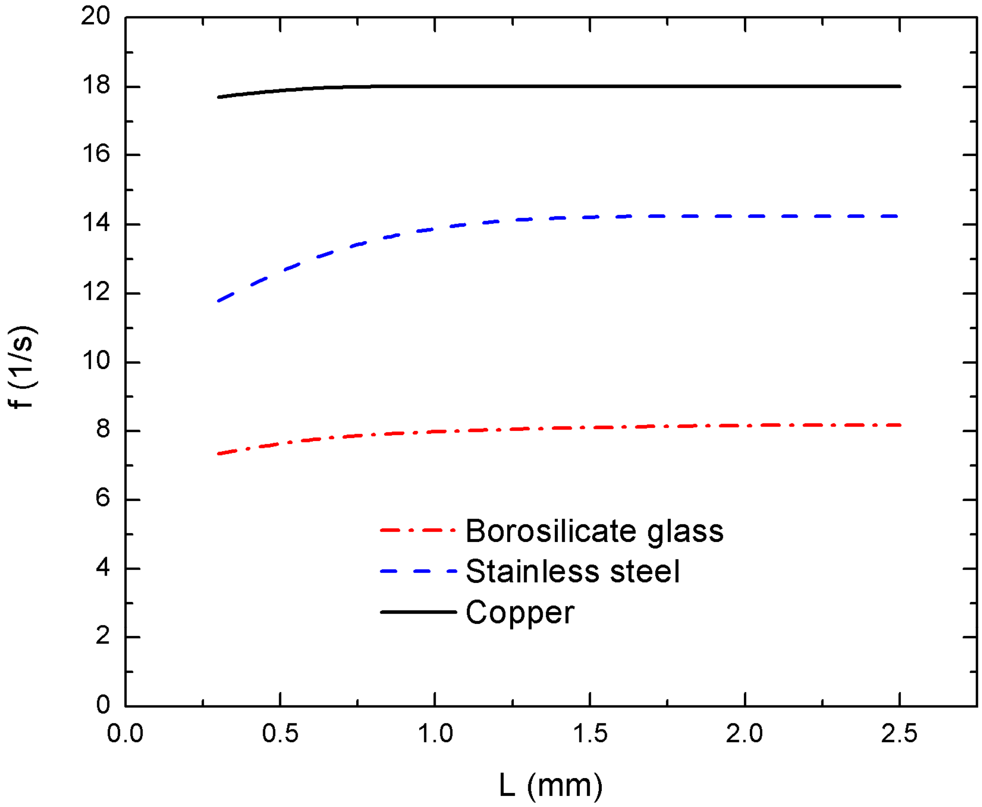

Figure 5.13 Bubble release frequency as a function of solid wall thickness for different materials with $q_{w,in}$ = 1.1 W/cm^2 and ΔT_{nuc} = 6 ^oC at one atmosphere pressure and $\varphi = 35^o$.

5.1.5 Effect of Substrate Thickness and Properties on Heat Transfer

Figure 5.14 shows the heat flux at the surface as the simulation proceeds from initial to quasi steady-state conditions. As explained previously, the nucleation criterion used is based on the cavity superheat. When that superheat reaches a prescribed value—$\Delta T_{nuc} = 6\ ^{o}C$ in this case—a new bubble embryo is placed over the cavity. The first noticeable effect of the application of a constant heat flux boundary condition is that as the cycles evolve the waiting time changes before reaching a steady value. This is simply due to the uncertainty in the specification of initial conditions. The area- and cycle-averaged wall heat flux also varies slightly before settling at the same value as the input heat flux. The behavior observed in Figure 5.14 indicates that initially the solid is actually being heated as the input heat flux is higher than the area- and cycle-averaged output. Eventually, the output becomes larger than the input and the wall cools back down before reaching a cycle-to-cycle steady value that is equal to the input value.

It was shown in the previous section that increasing wall thermal conductivity and diffusivity results in slower growth rates and smaller bubbles. It was further shown that improving wall thermal conductivity and diffusivity results in a shorter waiting period. One of the consequences of a shorter waiting period is that the thermal boundary layer has less time to develop before the next cycle begins. The boundary layer thickness and its effect on bubble growth can be seen on Figure 5.15. If surrounded by a thinner thermal boundary layer, a bubble will grow more slowly than if surrounded by a thicker thermal boundary layer. Additionally, more heat transfer will take place directly from the solid wall to the liquid if the thermal layer is thinner. The first set of frames shows the bubble embryo shortly after nucleation and the temperature contours for copper, steel, and borosilicate glass. The temperature contours show clearly the difference in boundary layer thickness at nucleation for the different solid substrates. The second set of frames shows the bubbles approximately half way through the growth cycle, and the last set of frames shows the bubbles right before they depart. Right before departure, the size difference is noticeable, and so is the fact that for borosilicate glass which had the thickest boundary layer at nucleation, the bubble is still surrounded by superheated fluid even as it detaches from the wall.

The first three frames in Figure 5.16 show the liquid-vapor interface at various times during bubble growth and after bubble departure for copper, steel, and borosilicate glass. The next three frames show the corresponding local wall heat flux as a function of the radial location at the same times during bubble growth and after bubble departure for the three different substrate materials. As the bubble grows and its base expands, the location where the rate of heat removal peaks moves radially out with the motion of the interface over the solid wall. The same is observed as the bubble base shrinks after reaching a maximum value. Quantitatively, the heat flux is of the order of 10^{-2} W/cm^2 where the solid is dry, 10^{-1} W/cm^2 where the solid is in contact with the superheated liquid boundary layer, and 10^{-3} W/cm^2 near the three phase point. During bubble growth, the actual peak heat flux can reach close to 150 W/cm^2 while the heat flux averaged over the entire surface of the disc remains at 1.5 W/cm^2.

Due to the sharpness of the heat flux peak and its motion as time passes, any single location on the solid surface close to the cavity site will be exposed to abrupt temperature fluctuations as is shown in the last three frames of Figure 5.16. The curves representing the surface temperature as a function of radius after departure show the absence of a sharp temperature drop in the absence of the evaporating microlayer during bubble growth. However, the less pronounced temperature drop affects a visibly larger surface area due to the liquid that rushes in to replace the bubble after departure.

Figure 5.17 shows the heat transfer coefficient predicted by the present simulations as a function of substrate thickness. The three different materials are also shown to illustrate the effect of the thermophysical properties of the substrate. Two trends can be observed in this figure. The first trend is that for all three different substrate materials the heat transfer coefficient is seen to decrease as the thickness increases. The figure also shows that, as thermal conductivity and diffusivity of the substrate increases, the heat transfer coefficient decreases. However, it should be noted that both trends are very weak. The highest change in heat transfer coefficient spanning all thicknesses and materials shown (occurring between the 0.3 *mm* thick borosilicate glass substrate and the 2.5 *mm* copper substrate) is only 4 percent.

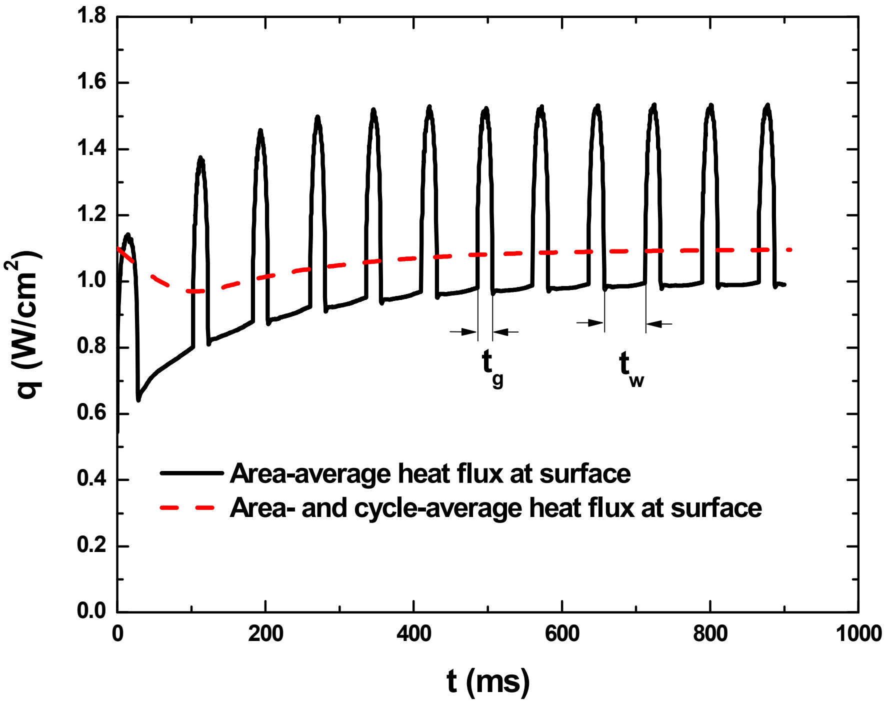

Figure 5.14 Variation of heat flux with time for various bubble cycles using a 1 mm thick steel plate and constant $q_{w,in}$ = 1.1 W/cm^2 with ΔT_{nuc} = 6 ^oC at one atmosphere pressure and φ = 35^o.

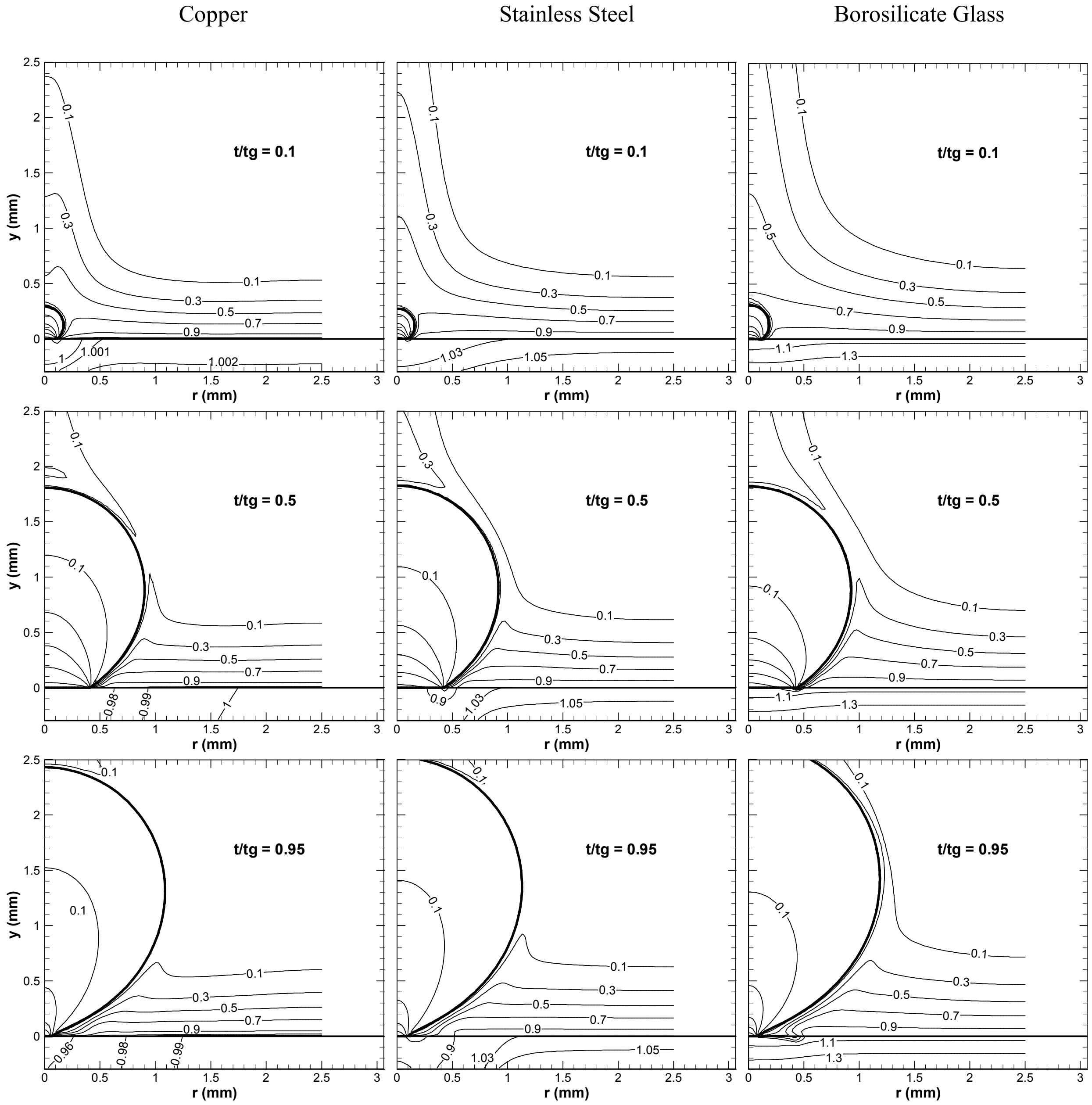

Figure 5.15 Bubble growth and temperature contours for copper, steel, and borosilicate glass at nucleation, midway through the growth cycle, and right before departure. The phase interfaces are shown in bold. The contact angle is 35^o, the input heat flux is 1.1 *W/cm*^{2} and the nucleation superheat is 6 ^{o}*C*.

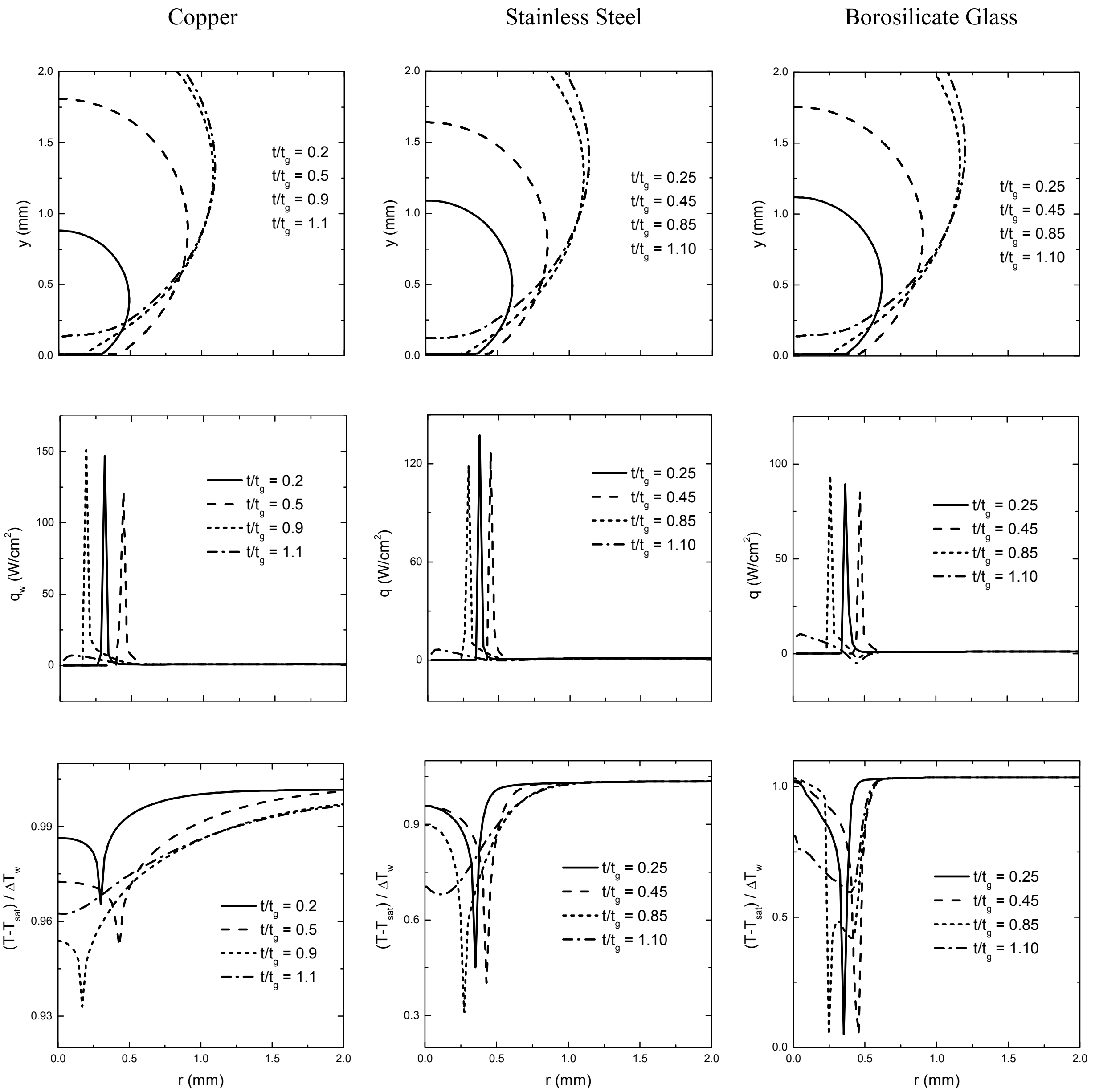

Figure 5.16 Local wall superheat and heat flux as a function of radial location at different times during bubble growth and after departure for 0.3 *mm* copper, steel, and borosilicate glass. The contact angle is 35^o, the input heat flux is 1.1 *W/cm^2* and the nucleation superheat is 6 ^{o}*C*.

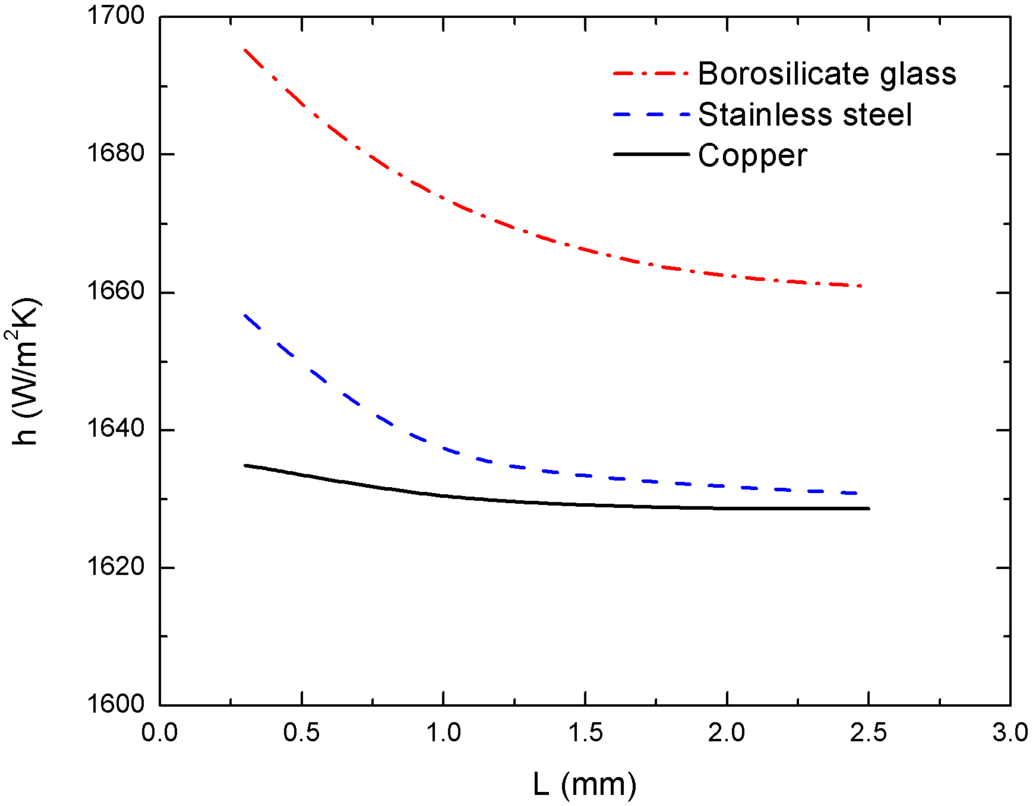

Figure 5.17 Dependence of heat transfer coefficient on solid substrate thickness for different substrate materials. Heat transfer coefficient averaged over the area of a circular heater with $R = 2.5\ mm$. Fluid properties based on water at one atmosphere pressure with $\varphi = 35^o$, $q_{w,in} = 1.1\ W/cm^2$ and $\Delta T_{nuc} = 6\ ^oC$.

5.1.6 Effect of Gravity on Bubble Dynamics

Figure 5.18 shows the growth history for water boiling on a 1 *mm* thick copper surface at one atmosphere pressure and reduced gravity, $g/g_e = 10^{-2}$. In comparison to the observations at Earth normal gravity, the growth period increases by two orders of magnitude and the departure diameter increases by one order of magnitude. However, the change in gravity only has second order effects on the solid substrate's recovery time. Therefore, the change observed in the waiting period (~ 20 *ms*) is almost insignificant when compared to those of the growth period and departure diameter.

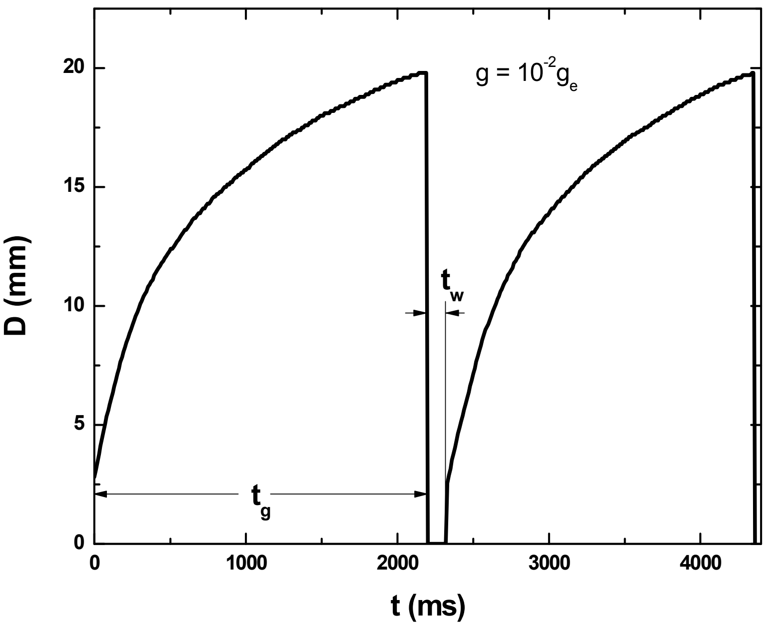

Figure 5.18 The effect of gravity on growth and waiting times for water boiling on a 1 *mm* thick copper surface at one atmosphere pressure, $\varphi = 35^o$, $q_{w,in} = 0.36$ *W/cm*^{2} with $\Delta T_{nuc} = 6\ ^oC$.

5.2 Effects of varying contact angle

In the preceding sections the phenomenon of local surface temperature fluctuations during single bubble nucleate pool boiling was shown through the coupled solution of conjugate conduction in the solid substrate. Additionally, several different parameters were varied and their effects on recovery periods were analyzed. However, the contact angle was held constant throughout. In the following sections the effect of varying contact angle will be explored in depth starting with some comparisons between numerical and experimental results that lend credibility to the numerical tool being employed.

5.2.1 Comparisons between numerical and experimental results

Nam et al. (2009) performed experiments to study the single bubble dynamics associated with water boiling on a hydrophobic surface in which the contact angle varied between 118 and 134^{o}. The authors utilized a similar numerical tool as the one being employed presently (based on the code originally developed by Son et al. (1999)) to simulate the process and the results were compared. The necking and eventual pinching of the bubble near its base observed in the experiments was also predicted by the simulations. Thus, the level set method was shown to be capable of predicting the bubble shape for large contact angles in which the bubble never fully departs from the surface. Growth rates and departure diameters were also predicted well by the simulations.

More recently, Nam et al. (2011) developed a similar experiment to study the single bubble dynamics of water boiling on a silicon surface which was treated to reduce contact angle rather than increase it. Despite using the same fluid, the result was a superhydrophilic surface with a measured static contact angle of less than 10^o. Figure 5.19 shows a comparison between the bubble growth history obtained in the experiment and that predicted by the numerical simulations. The simulations predict a faster initial growth than what was observed in the experiment. The same discrepancy can be seen in the bubble base diameter data. However, after the first millisecond, the bubble equivalent diameters match remarkably well. The departure diameter predicted is within 1 percent of the experimental result and the final growth period is underpredicted by less than 10 percent. Adjacent comparisons of bubble shapes and sizes between experiments and simulations are shown at 4 different times in Figure 5.20. It is seen that, in addition to predicting growth rate, growth period, and departure diameter, the simulations also capture the bubble shape well.

For the range of contact angles studied experimentally, bubble departure diameters vary by an order of magnitude and growth periods by up to three orders of magnitude. Bubble shapes vary significantly, becoming more spherical as the bubble departure diameters become smaller. Additionally, the departure mechanism changes for large enough contact angles in which a nucleus remains at the heater surface. The comparisons between experimental data and results from numerical simulations show that the approach being employed presently is capable of predicting all the range of single bubble dynamics for a wide range of contact angles.

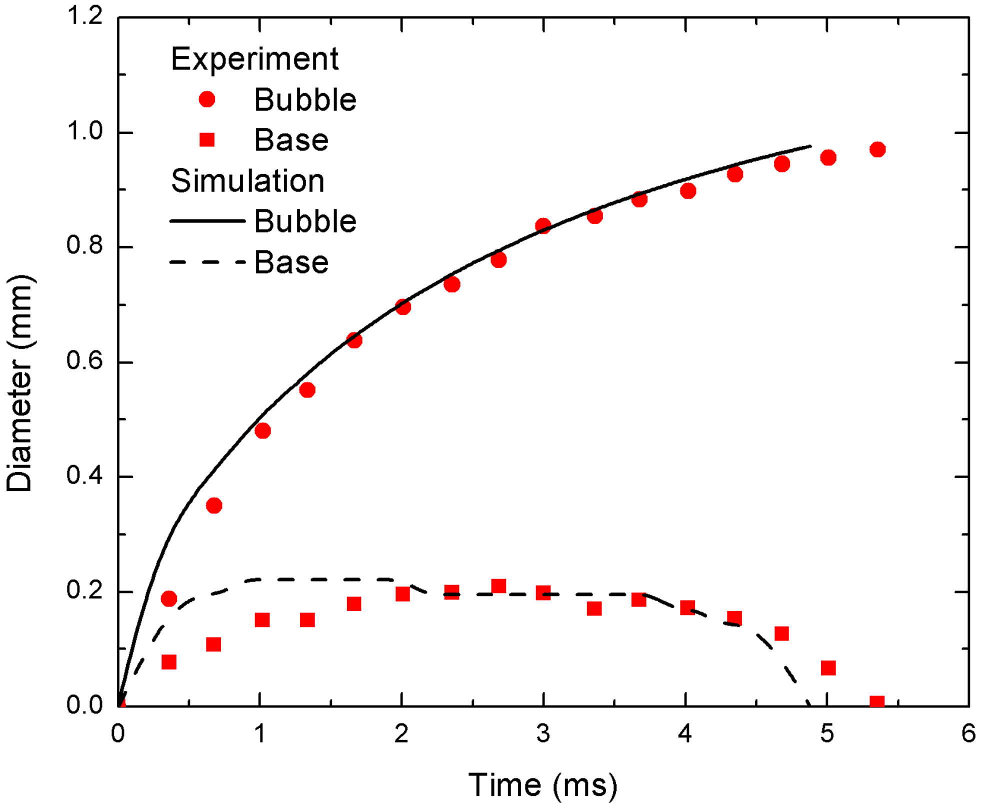

Figure 5.19 Comparison between numerically predicted and experimentally obtained bubble growth histories and base diameters (Nam et al., 2011) for $\varphi = 10^o$, $\Delta T_w = 5.3\ ^oC$, and $\Delta T_{sub} = 0\ ^oC$.

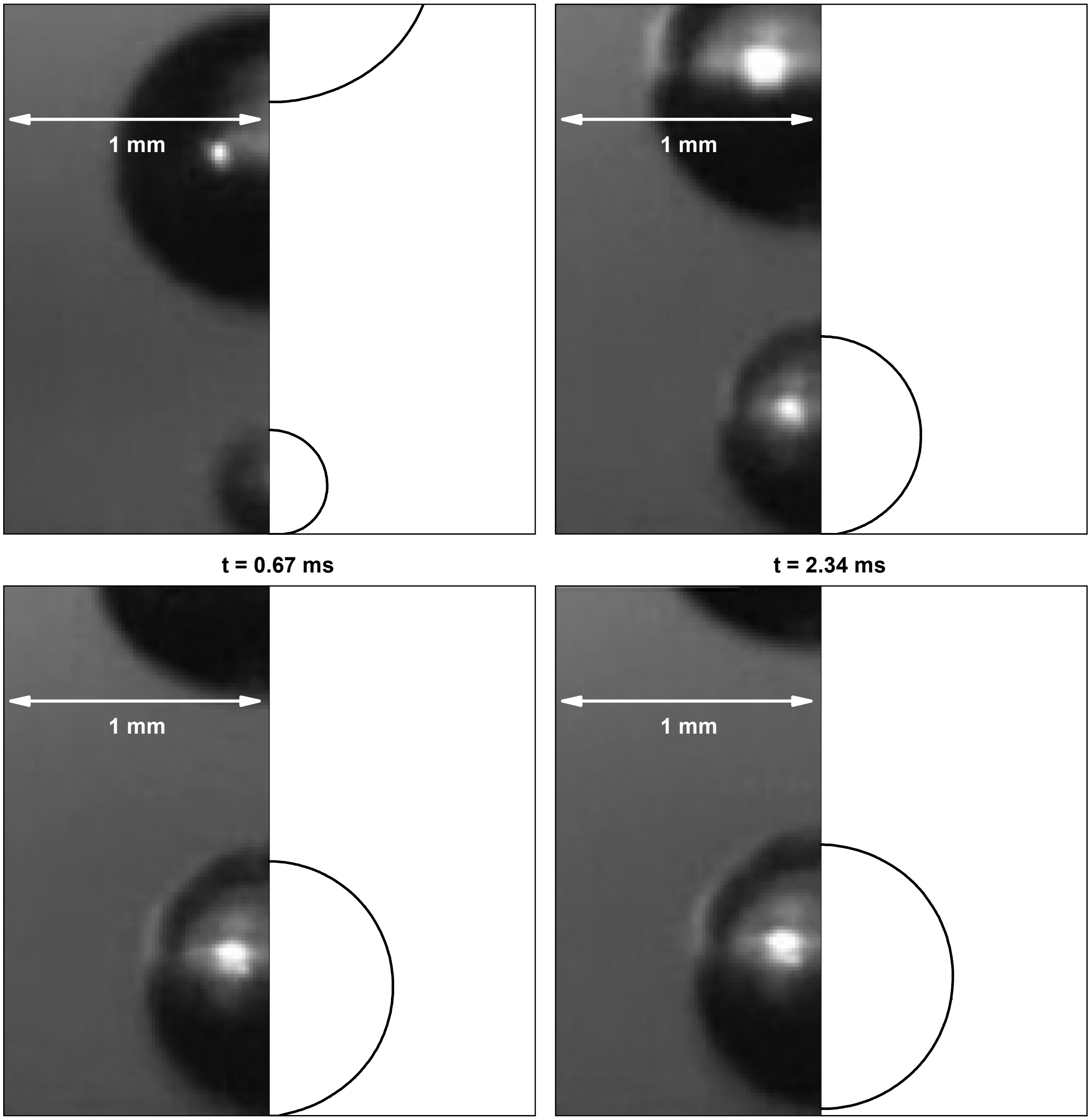

t = 0.67 ms

t = 2.34 ms

t = 4.34 ms

t = 5.34 ms

Figure 5.20 Bubble shape and size comparison between numerical simulations and experimental results for water boiling on superhydrophilic surface (Nam et al., 2011) for $\varphi = 10^{o}$, $\Delta T_w = 5.3\ ^{o}C$, and $\Delta T_{sub} = 0\ ^{o}C$.

5.2.2 Effect of contact angle on bubble dynamics

In order to study the effects of contact angle on bubble dynamics, several simulations were performed in which all conditions remained identical but the contact angle was varied parametrically. Calculations were also carried out for solids with different thicknesses while varying the contact angle parametrically. All simulations were performed using the properties of water boiling on a stainless steel surface at one atmosphere pressure.

Figure 5.21 shows the growth period as a function of contact angle predicted from the simulations for water boiling on stainless steel surfaces of different thicknesses at one atmosphere pressure. In these simulations the heat flux supplied was 1.1 W/cm^2 and the nucleation superheat was 6 ^oC. The growth period variation is nonlinear as suggested by the experimental results shown in the preceding section. As the bubble grows, an increasing portion of its vapor-liquid interface pushes itself out of the superheated layer of liquid adjacent to the wall and comes into contact with the bulk liquid which is at saturation conditions. Although the base of the bubble continues to increase, the area over which evaporation occurs becomes proportionally smaller compared to the total surface area of the bubble. This results in the nonlinearity observed in the growth period. The effect of wall thickness variation is also shown in the figure but the simulations predict almost no dependence of growth period on wall thickness. Calculations performed for wall thicknesses as low as 0.1 *mm* and as high as 10 *mm* result in growth periods within 10 percent of those shown for L = 0.5 *mm*.

Bubble departure diameter as a function of contact angle predicted by both Fritz (1935) and the present numerical simulations are shown in Figure 5.22. The simulated conditions were the same as above: water boiling on stainless steel surfaces of various thicknesses at one atmosphere pressure with $q_{w,in}$ = 1.1 W/cm^2 and ΔT_{nuc} = 6 ^oC. Assuming all experimental conditions and fluid properties remain the same, the semi empirical correlations given in section 1.3 (including Fritz) predict a linear variation of bubble departure diameter with contact angle. Figure 5.22 shows that the numerical simulations also predict an almost exactly linear relationship between bubble departure diameter and contact angle for contact angles ranging from 20 to 55^o.

Figure 5.23 shows bubble shapes and sizes for the same simulations with contact angles varying from 20 to 55^o. Although actual growth period is not the same for the various contact angles, the comparisons in Figure 5.23(a) are made based on half of the total growth period for each bubble. The size and shape differences are clear with increasing contact angles leading to larger bubbles and larger bubble base diameters. Figure 5.23(b) shows the bubble shapes and sizes immediately prior to departure. The differences are also clear, with increasing contact angle leading to less spherical bubbles at departure.

Due to local cooling of the heater surface during bubble growth, the dependence of the waiting period on the contact angle is more complex than that of the departure diameter and growth period. The effect of wall thickness can be eliminated by simply making it thick enough such that the temperature fluctuations at the heater surface cannot be felt at the bottom of the wall where the heat flux is applied. In such a case, making the wall thicker would have no effect on the temperature recovery of the heater surface or on the waiting period. Although the dependence of the waiting period on contact angle remains nonlinear, Figure 5.24 shows that the waiting period increases monotonically with increasing contact angle in the case of a thick wall. In thinner walls, however, the proximity of the bottom boundary where heat flux is supplied affects the recovery time.

The bubble release frequency is shown in Figure 5.25 as a function of contact angle for the same case of water boiling on a stainless steel surface of various thicknesses. The bubble release frequency is seen to increase slightly with increasing thickness but the dependence is weak. As the contact angle increases, the bubble release frequency decreases. This behavior is obvious considering that both the growth and waiting periods generally increase with increasing contact angle. The exception of the peaking waiting period for the 0.5 *mm* thick substrate does not affect the frequency appreciably because the drop in waiting period after the peak is small. The semi-empirical correlation of Mikic and Rohsenow (1969) given in section 1.4 predicts higher bubble release frequencies as shown in the figure. However, the dependence on contact angle predicted is similar between the simulations and correlation.

It should be noted that the results are only shown here for contact angles up to 55^o because at larger contact angles an entirely different bubble release pattern is observed. At a contact angle of 65^o, for example, after the first bubble detaches from the wall, the surface temperature at the cavity site is high enough that the next bubble immediately nucleates. After the second bubble departs, the cavity site is no longer hot enough for immediate nucleation of a third bubble. A brief waiting period follows the departure of the second bubble in which the wall temperature recovers. The cycle repeats itself indefinitely with cycles of two consecutive bubbles being released followed by a waiting period. If the contact angle is increased further, the number of consecutive bubbles increases before the recovery of the temperature at the cavity site leads to an appreciable waiting period. This phenomenon of consecutive bubble releases prior to each waiting period is outside the scope of the present work and is therefore not explored in depth presently.

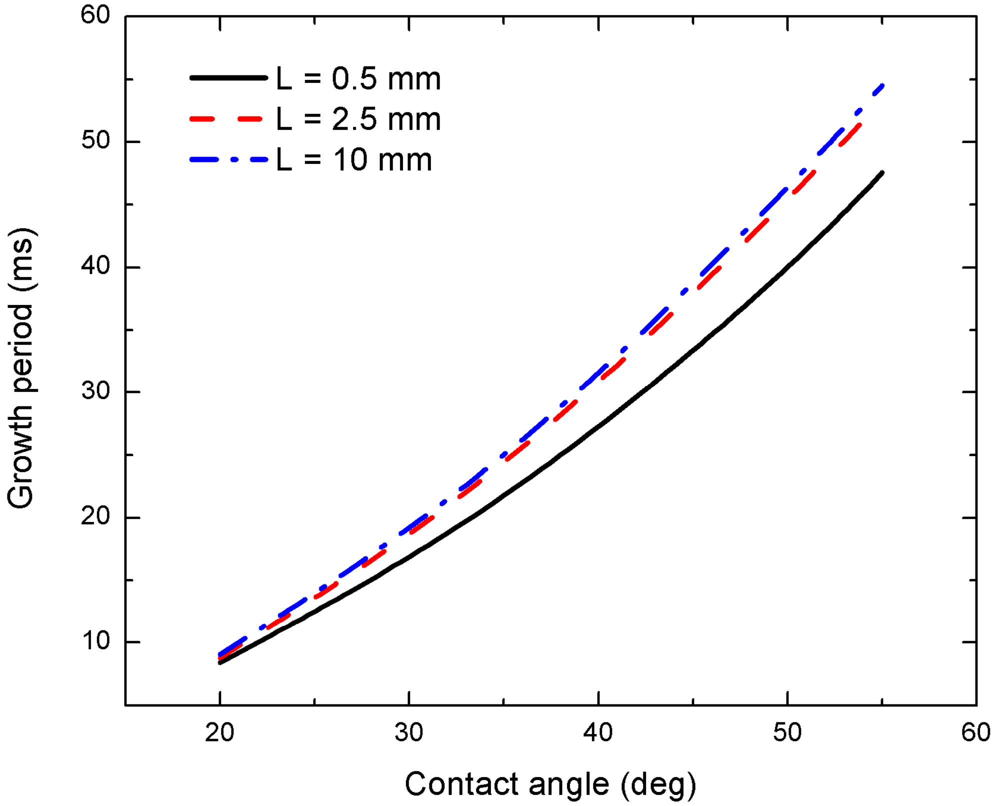

Figure 5.21 Growth period as a function of contact angle for water boiling on 0.5 and 2.5 *mm* thick stainless steel surfaces at one atmosphere pressure with $q_{w,in} = 1.1$ W/cm^2 and $\Delta T_{nuc} = 6$ ^oC.

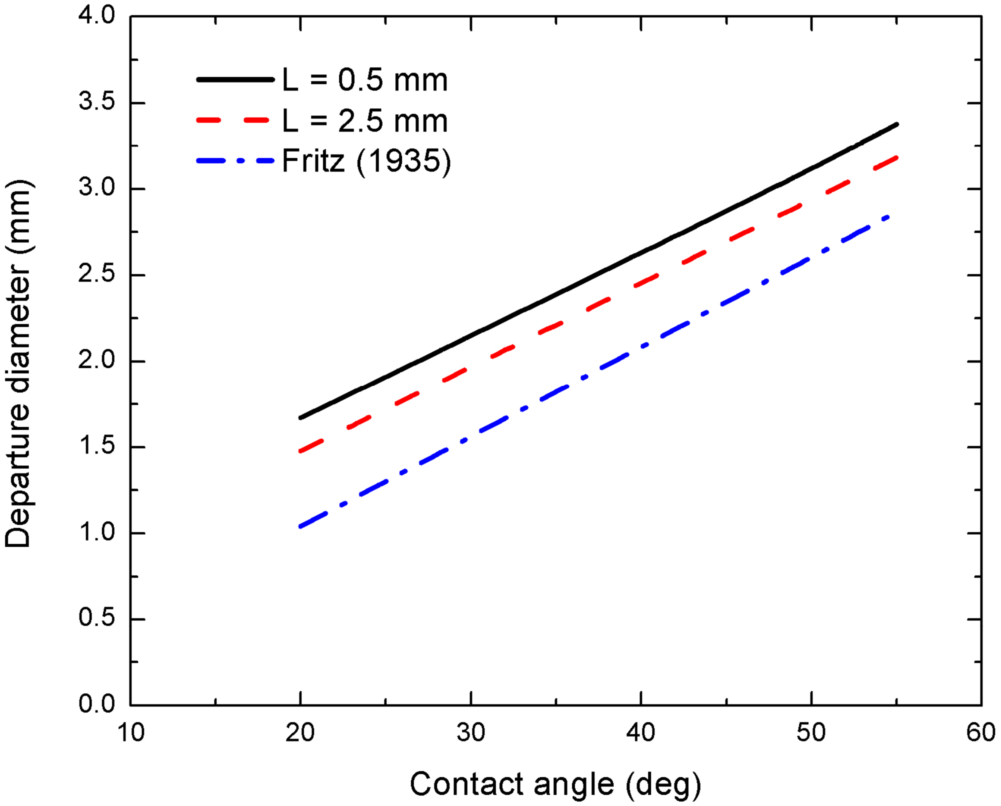

Figure 5.22 Departure diameter as a function of contact angle predicted by Fritz (1935) and the present numerical simulations of water boiling on 0.5 and 2.5 *mm* thick stainless steel substrates with $q_{w,in}$ = 1.1 W/cm^2 and ΔT_{nuc} = 6 °*C*.

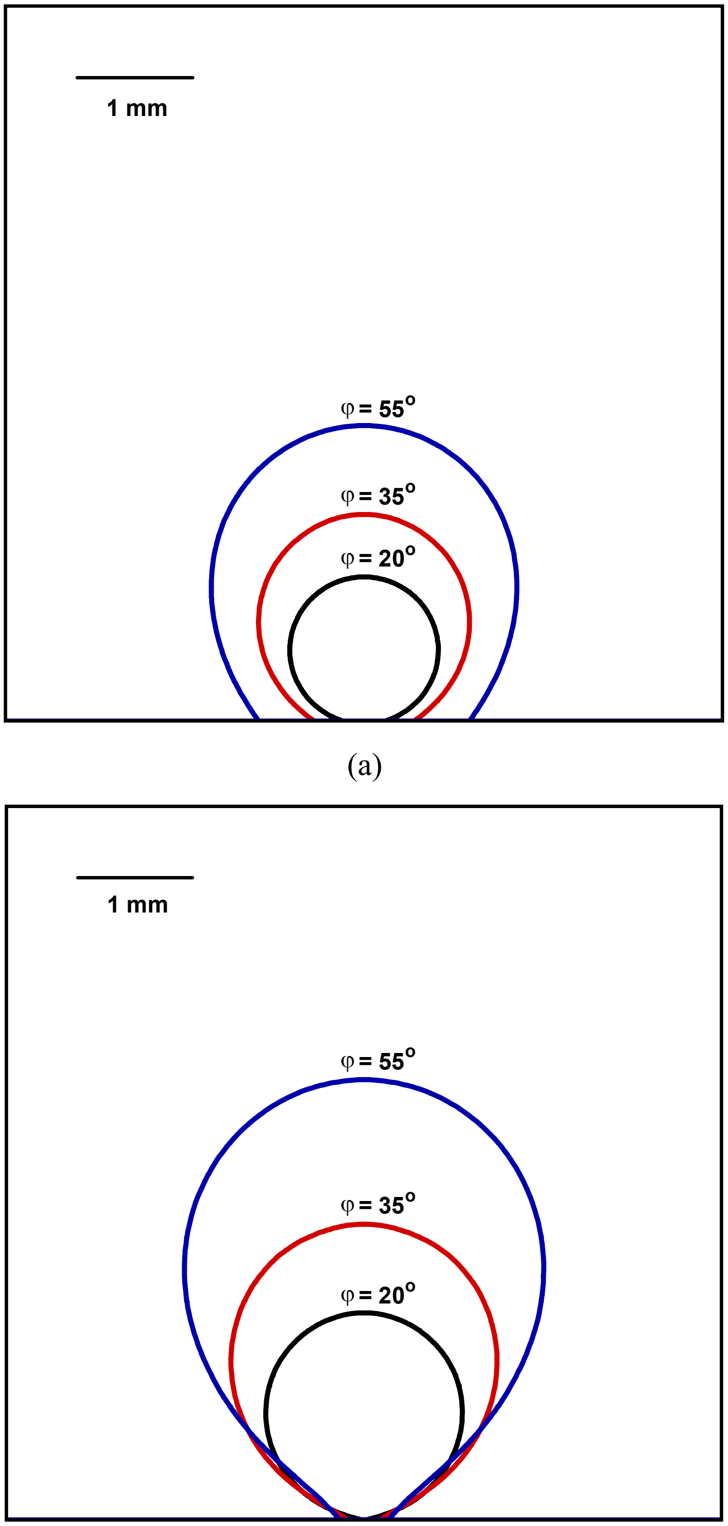

Figure 5.23 Bubble shapes for various contact angles at (a) approximately half way through their growth cycles and (b) immediately prior to departure. Fluid is water boiling on a 0.5 *mm* thick stainless steel substrate with $q_{w,in} = 1.1\ W/cm^2$ and $\Delta T_{nuc} = 6\ ^{o}C$.

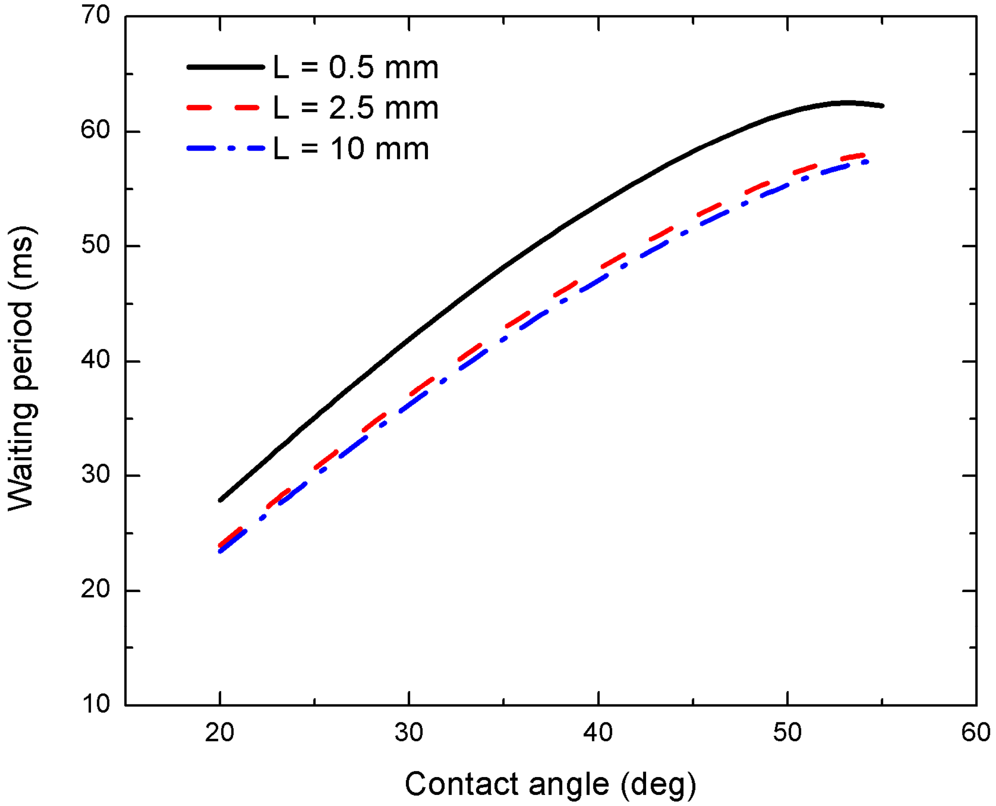

Figure 5.24 Waiting period as a function of contact angle for water boiling on stainless steel substrates of various thicknesses and with $q_{w,in} = 1.1\ W/cm^2$ and $\Delta T_{nuc} = 6\ ^oC$.

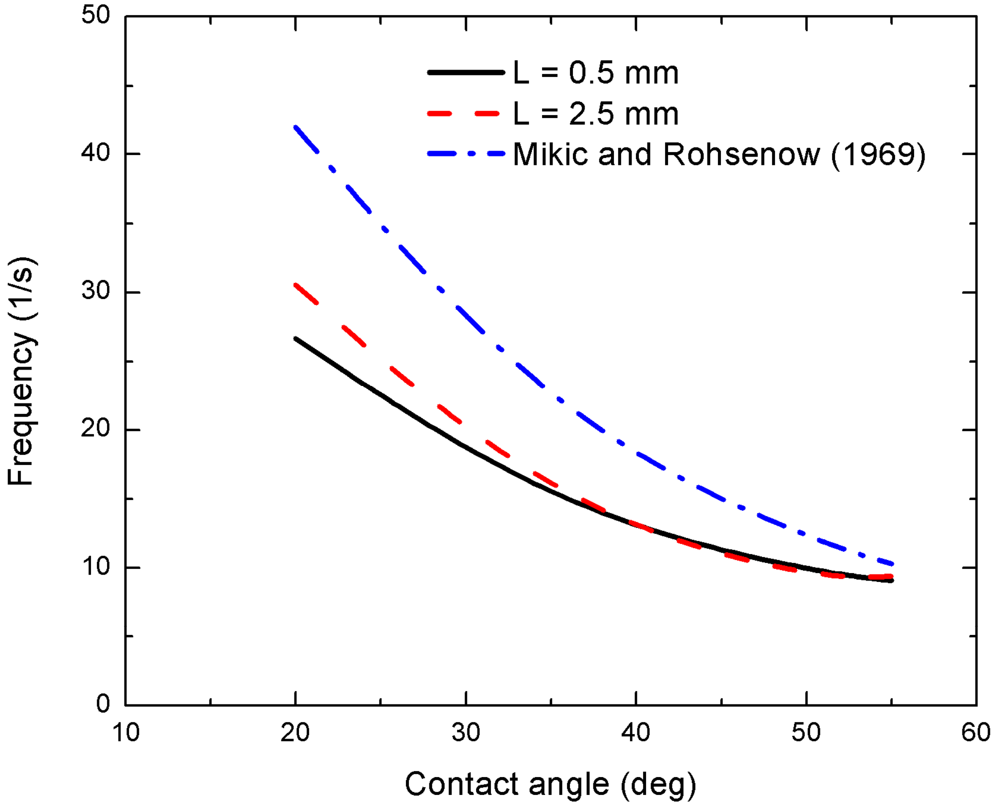

Figure 5.25 Bubble release frequency as a function of contact angle for water boiling on stainless steel substrates of various thicknesses and with $q_{w,in}$ = 1.1 W/cm^2 and ΔT_{nuc} = 6 ^oC. Predictions by Mikic and Rohsenow (1969) are also included for comparison.

5.2.3 Thermal response of the wall

Despite the complexities in the behavior of the waiting period shown previously, it was shown that for any given contact angle the waiting period goes down with increasing wall thickness. This dependence will be justified by first focusing on a single contact angle of 50^o and analyzing the thermal response of the wall carefully as follows.

Figure 5.26 shows the bubble interface immediately after departure as well as the isotherms in all three phases for water boiling on stainless steel for two different wall thicknesses (0.5 and 2.5 *mm*). Figure 5.27 shows the accompanying radial temperature distribution and vertical heat flux at a depth of 0.5 *mm* for both cases. It can be seen that the local temperature drop 0.5 *mm* below the cavity site for the thinner substrate is almost twice as that of the thicker substrate. The increased temperature drop suggests a longer recovery time after departure for the thinner case. Additionally, it can be seen that the vertical heat flux distribution at the same depth is much lower in the 0.5 *mm* substrate, being the imposed 1.1 W/cm^2 compared to a peak value of approximately 1.9 W/cm^2 for the 2.5 *mm* substrate. The peaking observed for the thicker substrate is a consequence of the increased thermal mass around the area where temperature drops are highest. This simple comparison of the vertical heat flux present at the same depth for the two different substrate thicknesses provides further insight into the mechanism by which the added thermal mass results in reduced recovery times. Therefore, keeping the contact angle constant at 50^o while altering the solid substrate's thickness, it becomes evident that the thicker solid will recover faster due to the extra stored energy which tends to equalize the temperature distribution through conduction.

Next, the positive correlation between waiting period and contact angle can also be justified by analyzing the thermal response of the wall. Figure 5.28 shows the bubble interface and the temperature field in all three phases immediately prior to bubble departure (left) and immediately after bubble departure (right) for various contact angles of water boiling on a 0.5 *mm* thick stainless steel surface. Figure 5.29(a) shows the radial surface temperature distribution 1 *ms* prior to departure of the bubble. The radius is measured outwards from the cavity site. At the cavity site, the wall superheat is less than 3 ^oC for the smallest contact angle ($\varphi = 20^o$). This is in sharp contrast with the cavity superheat for the largest contact angle ($\varphi = 50^o$) 1 *ms* prior to bubble departure of approximately 6.1 ^oC. During bubble growth, the size of the dry spot surrounding the cavity site increases with increasing contact angle. Increasing contact angles additionally result in longer growth periods, as shown previously. As a result, the cavity site is dry and consequently exposed to significantly reduced heat transfer coefficients for a longer period of time. The combined effect is a significant increase in local temperatures at the cavity site with increasing contact angle during bubble growth as shown in Figure 5.29(a).

The higher cavity site temperature immediately prior to departure indicates that recovery times will be shorter once the bubble has departed. However, at the last stages of bubble growth when the bubble base diameter is shrinking, cold liquid rushes in to fill the volume being vacated by the departing bubble. Larger departing bubbles (due to larger contact angles) result in a larger portion of the heater surface being exposed to the cold liquid and a consequent higher rate of heat transfer during the waiting period. Therefore, the changes in bubble shape and size that result from varying the contact angle lead to two competing phenomena that affect waiting time: (1) larger bubble leads to higher temperature at the cavity site during bubble growth and immediately prior to departure, and (2) larger bubble increases heat transfer rate near the cavity site immediately after departure.

Figure 5.29(b) shows the radial surface temperature distribution 1 *ms* after bubble departure. Compared to 1 *ms* prior to bubble departure, the cavity site temperature in this case shows the same trend of increasing temperature with increasing contact angle. However, the differences are smaller, peaking at a 1.2 ^{o}C difference between $\varphi = 20^{o}$ and $\varphi = 50^{o}$, compared to the previous difference of 3.1 ^{o}C. The result is that, despite the higher cavity temperature during bubble growth and immediately after departure, the recovery period is longer for higher contact angles due to improved heat transfer after bubble departure.

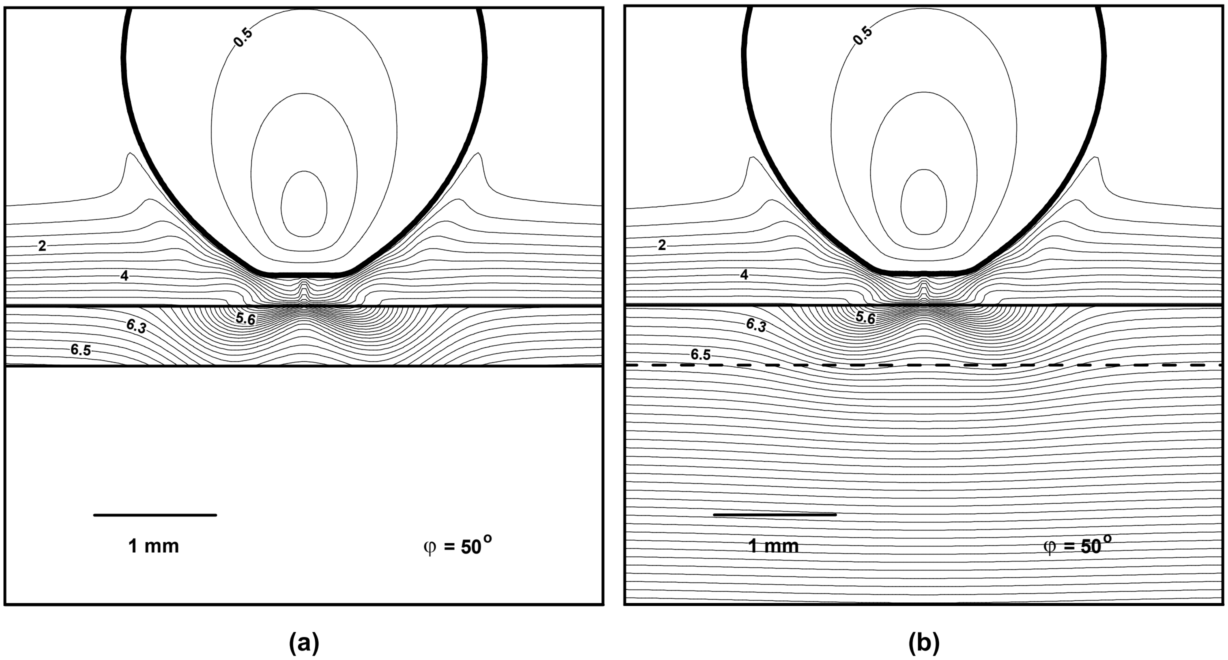

Figure 5.26 Isotherms and bubble interface 1 *ms* after bubble departure for water boiling on stainless steel with L = 0.5 *mm* (left) and L = 2.5 *mm* (right) for $\varphi = 50^o$ and with $q_{w,in}$ = 1.1 W/cm^2 and ΔT_{nuc} = 6 ^oC. Isotherm intervals are 0.5 ^oC in the fluid and 0.05 ^oC in the solid substrate.

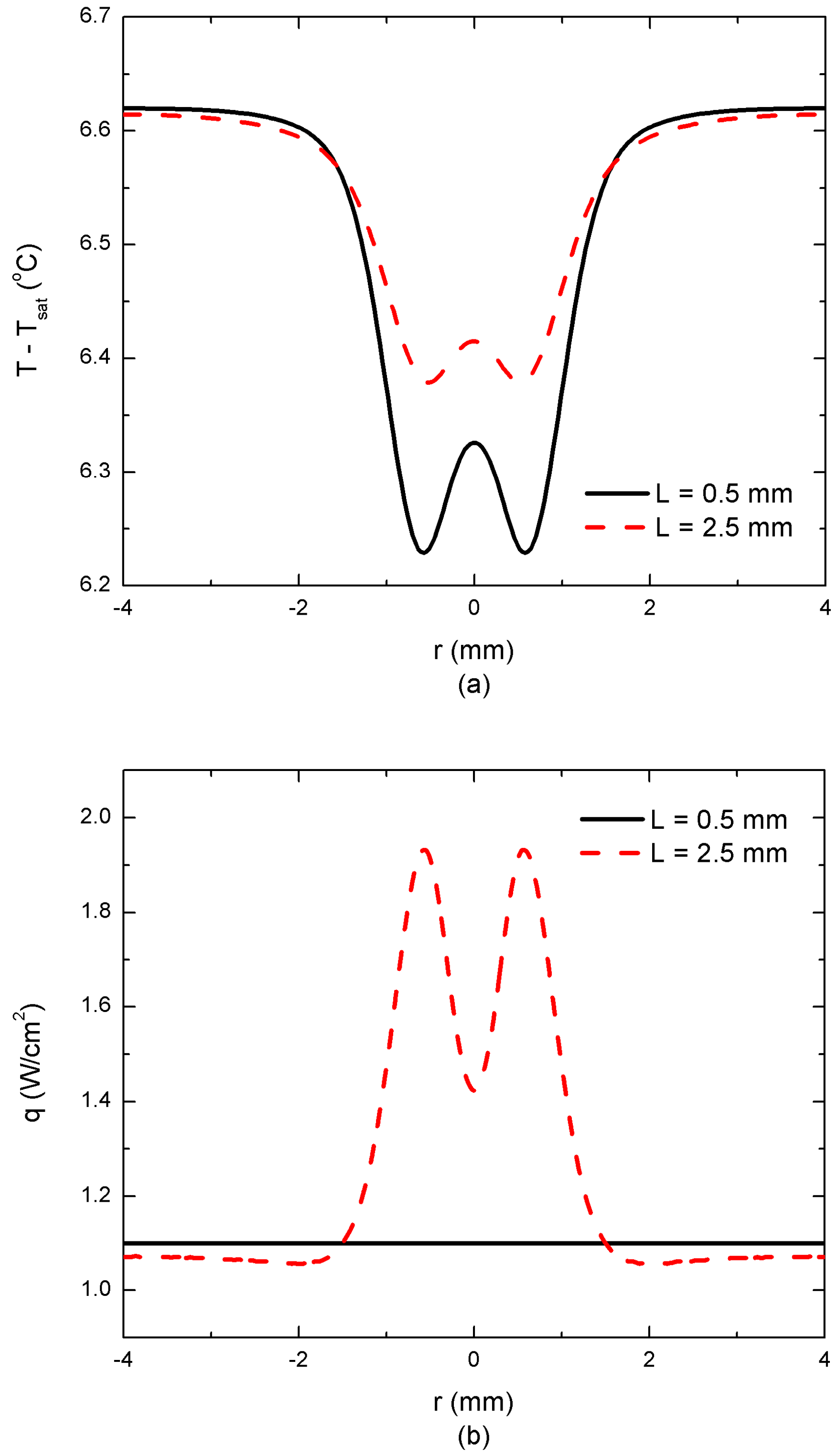

Figure 5.27 **Radial temperature distribution and vertical heat flux at depth of 0.5 *mm* 1 *ms* after bubble departure for water boiling on stainless steel with L = 0.5 *mm* and L = 2.5 *mm* for $\varphi = 50^{\circ}$ with $q_{w,in}$ = 1.1 *W/cm*^{2} and ΔT_{nuc} = 6 $^{\circ}C$.**

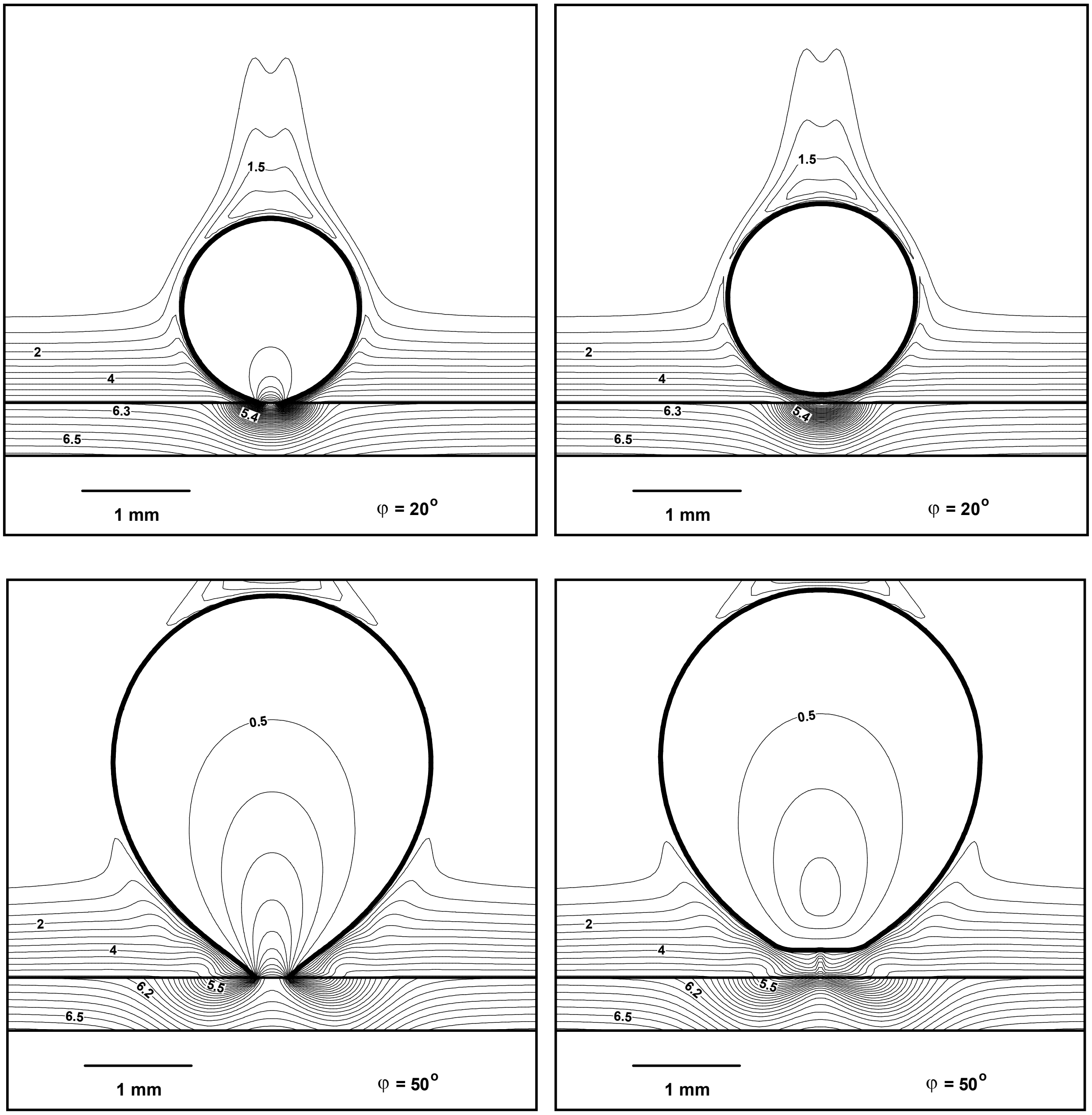

Figure 5.28 Isotherms and bubble interface just prior to bubble departure (left) and just after bubble departure (right) for various contact angles on 0.5 *mm* thick stainless steel surface with $q_{w,in}$ = 1.1 *W/cm*^{2} and ΔT_{nuc} = 6 °*C*. Isotherm intervals are 0.5 °*C* in the fluid and 0.05 °*C* in the solid.

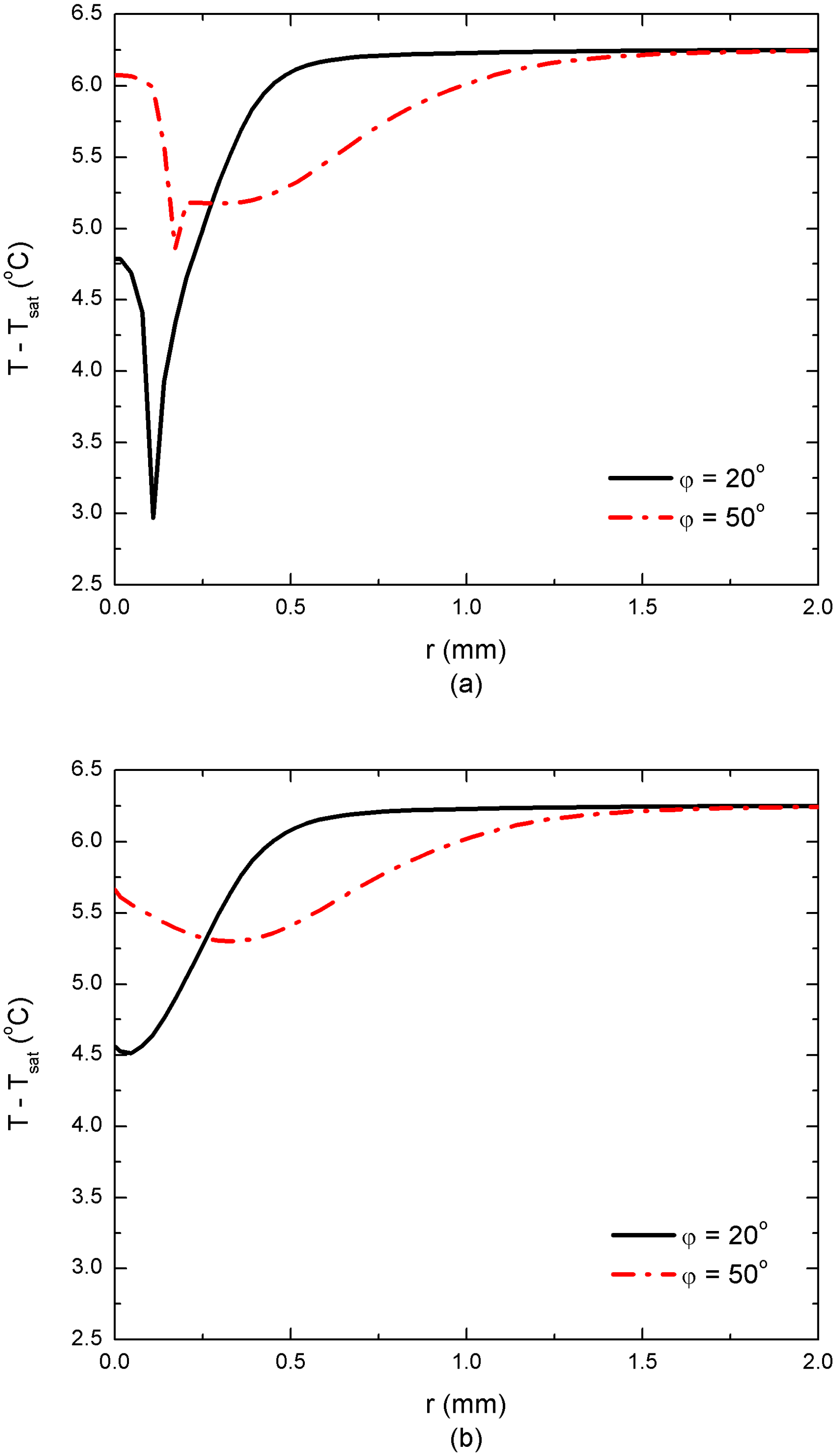

(a)

(b)

Figure 5.29 Surface temperature distribution (a) 1 *ms* prior to bubble departure and (b) 1 *ms* after bubble departure for water boiling on stainless steel substrate with L = 0.5 *mm*, $q_{w,in}$ = 1.1 *W/cm*^{2}, and ΔT_{nuc} = 6 ^oC.

5.2.4 Effect of contact angle on heat transfer

When the contact angle varies, there are several factors affecting heat transfer during bubble growth. A factor that is directly affected by the contact angle is the microlayer heat transfer. Figure 5.30(a) shows that with increasing contact angle the bubble base diameter increases but the microlayer width decreases. The resulting microlayer area at the point where bubble base diameter is maximum is shown in Figure 5.30(b). The dependence of the microlayer area on the contact angle is found to be nonlinear. The same is shown to be the case for the microlayer heat transfer rate in Figure 5.31.

Another contact angle-dependent factor that affects heat transfer rate has been mentioned previously: the dry spot increases with increasing contact angle. Since the heat transfer coefficient where the surface is dry is significantly lower than where it is wet, the rate of heat removal from the wall during bubble growth deteriorates as the dry spot grows. This behavior can be seen in the first few milliseconds of Figure 5.32 where the transient wall heat flux is shown for various contact angles. Nucleation occurs at $t = 0$ for all contact angles. For $\varphi = 20^{\circ}$, the wall heat flux is seen to be immediately aided by the growth of the bubble. In contrast, the wall heat flux remains below the input 1.1 W/cm^2 for the case of $\varphi = 55^{\circ}$ until a few milliseconds have passed. However, after approximately 20 *ms*, the wall heat transfer rate for the case of $\varphi = 55^{\circ}$ becomes higher than the smaller contact angles shown. Throughout the second half of the growth period, heat removal improves for large bubbles because of the large area affected by the bubble.

Figure 5.33 shows the heat transfer coefficient obtained as a function of contact angle for the same case of water boiling on a 0.5 *mm* thick stainless steel surface. Although the dependence is weak, the heat transfer coefficient is seen to increase with increasing contact angle. This behavior is in agreement with experimental observations reported in the literature. Wang and Dhir (1993) reported improvement in nucleate pool boiling heat transfer coefficient with increasing contact angle. However, the boiling curves reported by the authors indicate that the dependence is appreciably stronger during fully developed nucleate boiling than during partial nucleate boiling. At low wall superheats, the two boiling curves reported almost collapse on top of each other but some dependence still exists.

In the simulations performed presently, the computational domain remains constant regardless of contact angle. In order to obtain a more realistic prediction of the enhancement in heat transfer coefficient provided by increasing the contact angle, the change in nucleate site density should also be accounted for in the simulations. This could be done by simply changing the numerical domain to cover the area surrounding one nucleation site (which would vary for each contact angle).

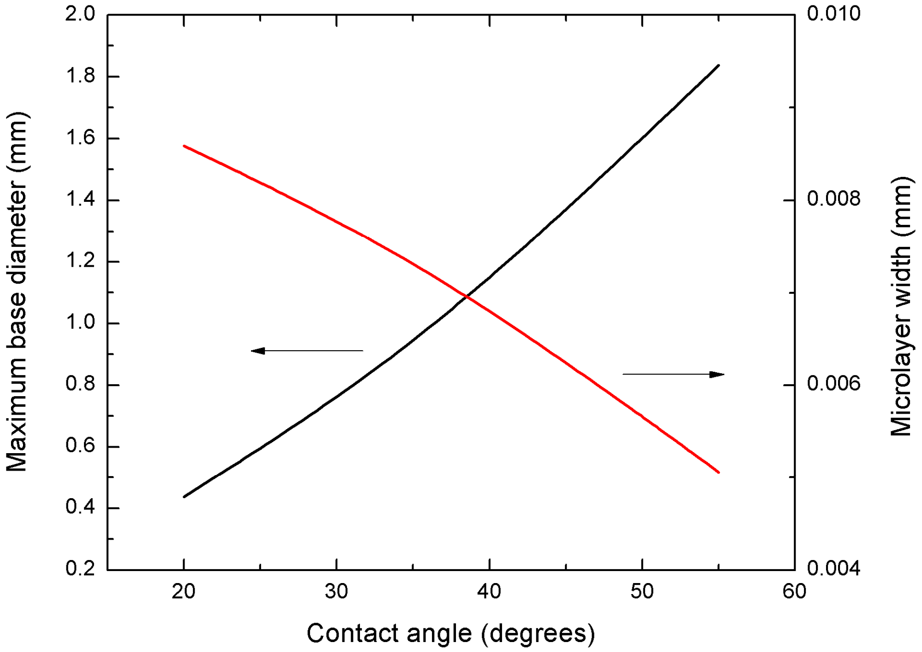

(a)

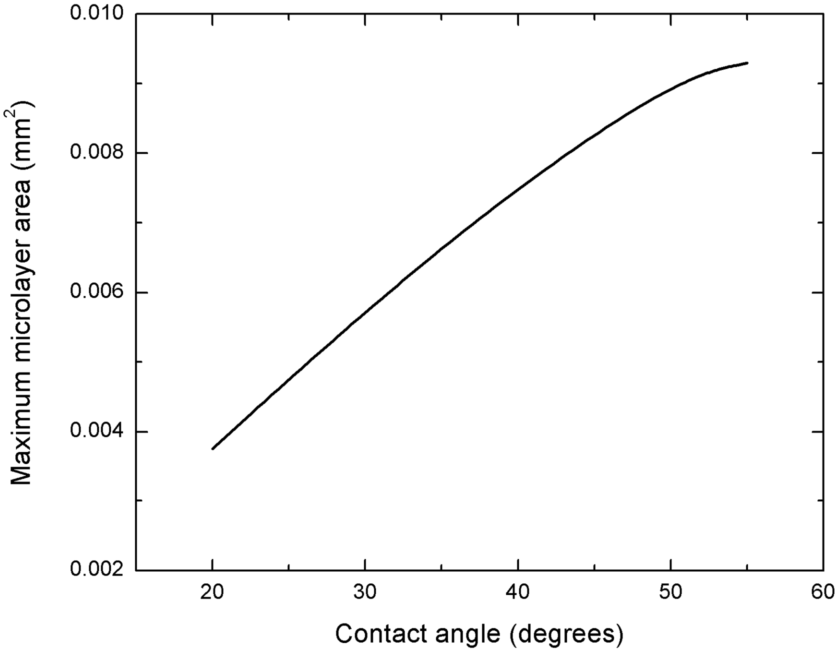

(b)

Figure 5.30 Dependence on contact angle of (a) bubble's maximum base diameter and microlayer width, and (b) maximum microlayer area. Water boiling on 0.5 *mm* thick stainless steel surface at one atmosphere pressure with $q_{w,in}$ = 1.1 *W/cm*^{2} and ΔT_{nuc} = 6 ^{o}*C*.

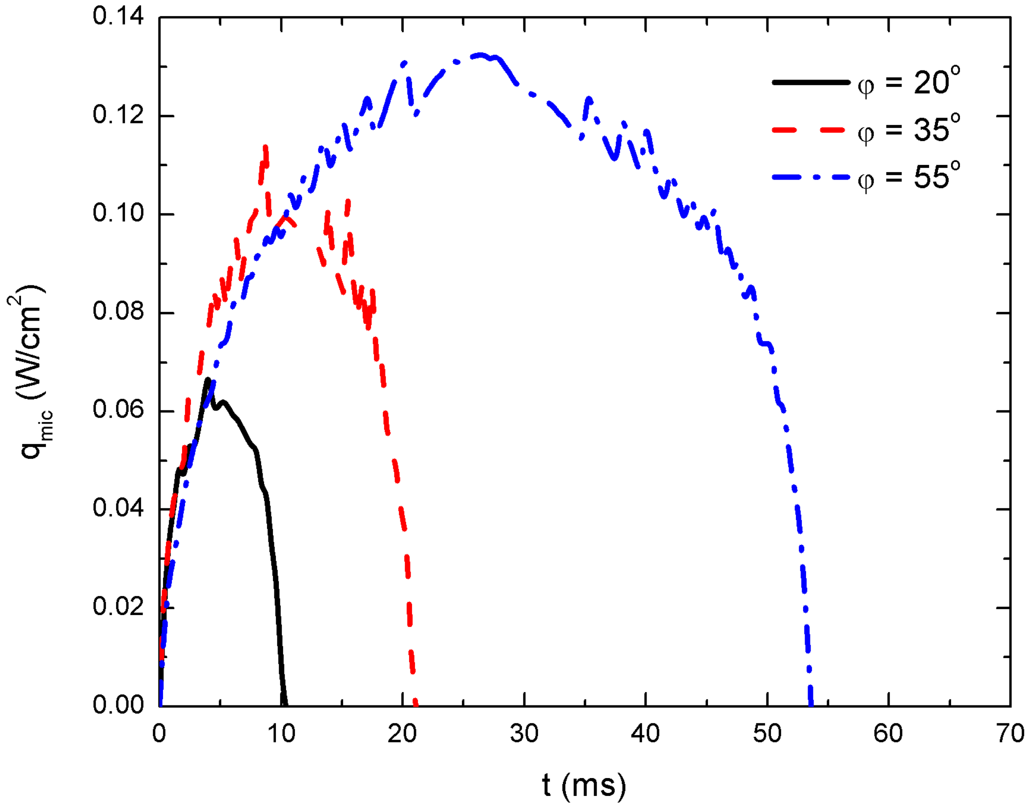

Figure 5.31 **Transient microlayer heat transfer rate for water boiling on a 0.5 *mm* thick stainless steel surface for various contact angles with $q_{w,in}$ = 1.1 W/cm^2 and ΔT_{nuc} = 6 °C.**

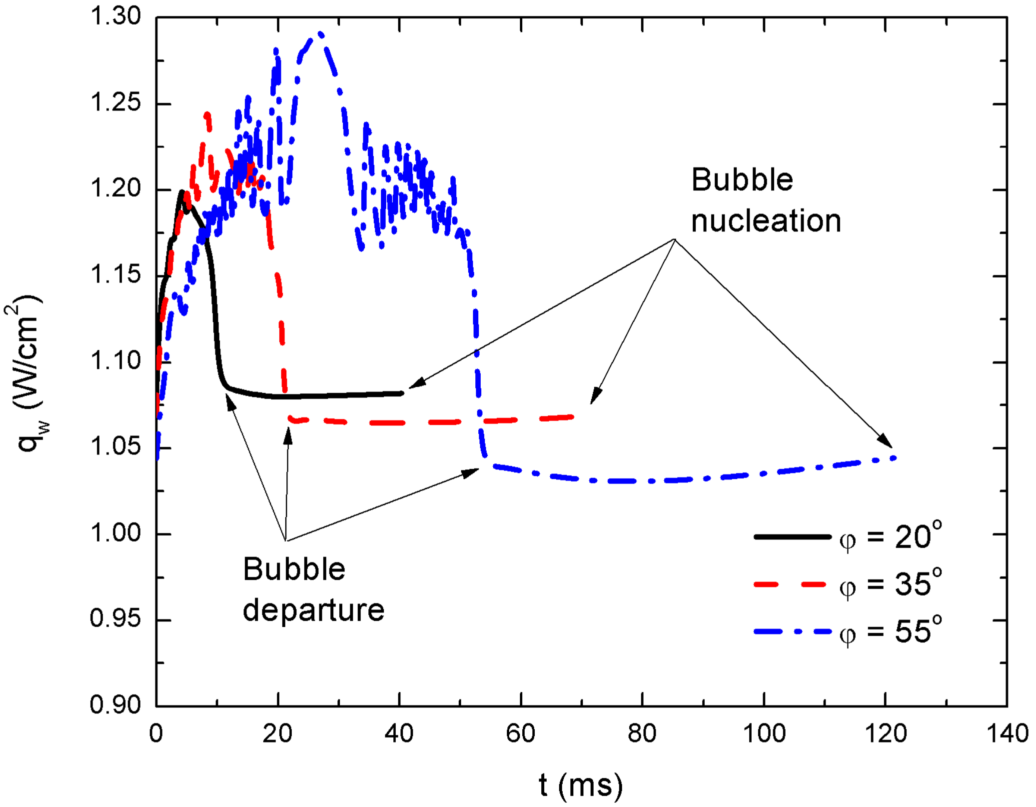

Figure 5.32 Transient wall heat flux for water boiling on a 0.5 *mm* thick stainless steel surface for various contact angles with $q_{w,in} = 1.1\ W/cm^2$ and $\Delta T_{nuc} = 6\ ^\circ C$.

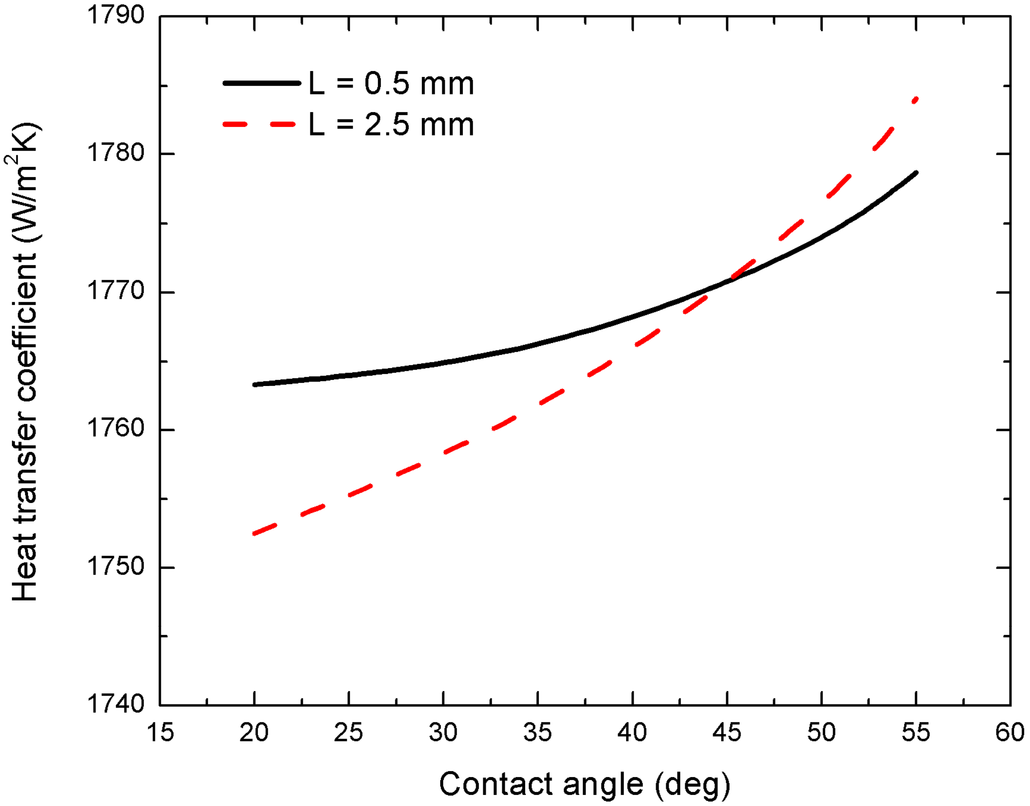

Figure 5.33 The effect of contact angle on heat transfer coefficient for water boiling on a 0.5 *mm* thick stainless steel surface with $q_{w,in}$ = 1.1 W/cm^2 and ΔT_{nuc} = 6 ^oC. Heat transfer coefficient averaged over the area of a circular heater with R = 4 *mm*.

5.3 Single bubble dynamics in microgravity and in the presence of noncondensable gas

In the following sections comparisons will be made between the predictions of the numerical simulations performed and experimental results obtained by Dhir et al. (2012) in the Nucleate Pool Boiling Experiment (NPBX) performed aboard the International Space Station (ISS). Bubble dynamics under two different pressures, liquid subcoolings, and dissolved mass fraction of gas were considered. The dissolved gas was assumed to be air with a molar mass of 29 g/mol while the fluid used was Perfluoro-n-Hexane (PFH) weighing 338 g/mol. A summary of the experimental conditions for the two cases studied is given in Table 5.

As shown previously in section 4.1, conduction was still the primary mechanism of heat transfer at the time of nucleation during the NPBX experiments. Therefore, the thickness of the thermal layer above the heater was initially approximated assuming pure conduction in the liquid as follows

$$\delta_t = \sqrt{\pi \alpha t_n} \tag{63}$$

where t_n denotes the time interval between initiation of heating and bubble nucleation for each case. Based on experiments this time interval was of the order of a few hundred seconds, such that the initial thermal layer thickness ranged from 3 to 8 millimeters at the time of bubble nucleation.

	Case 1	Case 2
Gas content, $C_{g,l}$	6×10^{-5}	2×10^{-5}
Pressure (kPa)	60 - 80	145 - 160
Change in T_{sat} (°C)	4.9 – 6.4	0.9 – 1.0
Duration (s)	200	800
ΔT_w (°C)	2 - 13	(-1) - 3
ΔT_{sub} (°C)	0 - 2	7 - 9
Bubble size history	Growth	Growth, shrinkage

Table 5 Experimental conditions for each case studied.

5.3.1 Case 1: low pressure, high mass fraction of noncondensables

The mass fraction of gas dissolved in the liquid (C_g) for the first case was 6×10^{-5}. The experimental conditions for the first case are shown in Figure 5.34(a) and Figure 5.34(b). Note that Figure 5.34 shows data after bubble nucleation occurred (i.e. nucleation occurred at $t = 0\ s$). During bubble growth the system pressure varied from 60 to 80 kPa. The pressure varied because the bellows could not keep up with the rapid increase in vapor volume caused by the growing bubble. The saturation temperature of the PFH was calculated based on the dissolved gas as follows

$$\begin{aligned} x_g &= \frac{C_g/M_g}{C_g/M_g + C_{PFH}/M_{PFH}} \\ p_{PFH} &= p_{total} - \frac{x_g}{H_g} \\ T_{sat,PFH} &= T\left(p_{PFH}\right) \end{aligned} \tag{64}$$

where $C_{PFH} = 1 - C_g$. The saturation temperature conditions correspondingly varied from 36 to 46 °C. As mentioned previously, the power supplied to strain gage heaters was controlled to maintain a constant surface temperature. However, because of system pressure change, T_{sat} changed, which resulted in ΔT_w and ΔT_{sub} changing with time. Figure 5.34(b) shows the variations of ΔT_w and ΔT_{sub} for the first 200 seconds of bubble growth.

The growth history for the bubble is shown in Figure 5.35 where the equivalent bubble diameter (D_{eq}) is plotted as a function of time. D_{eq} is defined as the diameter of a perfect sphere having the same volume as the actual bubble. The experimental data show that equivalent bubble diameter, D_{eq}, grew to approximately 50 mm in 80 seconds, at which point ΔT_w was still decreasing and ΔT_{sub} increasing. This was due to the increase in system pressure and corresponding increase in T_{sat}. The bubble size became nearly constant (bubble growth rate almost zero) because the condensation rate from bubble interface increased with increasing ΔT_{sub} while the evaporation rate at the base and bubble interface decreased with decrease in ΔT_{w}. As the bubble stopped growing, the continued expansion of the bellows finally caused the pressure in the test chamber to drop. Additionally, the wall temperature was increased at around 100 seconds. As a result of the increase in ΔT_w and decrease in ΔT_{sub}, the bubble began to grow again. The solid line in Figure 5.35 shows the simulated results assuming equilibrium conditions inside the bubble. In this case the species conservation equation is not solved because, at equilibrium, the mass fraction of gas inside the bubble is assumed to remain constant and is found using Eqs. (51) through (55). This case provides an upper limit for the gas content inside the bubble. Accordingly, this approach also provides an upper limit for the reduction in saturation temperature. The agreement between the simulation and the experimental results during the first 150 seconds is remarkable. After 150 seconds, however, the simulation results begin to diverge from the experimental data. The dashed line shows the results from simulations performed when the species conservation equation is solved in the vapor space. This approach provides a more complete and realistic picture of the physical processes taking place, including the addition of noncondensable gas into the bubble and distribution of gas inside the bubble as it grows. Although the dashed line does not show as close an agreement with the experimental data as the solid line, it does a noticeably better job of capturing the growth rate and oscillations observed in the final 100 seconds of bubble growth.

Bubble shape and size obtained from the simulations are compared with the experimental results in Figure 5.36. At 20 seconds the shape and size of the simulated bubble matches the experimentally obtained bubble size well. However, at 100 seconds the experimental bubble equivalent diameter is under-predicted by approximately 8 mm (about 20%). At 180 seconds, many small extraneous bubbles can be seen nucleating and merging with the primary bubble. These mergers resulted in the wavy interface seen in the figure and an estimated increase in the size of the experimentally measured bubble of approximately 5%. The simulation under predicted the size of the bubble by 13% at 180 seconds.

The average wall heat flux obtained from the experiment is also shown in Figure 5.36 alongside the local wall heat transfer rate predicted from the simulation. The experimental wall heat flux is given as an average over the entire surface except where the heaters were turned off. Since the heaters were controlled to maintain a constant surface temperature, they were automatically turned off where the surface was dry due to the low heat transfer coefficients present in those locations. The peaks shown from the simulations coincide with the location of pinning of the liquid-vapor interface on the wall and are due to the contribution of microlayer evaporation. The peak values vary because the microlayer heat transfer rates vary linearly with the wall superheats. The oscillation in local wall heat transfer rate immediately adjacent to the liquid-vapor interface is caused by the temperature field that develops around the bubble as will be shown later (Figure 5.38(b)). The wall heat transfer rate predicted is in good agreement with the experimental values for at 20 and 100 seconds. At 180 seconds the average wall heat transfer rate prediction is almost 30% lower than the experimental data. However, there is substantial uncertainty in the experimental wall heat transfer rates due to the transient nature of the heat losses through the insulation under the heater. Figure 5(a) shows the temperatures measured at different depths inside the insulation for the first 200 seconds of bubble growth. The time-dependence of the temperatures indicates that the heat losses are not constant in time. Since all the power was supplied at the bottom of the aluminum plate (depth of 0 *mm*), the best approximation of the instantaneous heat losses is given by the temperature gradient between the bottom of the aluminum plate and the first temperature measured inside the insulation (at a depth of 5.3 *mm*). However, the conductivity is not known precisely at such a shallow depth due to the fact that the wires (thermistor wires and strain gage wires for power) are densely packed within the first few millimeters of the insulation. This introduces another uncertainty in the calculation of the heat losses. The instantaneous heat losses based on the temperature gradient between the bottom of the aluminum plate and the first temperature measurement inside the insulation are given in Figure 5.37(b). At any given time, the average wall heat flux was calculated based on the total power supplied at that time minus the instantaneous heat losses.

Figure 5.38(a) shows streamlines outside the bubble. At 20 seconds the bubble was still in its initial phase of fast growth. Correspondingly, the streamlines in the liquid shown in Figure 5.38(a,i) spread radially outwards from the bubble and then up towards the top of the domain where the opening to the bellows is located. At 100 seconds the growth rate has slowed down significantly and the streamlines in Figure 5.38(a,ii) show that recirculation patterns start to form around the bubble. Finally, at 180 seconds, the bubble is growing faster again and the flow can be seen in Figure 5.38(a,iii) to be pushed out and up while the recirculation patterns become smaller. Figure 5(b) shows lines of constant temperature (isotherms) in the liquid surrounding the bubble. The interval between each isotherm represents a constant temperature difference of approximately 0.6 ^{o}C. The plume atop the bubble is a consequence of the energy added to the liquid through condensation. The size of the plume can be seen to increase with time, starting out barely noticeable in Figure 5.38(b,i) at 20 seconds. After 100 seconds, Figure 5.38(b,ii) shows an appreciable plume signifying the presence of more substantial condensation. The plume growth is slowed down between 100 and 180 seconds because the condensation rate decreased. The recirculation patterns described previously lead to the thickening of the thermal layer around the sides of the bubble seen in Figure 5.38(b,ii) and (b,iii). In Figure 5.38(c) lines of constant mass fraction of noncondensable gas are shown inside the bubble with intervals between lines of 2×10^{-4}. Figure 5.38(c,i) through (c,iii) show that the gas mass fraction is smallest near the base of the bubble and increases towards the top where condensation takes place and the noncondensable gas accumulates. It should also be noted that, due to the fact that the molecular weight of the gas is an order of magnitude smaller than that of the vapor, this configuration of gas accumulation is aided by the very limited buoyancy. Finally, streamlines are shown inside the bubble in Figure 5.38(d). Figure 5.38(d,i) through (d,iii) show that the flow pattern inside the bubble—predominantly from the base of the bubble to the top—remains similar throughout the 180 seconds. This flow pattern further reinforces the configuration set up by condensation in which the noncondensable gas accumulates at the top of the bubble. Some recirculation patterns are also seen to develop inside the bubble at 180 seconds.

Figure 5.39 shows evaporation/condensation rate, mass fraction of gas, interface temperature, and surface tension along the interface of the bubble. Each of the interface conditions is plotted as a function of the angle along the interface, starting at 0° (horizontal wall) and ending at 90° (vertical axis of symmetry). It was previously noted that the noncondensable gas tends to accumulate at those locations where the vapor condenses and leaves behind the noncondensable gas. This behavior is detailed in Figure 5.39. It can be seen in Figure 5.39(a,i) that the mass fraction of noncondensable gas begins to rise steeply at approximately a 25° angle along the interface, coinciding with the angle at which condensation begins (evaporation becomes negative). At 100 seconds, Figure 5.39(a,ii) shows that at approximately 65° the condensation rate begins to drop due to the presence of the plume atop the bubble. Correspondingly, the mass fraction of gas at the interface also drops as the rate of vapor removal decreases. Similar trends can be observed at 180 seconds in Figure 5.39(a,iii). Figure 5.39(b,i) to (b,iii) show that interface temperature has a negative correlation with the mass fraction of gas. This is due to the fact that an increase in mass fraction of gas results in a decrease of partial pressure of vapor. Therefore, the accumulation of the noncondensable gas inside the bubble leads to decreasing interface temperature which effectively reduces the effect of subcooling. It should be noted that the scales in Figure 5.39(b,i) through (b,iii) are not the same due to the fact that interface temperature and surface tension also depend on system pressure which varies significantly throughout the duration of the experiment (65 kPa at 20 seconds and 80 kPa at 100 seconds).

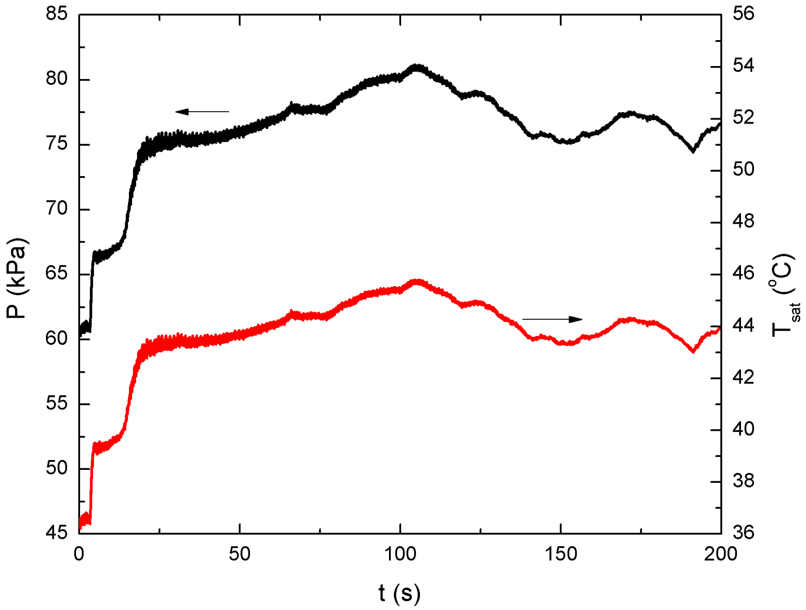

(a)

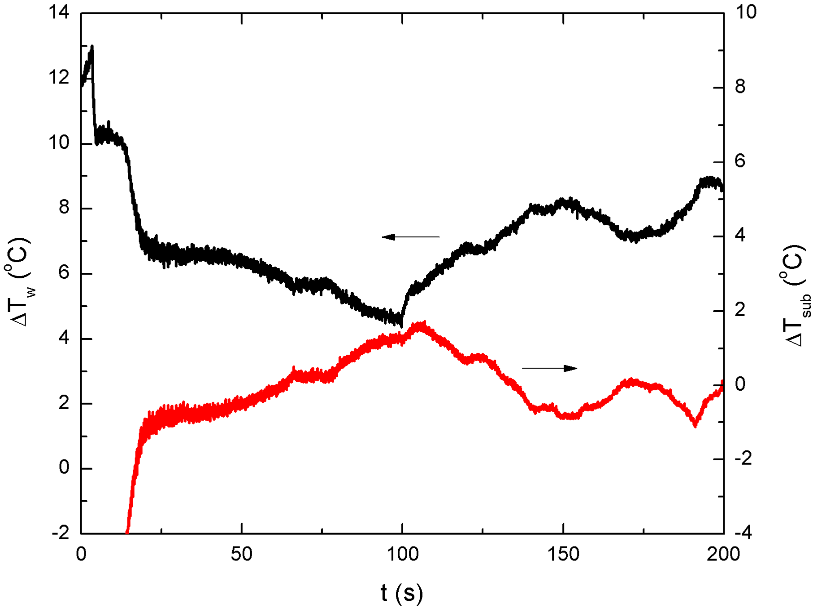

(b)

Figure 5.34 Time-dependent experimental conditions (a) system pressure and saturation temperature and (b) wall superheat and liquid subcooling.

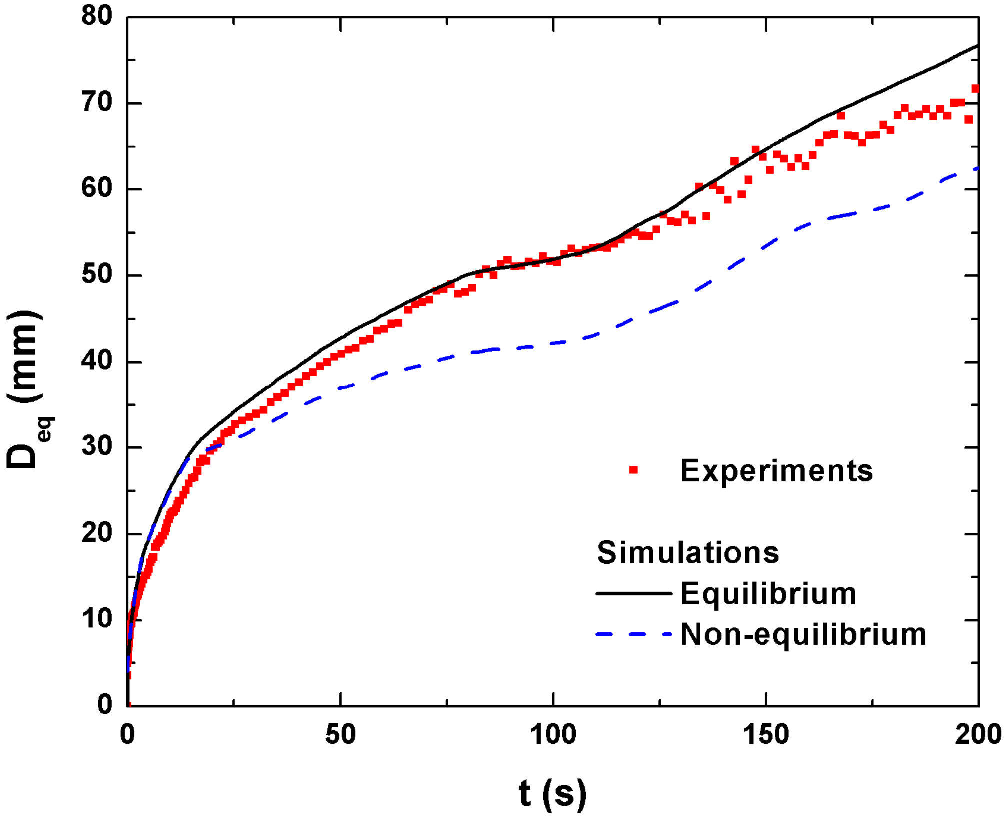

Figure 5.35 Growth history comparison between experiments and simulations.

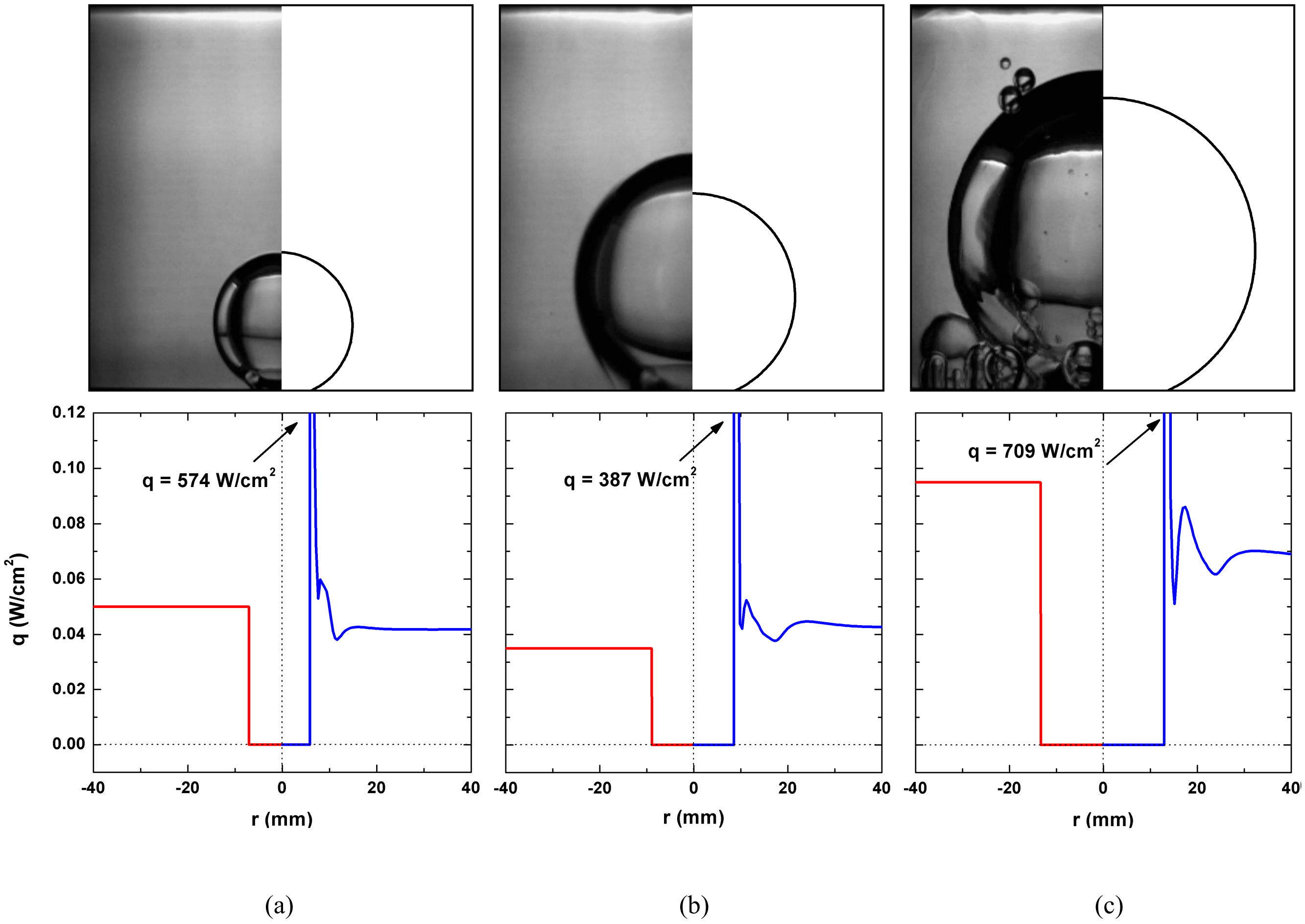

(a) (b) (c)

Figure 5.36 Bubble shape and wall heat transfer rate comparison between simulations and experiments at (a) 20 seconds, (b) 100 seconds, and (c) 180 seconds.

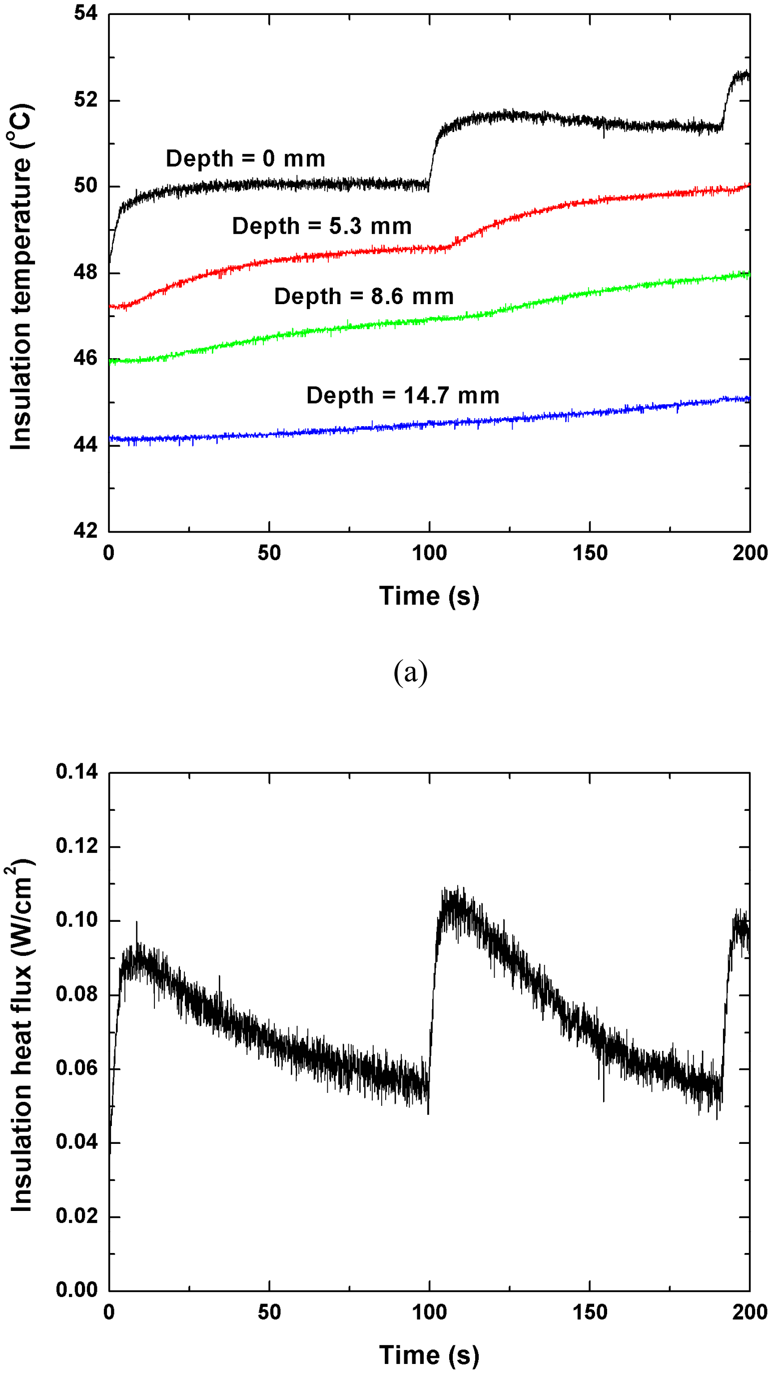

(a)

(b)

Figure 5.37 (a) temperatures measured inside the insulation and (b) calculated instantaneous heat flux through the first 5.3 *mm* of the insulation.

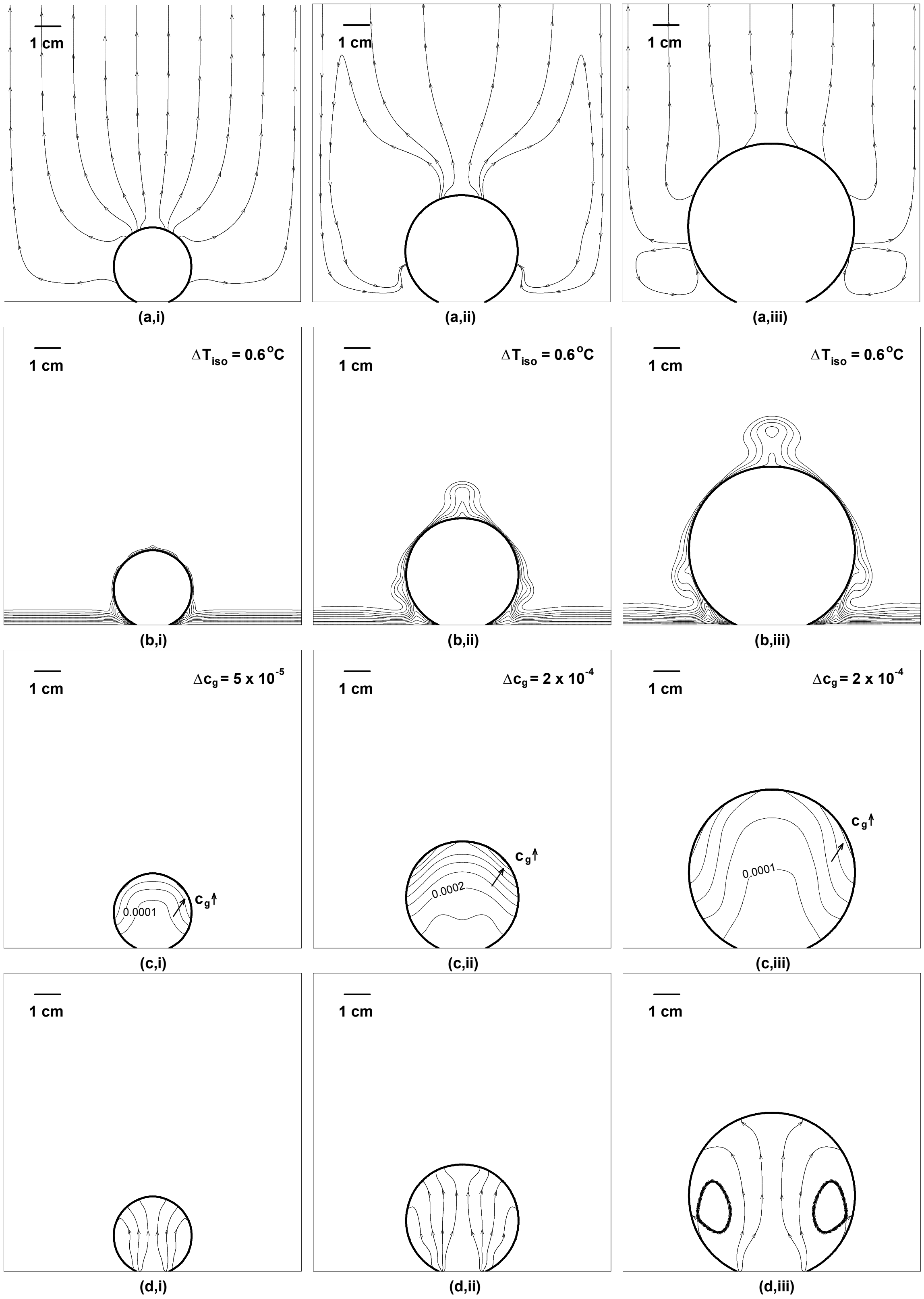

Figure 5.38 Contour plots showing: (a) streamlines in the liquid, (b) isotherms, (c) lines of constant mass fraction, and (d) streamlines inside the bubble at (i) 20 seconds, (ii) 100 seconds, and (iii) 180 seconds.

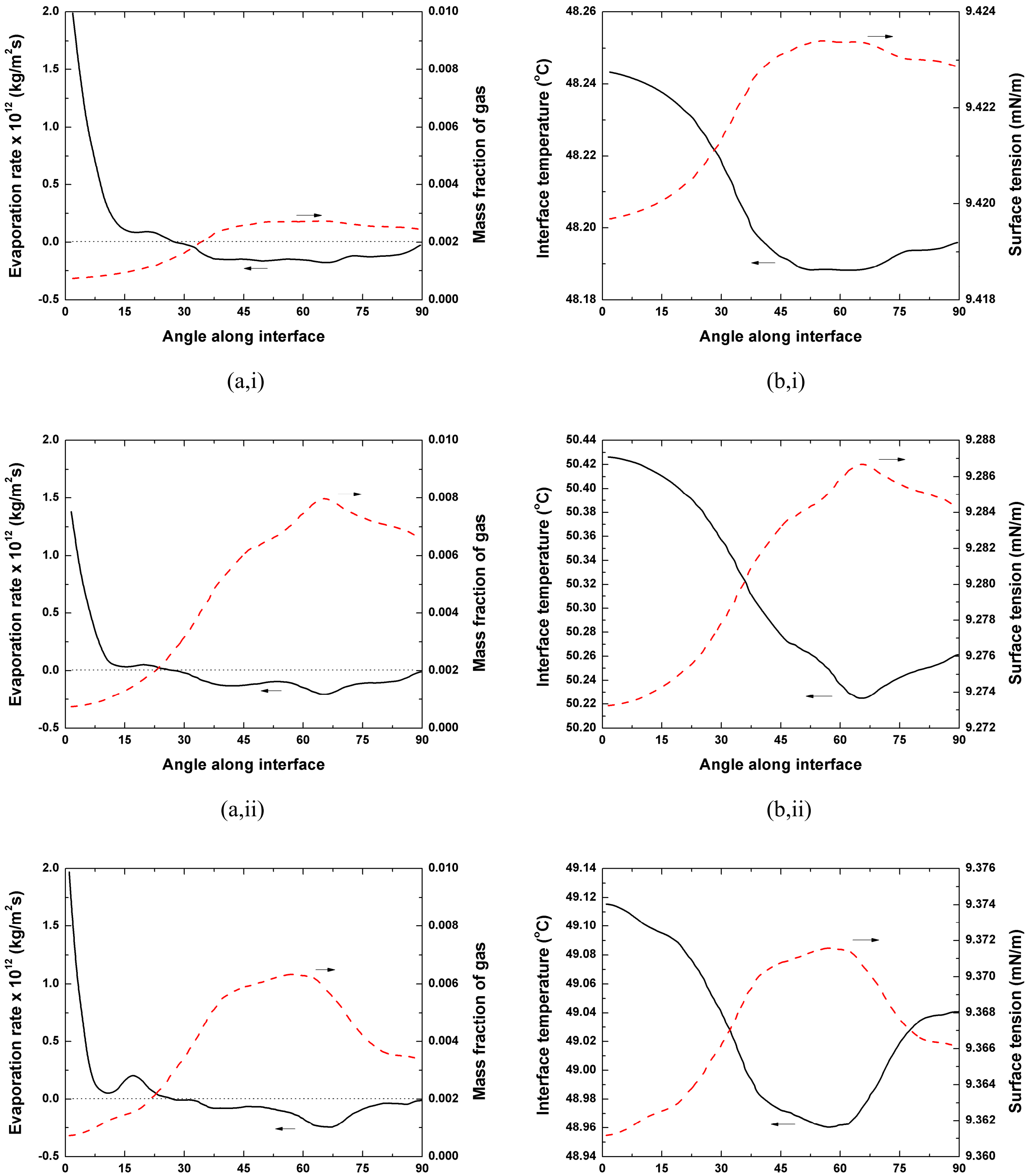

(a,i) (b,i)

(a,ii) (b,ii)

(a,iii) (b,iii)

Figure 5.39 Evaporation rate, mass fraction of gas, interface temperature, and surface tension along interface of bubble at (i) 20 seconds, (ii) 100 seconds, and (iii) 200 seconds. Angle along the interface is measured from the horizontal boiling surface up to the vertical axis of symmetry.

5.3.2 Marangoni convection

The accumulation of noncondensable gas, decrease of partial pressure of vapor, and corresponding increase in interface temperature are responsible for the variations in surface tension observed in Figure 5.39(b). Since the surface tension has a negative correlation with the local vapor pressure (or saturation temperature), it is seen to peak where vapor content is lowest (noncondensable gas content is highest). This variation in surface tension along the bubble interface can induce thermocapillary flow around the bubble. However, careful examination of the surface tension force per unit length shows that the variation is extremely small (<0.2%). As such, thermocapillary flow only has a second order effect on the flow field around the bubble at any given moment. In order to elucidate the accumulated effect of capillary flow for a relevant period of time, the same exact simulation was repeated assuming constant surface tension. Figure 5.40 shows isotherms on the left and lines of constant mass fraction on the right at 180 seconds for (a) the case with variable surface tension and (b) the case with constant surface tension. The difference between the two is barely noticeable, thus corroborating the claim that capillary flow has a weak effect on the flow and temperature fields even after significant accumulation of gas.

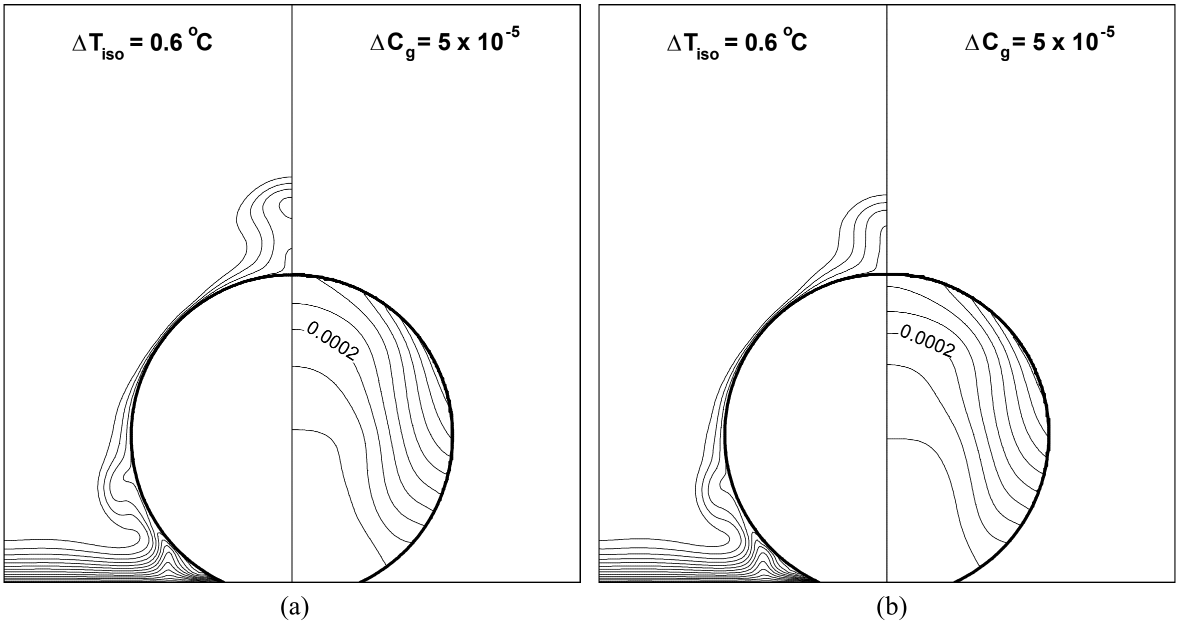

(a) (b)

Figure 5.40 Lines of constant mass fraction on the left and isotherms on the right after 200 seconds of growth for (a) variable surface tension and (b) constant surface tension.

5.3.3 Case 2: high pressure, low mass fraction of noncondensables

In this case, the system pressure is higher by a factor of two while the mass fraction of the dissolved gas in the liquid is lower at 2×10^{-5} (factor of three). Figure 5.41(a) shows that the pressure varied considerably during the experiment (800 seconds). The initial spike in pressure was caused by the inability of the bellows to keep up with the rapidly increasing vapor volume of the bubble. At approximately 80 seconds the pressure began to drop as the continued expansion of the bellows caught up with the growth of the bubble. Eventually, the pressure dropped below the specified point and the bellows had to shrink in order to increase the system pressure back to its original set point. The varying system pressure was the cause for most of the wall superheat and liquid subcooling variations shown in Figure 5.41(b). After the initial 80 seconds, the wall superheat gradually increased and the liquid subcooling gradually decreased for the first 400 seconds, at which point the wall temperature was intentionally decreased in steps. As a result, the wall superheat slowly decreased while the liquid subcooling increased.

The wall superheat and liquid subcooling variation over the course of 800 seconds is reflected in the bubble growth history seen in Figure 5.42. The experimental data show that the bubble grew quickly at first and then the growth slowed down and it subsequently started to shrink as the condensation rate became larger than the evaporation rate. The solid line represents the results from the simulation assuming equilibrium conditions exist inside the bubble as explained previously. The dashed line shows the results obtained when the species conservation equation was solved in the vapor region. The equilibrium assumption provided a simulated bubble growth history that better matched the experimental observations for the first 200 seconds. However, it is seen that the simulation assuming equilibrium conditions inside the bubble started to over predict the experimental results at longer times. Conversely, the simulation which accounted for species conservation had a slightly slower growth rate initially but eventually yielded a better prediction of the overall growth history observed in the experiment. Specifically, the species-conserving simulation did a noticeably better job of predicting the stoppage in bubble growth for 20-70 seconds and capturing the shrinking observed during the last few hundred seconds.

As seen in Figure 5.42, for a period of about 50 seconds during the experiment, the bubble equivalent diameter remained approximately constant at 13 mm. This is due to the fact that, as a bubble grows in subcooled liquid, an increasing portion of the bubble interface comes in contact with the subcooled liquid. This increases the condensation rate which decreases the bubble growth rate. Wu and Dhir (2011) have shown that, for certain subcooled nucleate pool boiling conditions, a bubble may grow until the point when condensation balances evaporation. Under these conditions the bubble remains attached to the wall indefinitely. A similar situation is encountered in the present case, where evaporation is balanced by condensation during the early stages of bubble growth (< 70 seconds). Beyond 70 seconds, due to changing system pressure that leads to increased wall superheat and reduced liquid subcooling, evaporation exceeds condensation and the bubble begins to grow again. Figure 5.43(a) shows, on an expanded scale, the first 100 seconds of experimental and simulated bubble growth histories. The flat portion in which the bubble equivalent diameter remains constant can be seen clearly in both the experimental data and the results obtained from the species-conserving simulation. Figure 5.43(b) shows the net interface heat transfer rate (evaporation minus condensation heat flux) for the first 100 seconds of the simulation. It can be seen that in the simulation the evaporation and condensation rates balance each other out resulting in zero interface heat transfer rate for over 30 seconds.

Figure 5.44(a) through (c) show comparisons between experimentally observed and numerically calculated bubble shapes and sizes at 100, 300 and 700 seconds, respectively. At 100 and 300 seconds the bubble size is under-predicted by the simulation such that the calculated equivalent diameter is about 10-20% smaller than that obtained in the experiment. At 700 seconds the simulation over predicts the experimentally observed bubble size. Wall heat transfer rates are also shown in Figure 5.44 with the experimental results on the left side of each frame and the numerical results on the right. The large spikes in heat flux in the simulations coincide with the location of the pinning of the vapor-liquid interface on the wall. The peak values represent the contribution of the microlayer and vary linearly with the wall superheat. The dips in wall heat flux immediately adjacent to the peaks are a result of a local thickening of the thermal layer around the base of the bubble (as shown later in Figure 5.46(b)). At all three times the wall heat transfer rates predicted are lower than those obtained in the experiments. At 100 seconds the under prediction is larger than 50%. However, as mentioned earlier, there is significant uncertainty in the estimation of heat losses in the experiments due to their transient nature. The time dependence of the temperatures measured inside the insulating epoxy (under the heaters) is shown in Figure 5.45(a) for the 800 second duration of the experiment. At any given instant, the best approximation of the heat losses can be obtained from the temperature gradient between the bottom of the aluminum plate and the first thermocouple located inside the insulation at a depth of 5.3 *mm*. The wall heat fluxes reported earlier (Figure 5.44) are calculated based on the total power supplied to the strain gage heaters minus the approximate instantaneous losses as shown in Figure 5.45(b).

Figure 5.46(a) and (b) show streamlines and isotherms in the liquid while Figure 5.46(c) and (d) show lines of constant mass fraction and streamlines inside the bubble at various times. The streamlines in Figure 5.46(a,i) show that, during the initial phase of fast bubble growth, the liquid flowed radially out from the bubble and up towards the opening at the top of the boiling chamber. At 300 seconds Figure 5.46(a,ii) shows the formation of recirculation patterns as the growth rate of the bubble has slowed down significantly. The main contrasting feature for this case can be observed in Figure 5.46(a,iii) when the bubble is actually shrinking (at 700 seconds). As the bubble shrinks, the liquid begins to flow back from the bellows into the boiling chamber through the opening placed vertically above the center of the cavity. This results in a large portion of the liquid actually flowing down. The only streamlines still showing upwards flow are above the bubble and are a result of the presence of the large plume of hot liquid (as shown later in Figure 5.46(b,iii)). The presence of the plume of hot liquid above the bubble in Figure 5.46(b,i) shows that condensation is already appreciable at 100 seconds. Figure 5.46(b,ii) confirms the continued contribution of condensation as the plume grows appreciably after 200 more seconds have passed. In addition to the enlarging plume, the thickening of the thermal layer around the sides of the bubble is evident in Figure 5.46(b,iii). This thickening is a consequence the recirculation patterns that develop around the base of the bubble as described previously. The significantly lower dissolved gas content in this case, combined with the longer duration and higher subcooling, lead to higher condensation rates. As a result, the rising plume that develops on top of the bubble is significantly larger than it was for Case 1. The resulting thickness of the thermal layer around the bubble determines the local condensation rate which in turn determines the rate of accumulation of noncondensable gas inside the bubble. It can be observed in Figure 5.46(c,i) through (c,iii) that the mass fraction of noncondensable gas is low near the base of the bubble where evaporation occurs and increases towards the top of the bubble where condensation is dominant. The streamlines inside the bubble plotted in Figure 5.46(d,i) through (d,iii) show a pattern of flow predominantly from the base of the bubble to the top, reinforcing the distribution of noncondensable gas established by the local evaporation/condensation rate.

Figure 5.47(a) shows the hot liquid plume atop the bubble for Case 2 at 700 seconds while Figure 5.47(b) and (c) are interferograms showing similar hot plumes as obtained experimentally by Abe and Iwasaki (1999) and Straub (2002). The experiments of Abe and Iwasaki were performed in a drop tower with the gravity level reported to be between 10^{-4} and 10^{-5} ge. The binary fluid mixture used was CFC112/CFC12. The fluid used in Straub's experiments was R123 and they were performed in the Space Shuttle with a reported gravity level between 10^{-3} and 10^{-5} ge. Therefore, significant differences exist between the fluids' thermophysical properties and between the conditions encountered in the experiments and those used in the numerical simulation. Nevertheless, the isotherm patterns observed in the figures are remarkably similar. In addition to the plume growing above each of the bubbles, the interferograms show the thickening of the thermal layer along the sides of the bubbles. The region where the thermal layer is thinnest is at an angle of approximately 65^{o}; this is similar to the value predicted by the simulations. The size of the plume is significantly larger in the case of Straub but the author explained that the interferogram reported was not from a single bubble but from a sequence of bubbles that continuously grew and collapsed in cycles.

Figure 5.48 shows evaporation rate, mass fraction of gas, interface temperature, and surface tension as functions of the angle along the interface. The solid lines in Figure 5.48(a) show the evaporation/condensation rate. At 100, 300, and 700 seconds, respectively, Figure 5.48(a,i) through (a,iii) show a decreasing overall rate of evaporation. However, the overall condensation rate remains nearly constant. As a consequence, the mass fraction of gas (represented by the dashed lines in the same figures) is seen to increase with time as more noncondensable gas accumulates inside the bubble. The peak mass fraction of gas at 100 seconds is only slightly over 0.003 (Figure 5.48(a,i)), increasing to 0.005 by 300 seconds (Figure 5.48(a,ii)) and to almost 0.011 by 700 seconds (Figure 5.48(a,iii)). The solid lines in Figure 5.48(b,i) through (b,iii) show that the interface temperature decreases as a function of angle along the interface until reaching a minimum which coincides with the maximum mass fraction of gas. Conversely, the surface tension (represented by the dashed lines in Figure 5.48(b)) can be seen to increase as a function of angle along the interface and peak at the same angle as the mass fraction of gas. However, the effect of the variation of surface tension along the interface on the flow field is of second order.

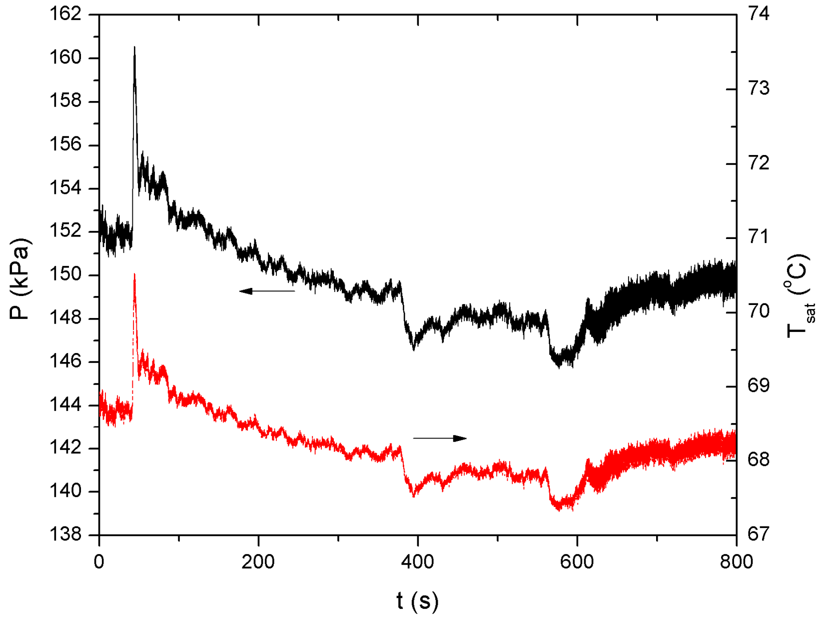

(a)

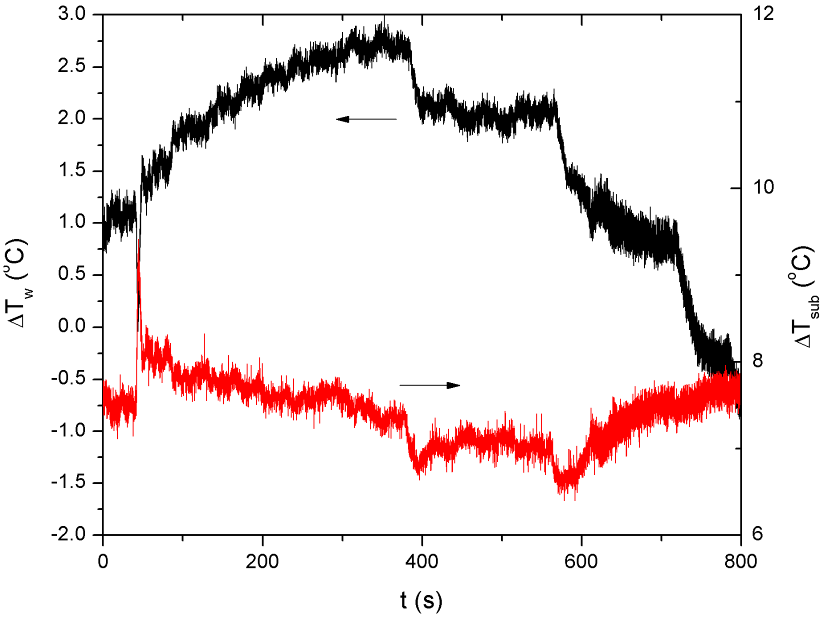

(b)

Figure 5.41 Time-dependent experimental conditions including system pressure, saturation temperature, wall superheat, and liquid subcooling.

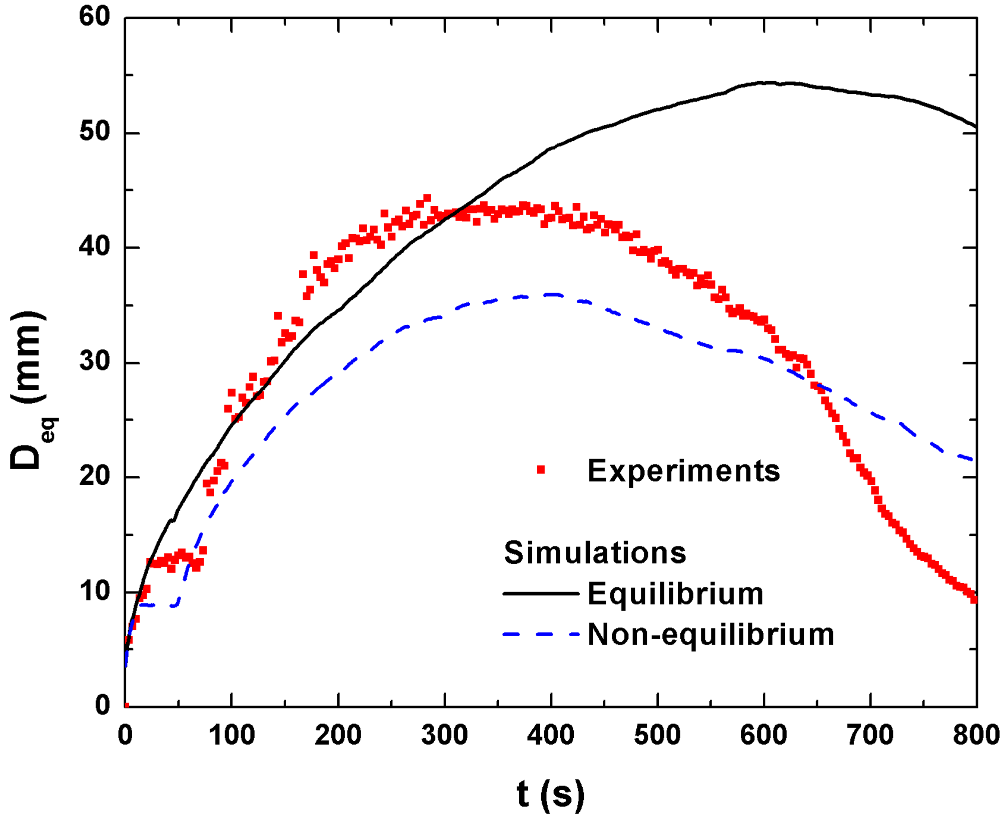

Figure 5.42 Growth history comparison between experiments and simulations, including the cases of equilibrium conditions assumption and the full solution of the species conservation equation.

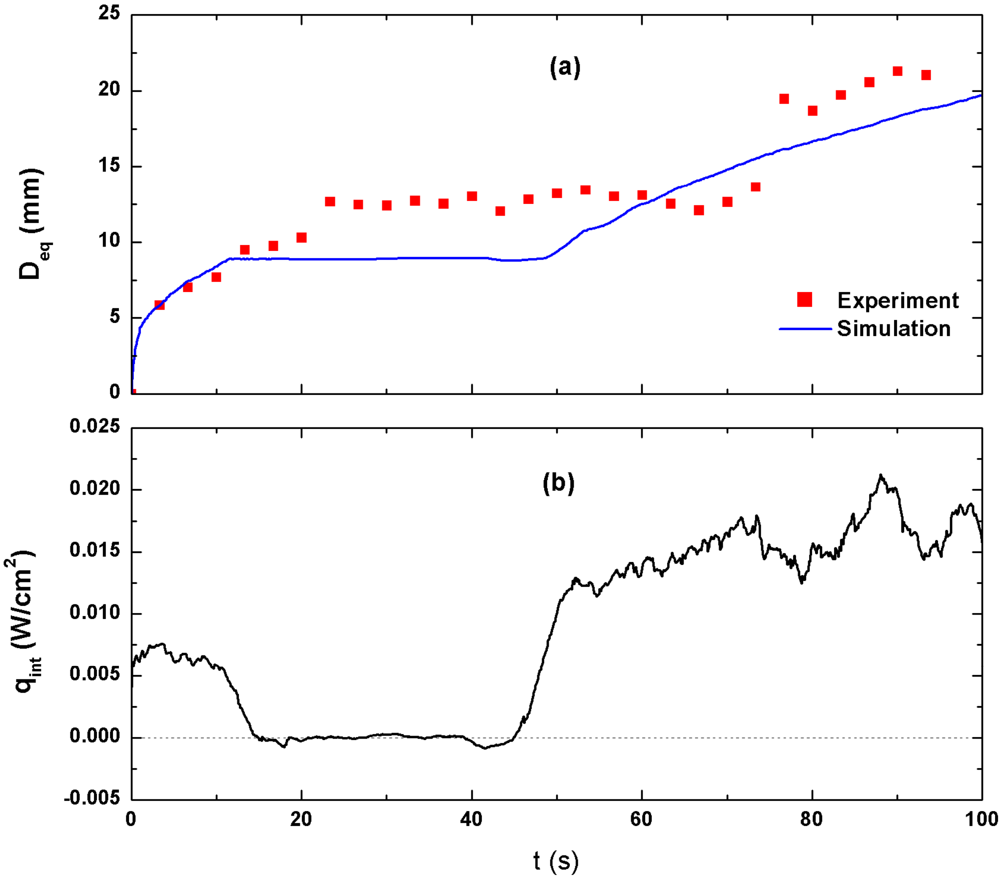

Figure 5.43 (a) Bubble growth history and (b) net interface heat flux as a function of time for the second case.

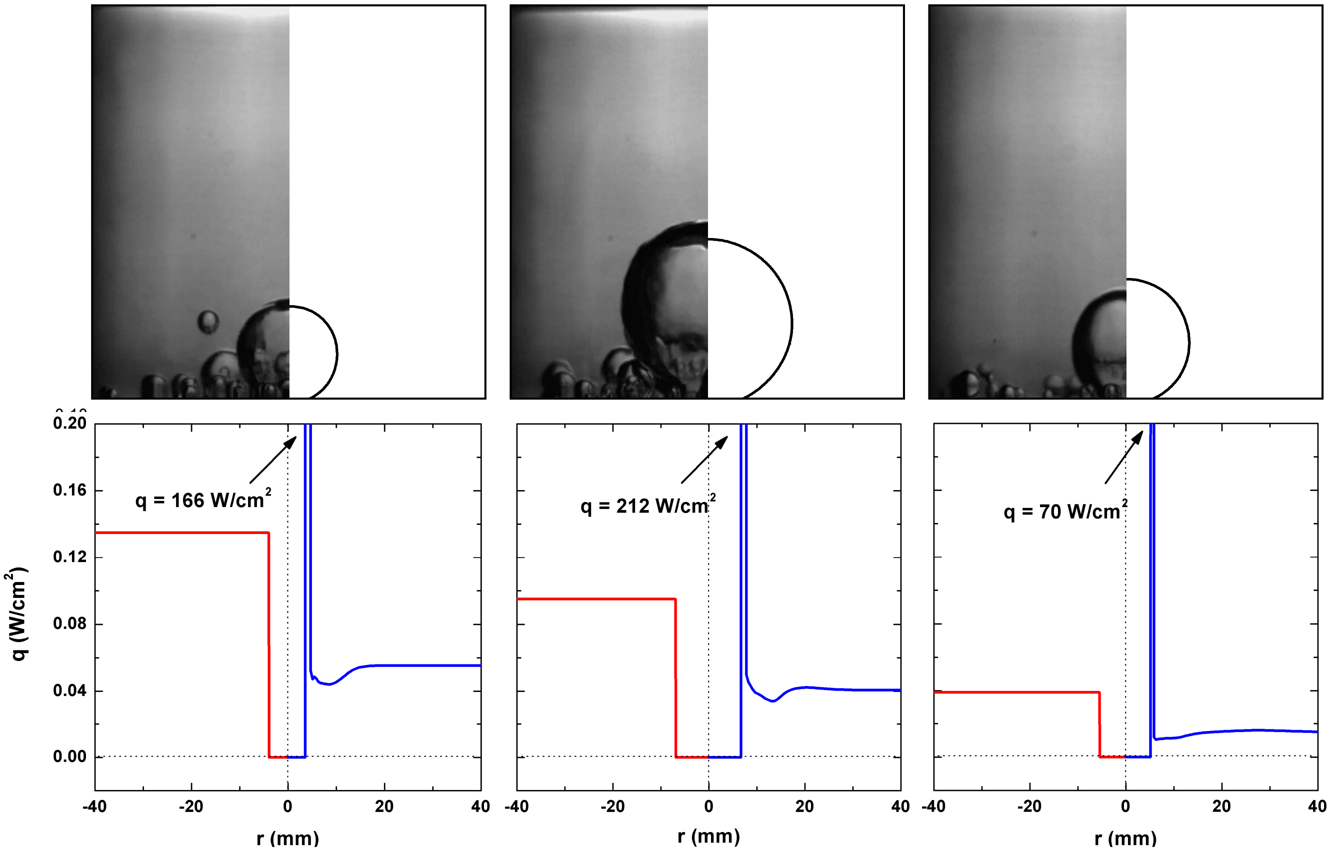

(a) (b) (c)

Figure 5.44 Bubble shape comparison between simulations and experiments at (a) 100 seconds, (b) 300 seconds, and (c) 700 seconds.

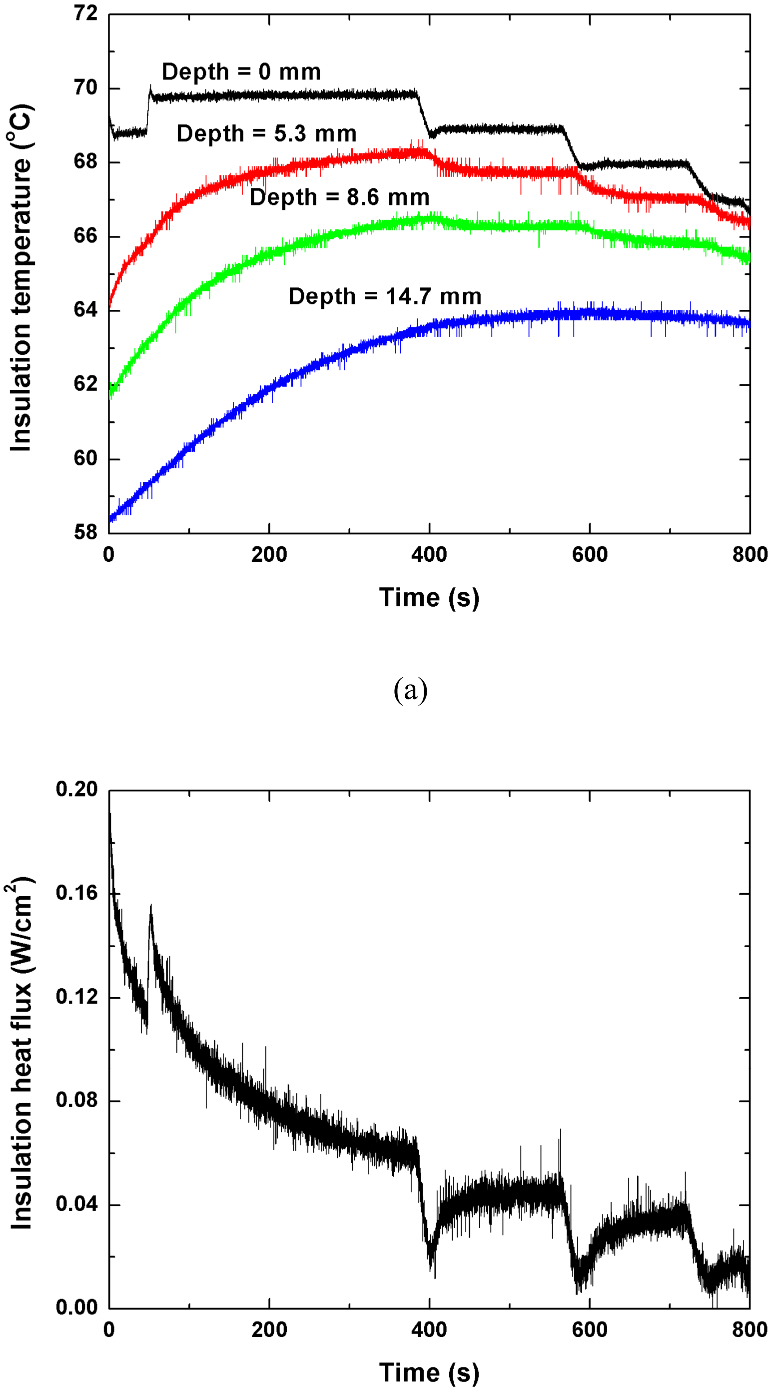

(a)

(b)

Figure 5.45 (a) temperatures measured inside the insulation and (b) calculated instantaneous heat flux through the first 5.3 *mm* of the insulation.

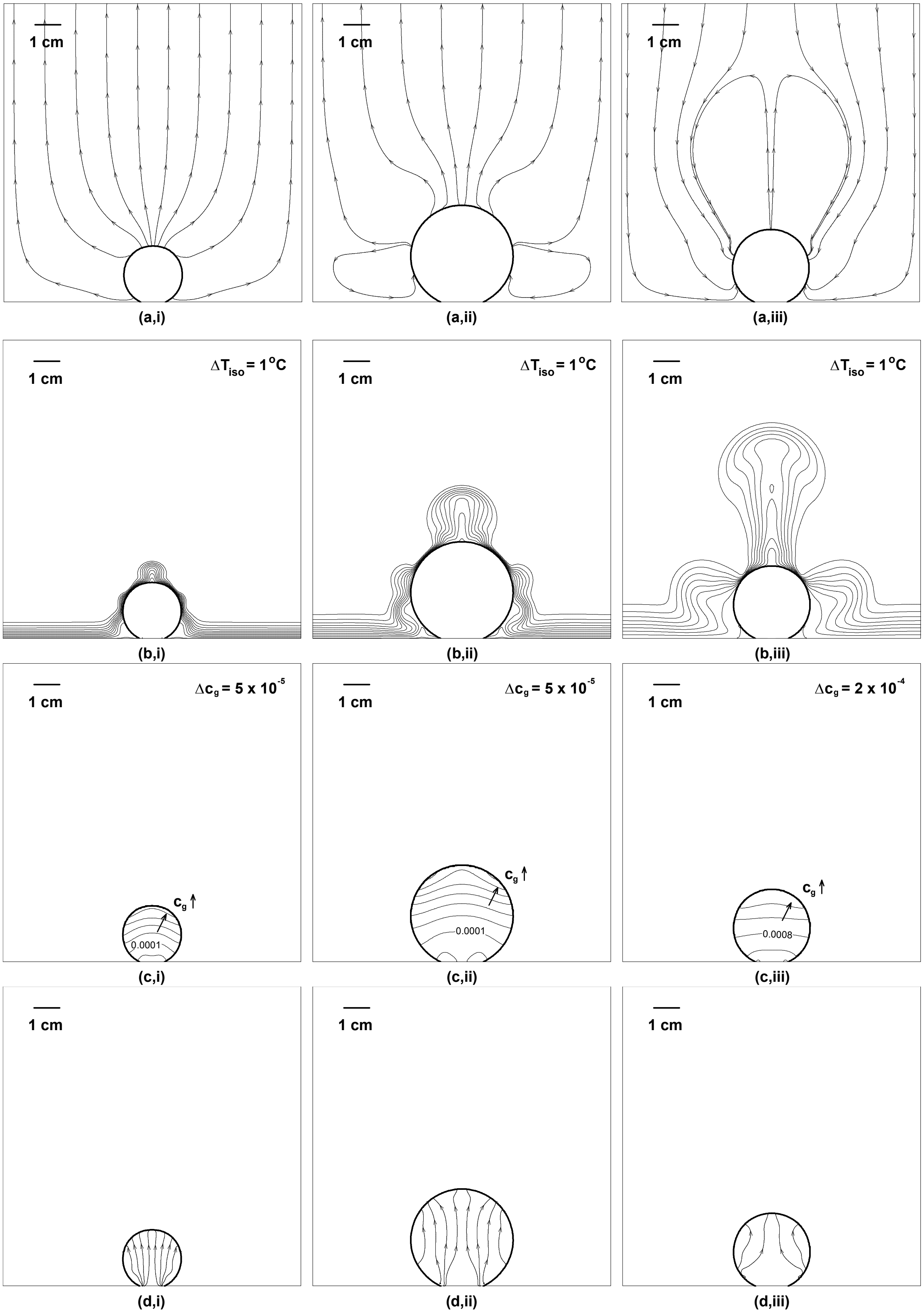

Figure 5.46 Contour plots showing: (a) streamlines in the liquid, (b) isotherms, (c) lines of constant mass fraction, and (d) streamlines inside the bubble at (i) 100 seconds, (ii) 300 seconds, and (iii) 700 seconds.

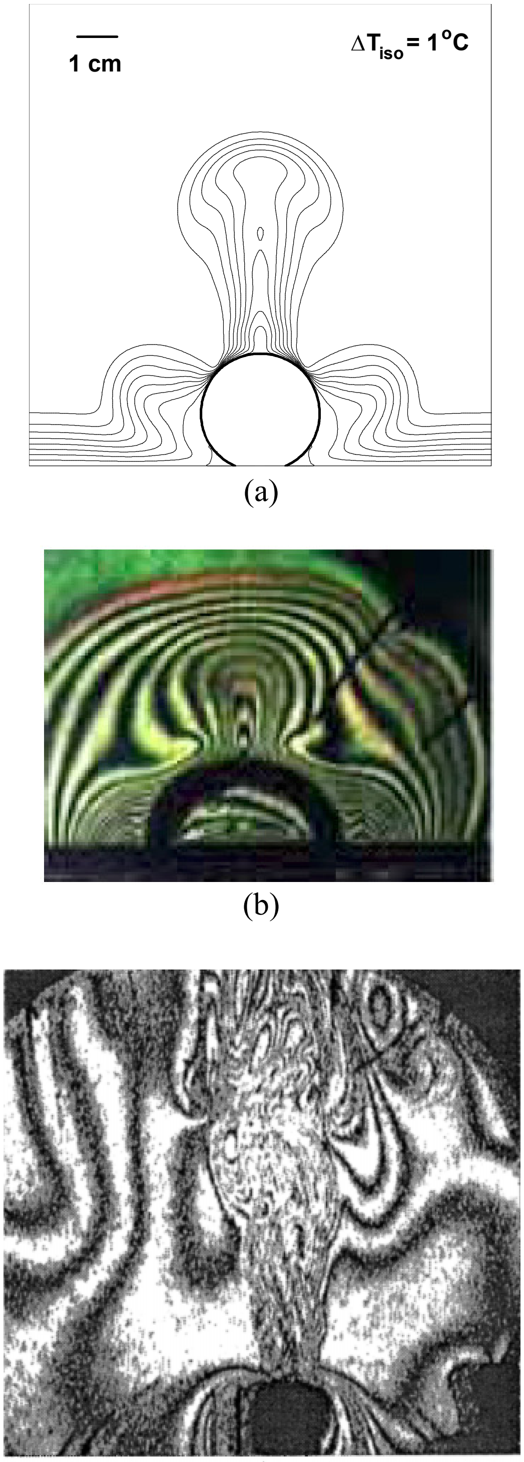

(a)

(b)

(c)

Figure 5.47 Comparison between the temperature field obtained by (a) the numerical calculations performed in the present study at $g/g_e \sim 10^{-7}$, (b) interferogram results reported by Abe and Iwasaki at $g/g_e \sim 10^{-5}$ [17], and (c) interferogram reported by Straub at $g/g_e \sim 10^{-4}$ [18].

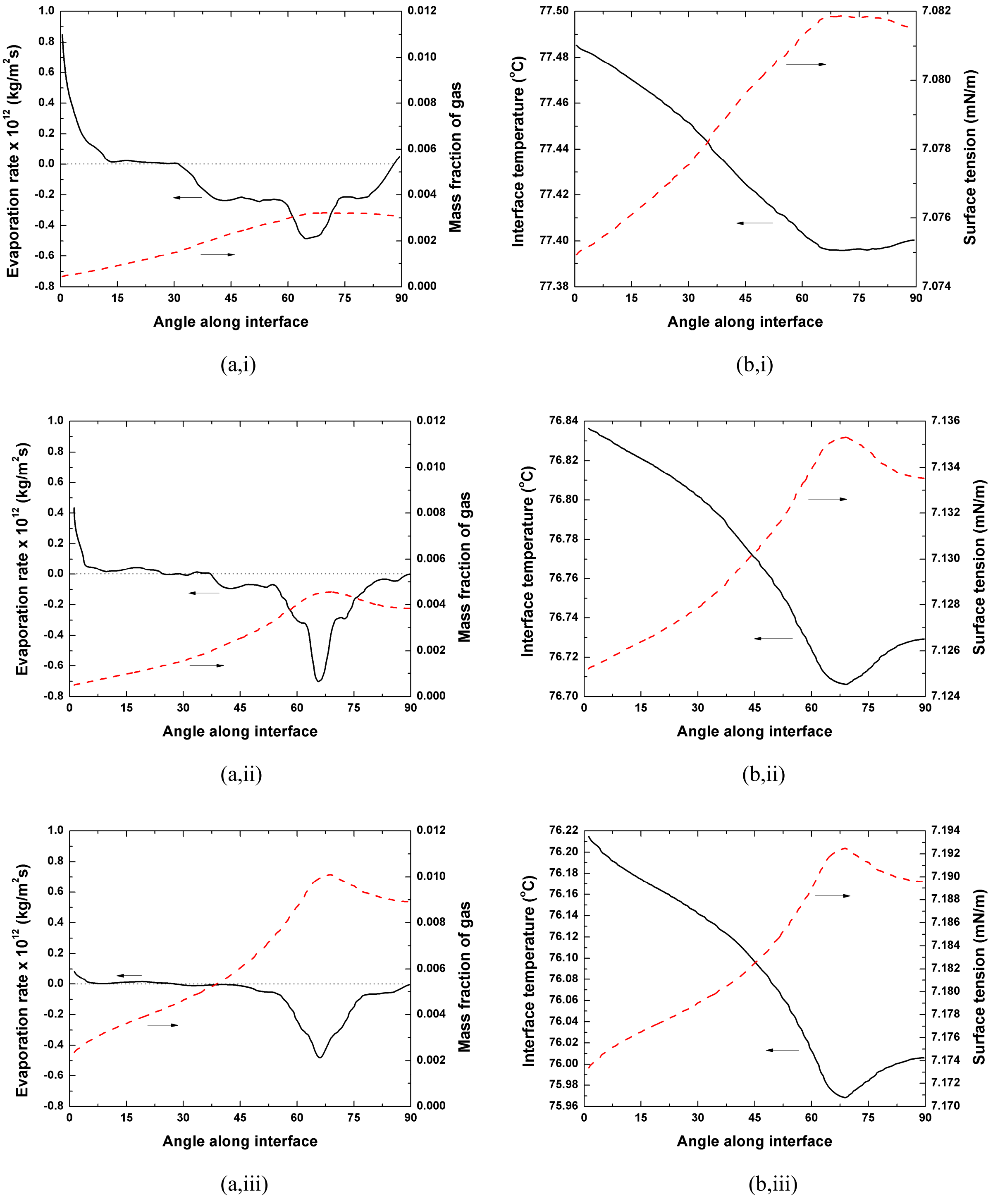

(a,i) (b,i)

(a,ii) (b,ii)

(a,iii) (b,iii)

Figure 5.48 Evaporation rate, mass fraction of gas, interface temperature, and surface tension along interface of bubble at (i) 100 seconds, (ii) 300 seconds, and (iii) 700 seconds. Angle along the interface is measured from the horizontal boiling surface up to the vertical axis of symmetry.

5.3.4 Numerical predictions and experimental results for bubble departure diameter and growth period

The numerically predicted bubble departure diameter as a function of gravity level is given in Figure 5.49 for water and PFH. Data from the experiments of Qiu et al. (2000) and Straub (2001) are also included. In the experiments of Qiu et al. in the parabolic flights, the bubbles lifted off from the surface. However, in Straub's experiments, the bubble did not lift off so the diameter shown in Figure 5.49 is the largest diameter of the bubble while still attached to the heater surface. In the present experiments, single bubbles never departed the surface. The points are nevertheless included in the figure and it can be seen that the largest bubble equivalent diameters obtained in the experiments are well below the numerically predicted bubble departure diameters. According to the numerical prediction, at the gravity level encountered on the ISS the boiling chamber would have to be significantly larger to allow a bubble to acquire a large enough diameter to depart the surface.

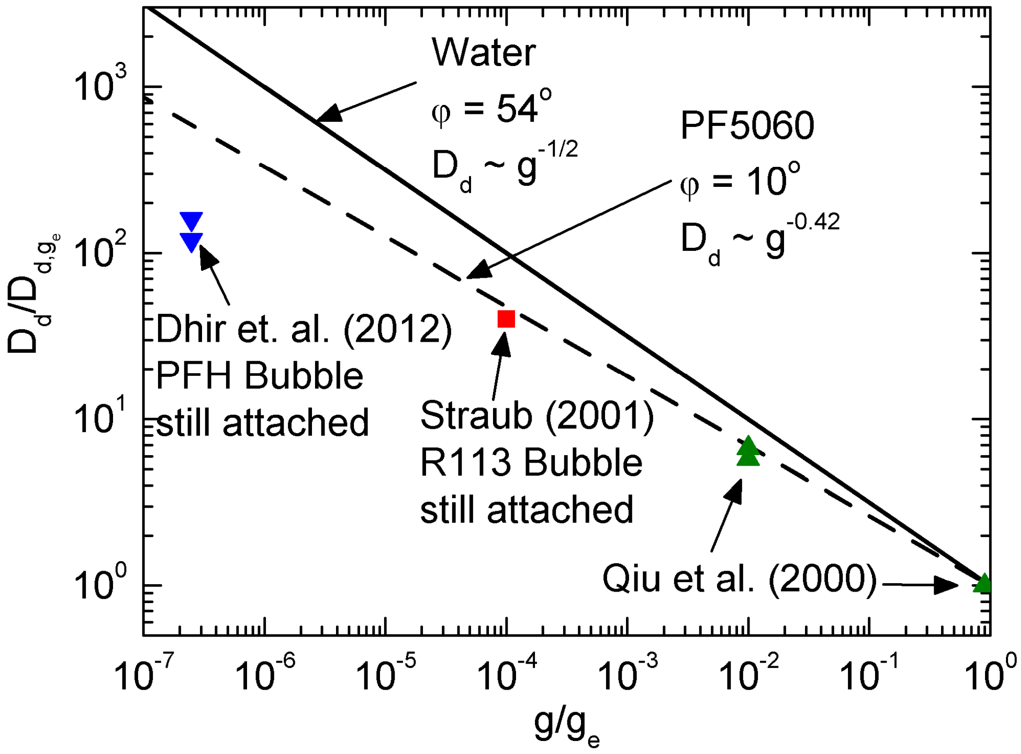

Figure 5.49 Numerically predicted and experimentally obtained bubble departure diameters for varying gravity level.

5.4 Nucleate pool boiling in microgravity conditions

In addition to single bubble experiments, Dhir et al. (2012) also performed nucleate pool boiling experiments. As described in section 1.7, it has been noted by several authors in the literature that the vapor removal process in nucleate pool boiling under microgravity conditions is entirely different than at earth normal gravity. There is also a general consensus among all investigators of boiling under reduced gravity conditions that the critical heat flux decreases with decreasing gravity level. However, there remains some debate about whether a reduced gravity environment results in improvement or deterioration of boiling heat transfer rates during partial nucleate boiling. In the following sections comparisons will be made between the predictions from numerical simulations and experimental results obtained by Dhir et al. (2012). The two main areas of interest for the comparisons are the vapor removal patterns and the heat transfer rates.

In order to keep the simulations as simple as possible for the first attempt at predicting vapor removal patterns, the problem of conjugate conduction in the solid substrate is not included. Instead, the heater surface is assumed to remain at a constant and uniform temperature throughout. As a consequence, the number of active cavity sites has to be specified as well as the waiting period between successive bubble nucleations. For these purposes, empirical correlations are used. The active site density is estimated for each superheat simulated using the correlation provided by Basu et al. (2002),

$$\begin{aligned} N_a &= 3.4\times10^{-1}\left[1-\cos\left(\varphi_s\right)\right]\Delta T_w^{2.0} & \Delta T_{w,ONB} < \Delta T_w < 15^\circ \\ N_a &= 3.4\times10^{-5}\left[1-\cos\left(\varphi_s\right)\right]\Delta T_w^{5.3} & \Delta T_w \geq 15^\circ \end{aligned} \tag{65}$$

where N_a is in units of cavities per square centimeter. For the range of wall superheat simulated, the active site density ranges from approximately 0.5 to 2 cavities per square centimeter. Similarly, the waiting time is estimated based on the superheat using the following correlation also developed by Basu et al. (2002),

$$t_w = 139.1\left(\Delta T_w^{-4.1}\right) \tag{66}$$

The resulting waiting time varied from under 100 milliseconds to almost 2 seconds at the lowest wall superheat.

5.4.1 Vapor removal pattern during nucleate pool boiling in microgravity conditions

Under earth normal gravity conditions, the vapor volume generated at the base of the bubbles attached to the heater surface is removed when the bubbles detach as a consequence of the buoyancy force. Once they become large enough the buoyancy force overcomes the surface tension and the bubbles float up and away from the heater surface. Under highly reduced gravity, however, the buoyancy force is greatly reduced and vapor removal from the heater surface does not occur by the same buoyancy-driven detachment mechanism. Instead, under highly reduced gravity conditions, bubble mergers become the primary mechanism by which the vapor is removed from the heater surface. Depending on the size and spacing of laterally merging bubbles, the inertia of the merger may cause the bubbles to detach from the surface. However, the detached vapor mass does not float away due to the reduced buoyancy force experienced and drag of the surrounding liquid. Subsequently, the new bubbles that nucleate on the heated surface grow until they merge with the vapor mass still located directly above the center of the heater. This merger causes the new bubbles to detach from the surface. The resulting vapor removal pattern is of a large vapor mass floating near the heated surface while bubbles nucleate, grow until they come into contact with the large vapor mass, merge with it, and thus detach from the surface. Alternatively, the large vapor bubble may remain attached to the heater surface throughout. In such a case, bubbles continue to nucleate and grow around the large vapor mass and eventually merge with it. The vapor removal pattern is similar except for the slight change in the position of the large vapor bubble. Both cases are entirely different from the dynamics present under earth normal gravity. Figure 5.50 shows an example of experiments performed by Lee et al. (1997) of the resulting distribution of bubbles during nucleate pool boiling under earth normal gravity and microgravity conditions.

Figure 5.51 shows a simulation of the development of nucleate pool boiling in microgravity. In this case the fluid is PFH, gravity level is $10^{-5}\ g_e$, and a total of 25 cavities are active over a 32 *mm* diameter circular heater. Additionally, the bulk liquid is saturated, the wall superheat is 7 ^{o}C, and the waiting time between bubble nucleations for any given site is 50 *ms* as obtained from Eq. (66). The times at each frames are 0.2, 2, 5, and 20 seconds, respectively. The first frame shows that, as the bubbles initially coalesce together from all sides, the bulk of the vapor mass moves towards the center of the heater. The initial fast growth of the large vapor mass results in an overall motion in which the fluid is pushed radially outwards as seen in Figure 5.51(a). After 2 seconds have elapsed, the vapor mass at the center of the heater is significantly larger. Due to the cavity distribution on the circular heater, small bubbles continue to nucleate all around the large bubble. As the top of the large bubble continues to move up and push the liquid up, some liquid must flow down due to mass conservation. This results in the flow reversing direction around the sides of the large bubble. As a result, the reversal of the flow causes the small bubbles to move radially in towards the large bubble and eventually merge with it. After this flow pattern is established it remains similar throughout the simulation as can be seen at 5 and 20 seconds. Additionally, it can be seen throughout that the multiple mergers causes oscillations in the large bubble's shape. Due to the lack of subcooling in this case, the bubble would continue to grow indefinitely and eventually cover the entire heater surface or take up the entire computational domain. In the cases in which the bulk liquid is subcooled, a steady state may eventually be reached in which vapor production at the base of the bubble is balanced out by the condensation occurring around the top of the large bubble. Nevertheless, the initial transient pattern remains similar for subcooled boiling.

Figure 5.52 shows comparisons between experimental and numerical bubble shapes and vapor removal patterns for a system pressure of approximately 140 *kPa* and subcooling of 12 ^{o}C and for two different wall superheats. The estimated mass fraction of gas dissolved in the liquid in this case was 2 x 10^{-5} (or 240 *ppm* concentration). At the given system pressure, the change in saturation temperature due to the presence of dissolved gas is only approximately 1 ^{o}C. This change in saturation temperature is included in the simulations by assuming the vapor and liquid phases are in equilibrium. Therefore, the gas content in the vapor phase can be obtained by using Henry's law and the species conservation equation is not solved. The superheat in Figure 5.52(a) is 3.4 ^{o}C and the diameter of the bubble takes up approximately 60-70% of the width of the viewing window (80 mm). At this wall superheat the total number of active nucleation sites present on the 89.5 *mm* diameter circular heater is 45 and the waiting period is 920 *ms*. The large bubble is still in contact with the heater surface while numerous bubbles nucleate around its base and coalesce with it after a growth period that lasts a few seconds. In Figure 5.52(b) the superheat is higher at 5.2 ^{o}C and the bubble diameter takes up almost the entire viewing window. For this wall superheat the total number of active nucleation sites present on the same surface is

105 and the waiting period is 160 *ms*. In this case the large bubble is floating atop the heated surface and bubbles nucleate all over the heater. After a few seconds of growth and lateral mergers, the newly nucleated bubbles become large enough to come into contact with the large bubble and coalesce with it. In this way, whether the large bubble remains attached or floats atop the heater surface, it acts as a vapor reservoir for the nucleating bubbles. Without such a mechanism for bubble removal, growing bubbles could be expected to remain attached and eventually cover the entire heater surface with vapor, leading to film boiling prematurely.

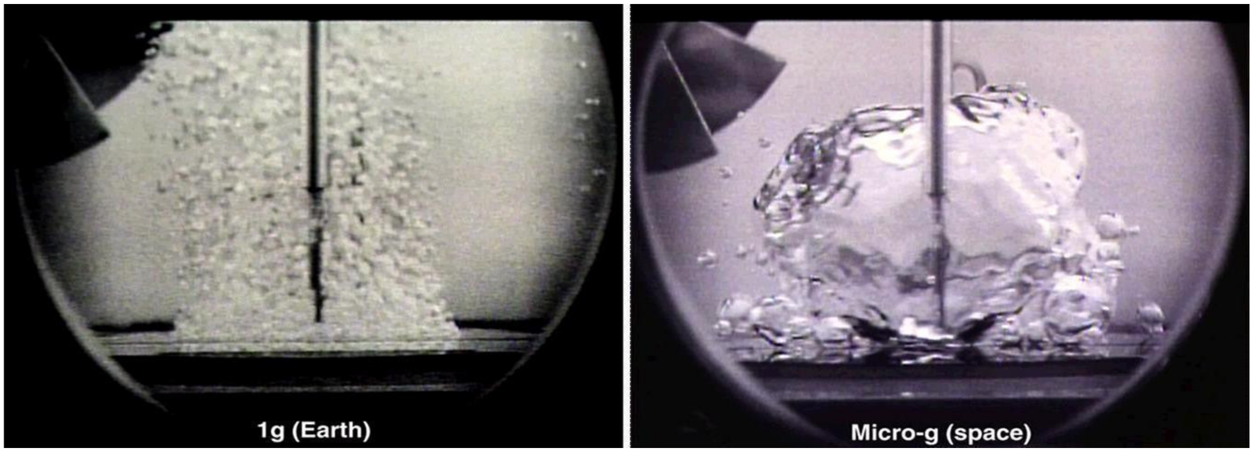

Figure 5.50 Vapor removal pattern during nucleate pool boiling under earth normal gravity conditions and microgravity by Lee et al. (1997).

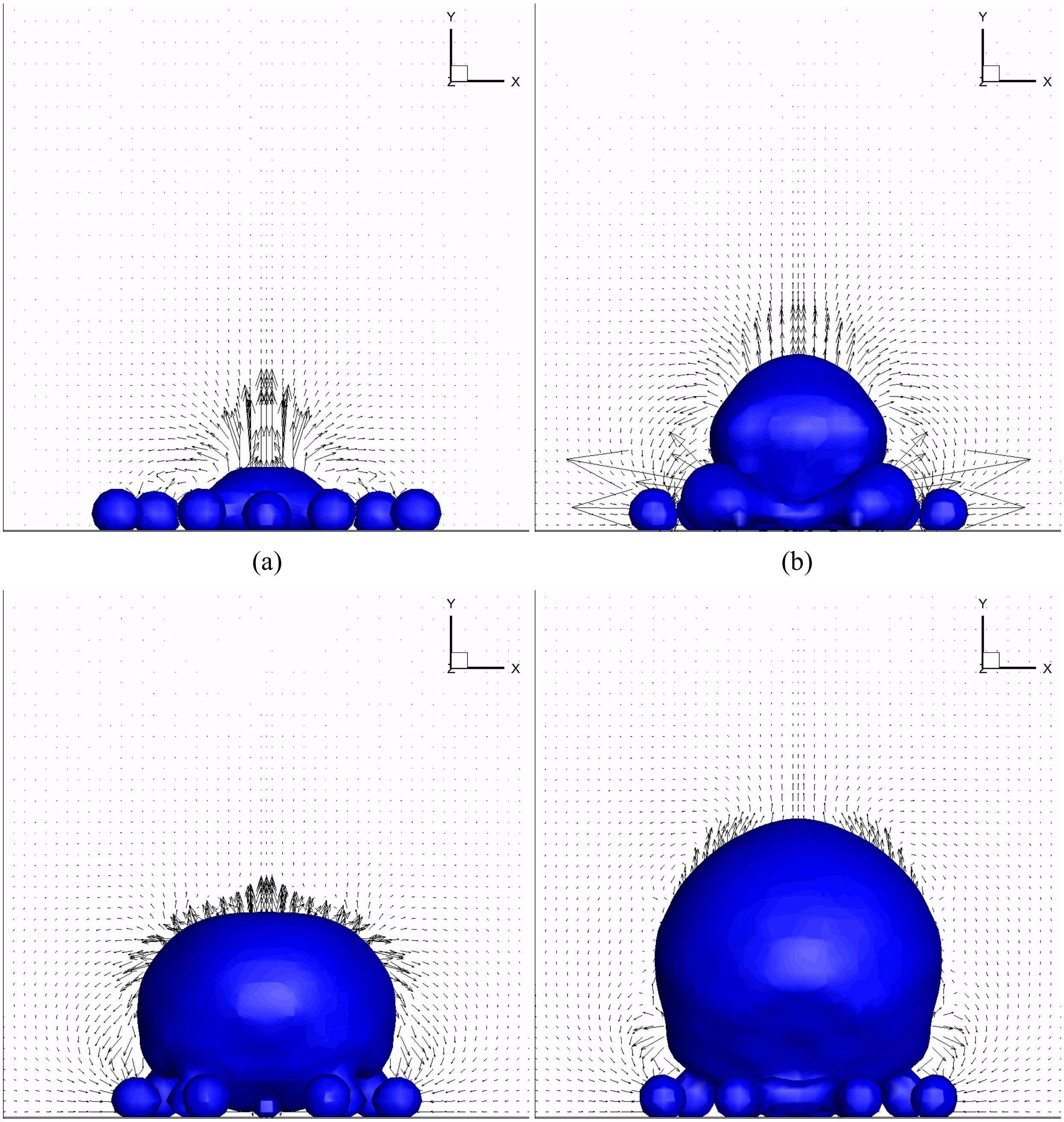

(a) (b) (c) (d)

Figure 5.51 Bubble shapes and flow fields from three dimensional simulation of nucleate boiling in microgravity. Total number of active cavities is 25, fluid is PFH with a contact angle of 30^o, $p = 1\ atm$, $\Delta T_w = 7\ ^oC$, and $\Delta T_{sub} = 0\ ^oC$. The times are (a) 0.2 s, (b) 2 s, (c) 5 s, and (d) 20 s.

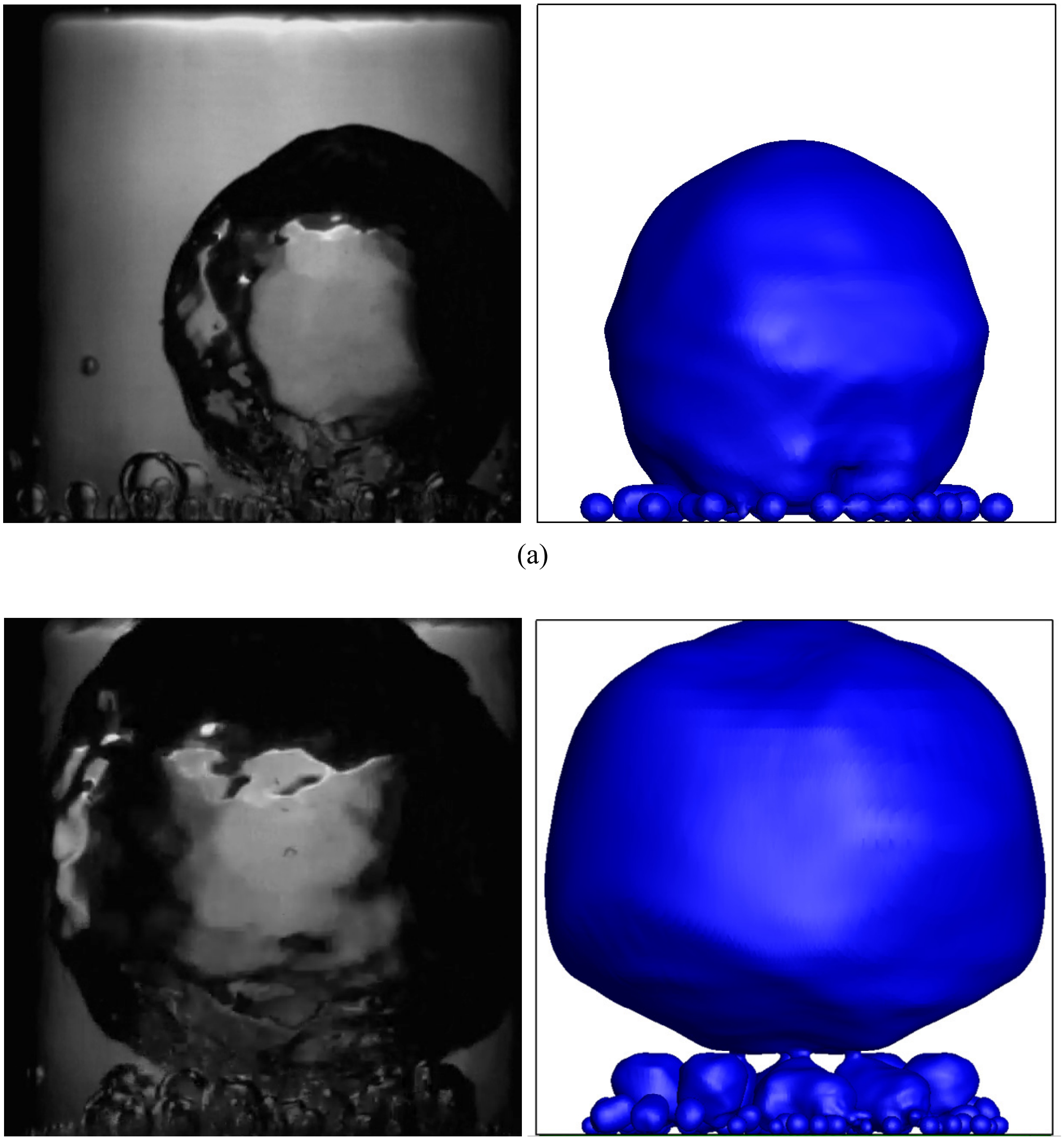

(a)

(b)

Figure 5.52 Comparison of steady state experimental and numerical vapor removal patterns at similar pressure (*p* ~ 140 *kPa*) and subcooling (ΔT_{sub} ~ 12 °*C*) but different wall superheats; (a) ΔT_w = 3.4 °*C*, and (b) ΔT_w = 5.2 °*C*.

5.4.2 Nucleate pool boiling heat transfer in microgravity conditions

The computer code developed to implement the procedure outlined in section 2.5 is serial. This means that a single central processing unit is used and therefore only one calculation can be performed at a time. If the number of grids is doubled, for example, the number of computations is also doubled and so is the computational time. In two dimensions, a general resolution for computational efficiency with acceptable accuracy was given by Son et al. (1998) as approximately 100 grid points per dimensionless unit of length. Consequently, two-dimensional numerical simulations are carried out with approximately 100 by 200 grid points. This results in a total of 20,000 grid points in the computational domain. The solution may generally take several days in the case of earth normal gravity where a quasi steady state is desired which requires many bubble growth cycles to achieve (refer back to Figure 5.14 for an example). The solution may take even longer (20-30%) due to iterations between solid and liquid if the problem of conjugate conduction is being solved. Iterations between the species conservation and energy equations when dissolved gas is present may further increase computational time by 20-30%.

In order to compare with the single bubble experiments performed on the ISS, only one cycle is required. Therefore, despite the greatly lengthened growth period and the presence of dissolved gas in the liquid, the overall computational time is reduced to two to three days.

However, for the nucleate boiling cases, it is not reasonable to assume axisymmetry. Instead, the governing equations given in section 2 must be solved in three-dimensional space. In order to maintain the same level of accuracy in three dimensions, the third dimension has to be discretized with the same mesh size. Therefore, the time required is 100 times longer, or several months for a single case. In addition to the unmanageable computational time, memory becomes a problem in three dimensions since the minimum grids required are 100 by 200 by 100—or 2,000,000 grid points. In order to overcome the limitations in computational time and memory management, the code must be rewritten so that a parallel computer architecture can be used to perform simultaneous computations in parallel. For the present study, however, the serial code is still used and the results of a coarse mesh are presented. The results shown in the following figures were all obtained using 66 by 130 by 66 grids (where the vertical coordinate is covered by the most grid points in a Cartesian coordinate system).

Figure 5.53 shows comparisons between the boiling curves obtained in the NPBX experiments and those predicted by numerical simulations. The simulations were carried out until a quasi steady state was reached at each superheat. Quasi steady state was defined as at least 10 elapsed seconds with constant wall heat flux and total vapor volume. At each superheat the number of cavities and the waiting time were calculated using Eqs. (65) and (66), respectively. The effect of dissolved gas was accounted for in these simulations by assuming equilibrium conditions exist between the liquid and vapor phases as explained previously. In this way, the species conservation equation is not solved and the saturation temperature is simply reduced by approximately 1 ^{o}C (dissolved mass fraction of gas was 2 x 10^{-5} in this case). For the first two cases shown, the exponents predicted by the simulations compare favorably with those obtained in the experiments. For the third case at highest pressure, the exponent is significantly higher in the simulation than in the experiment (2.68 compared to 1.15). The results from the simulation are consistent with the other two cases but appear to be surprisingly low in the experiment.

Despite the acceptable agreement in the boiling curve exponents, all heat fluxes are systematically under-predicted by the simulations. Figure 5.54 shows the result of a grid convergence test for interfacial heat transfer rate and wall heat flux. Grid refinement results in higher interfacial heat transfer rates and higher wall heat flux. The results shown in the boiling curves were obtained using a mesh size that is shown to not be fine enough for accurate capturing of temperature gradients. Therefore, the under-prediction in the heat flux is at least in part a direct result of the use of a coarse mesh.

Figure 5.55 shows a comparison between the experimental and numerical boiling curves obtained at microgravity and at Earth normal gravity for similar pressures and liquid subcoolings. Although at Earth normal gravity the simulation of nucleate pool boiling must also be performed in three dimensions, the heater size is much larger than the characteristic length. Therefore, the entire boiling chamber in the experiment does not need to be simulated as it does in microgravity and thus mesh limitations become less important when calculating temperature gradients. Although the prediction from numerical simulations is seen to be low even at Earth normal gravity, the maximum under prediction is 34% compared to over 300% at microgravity.

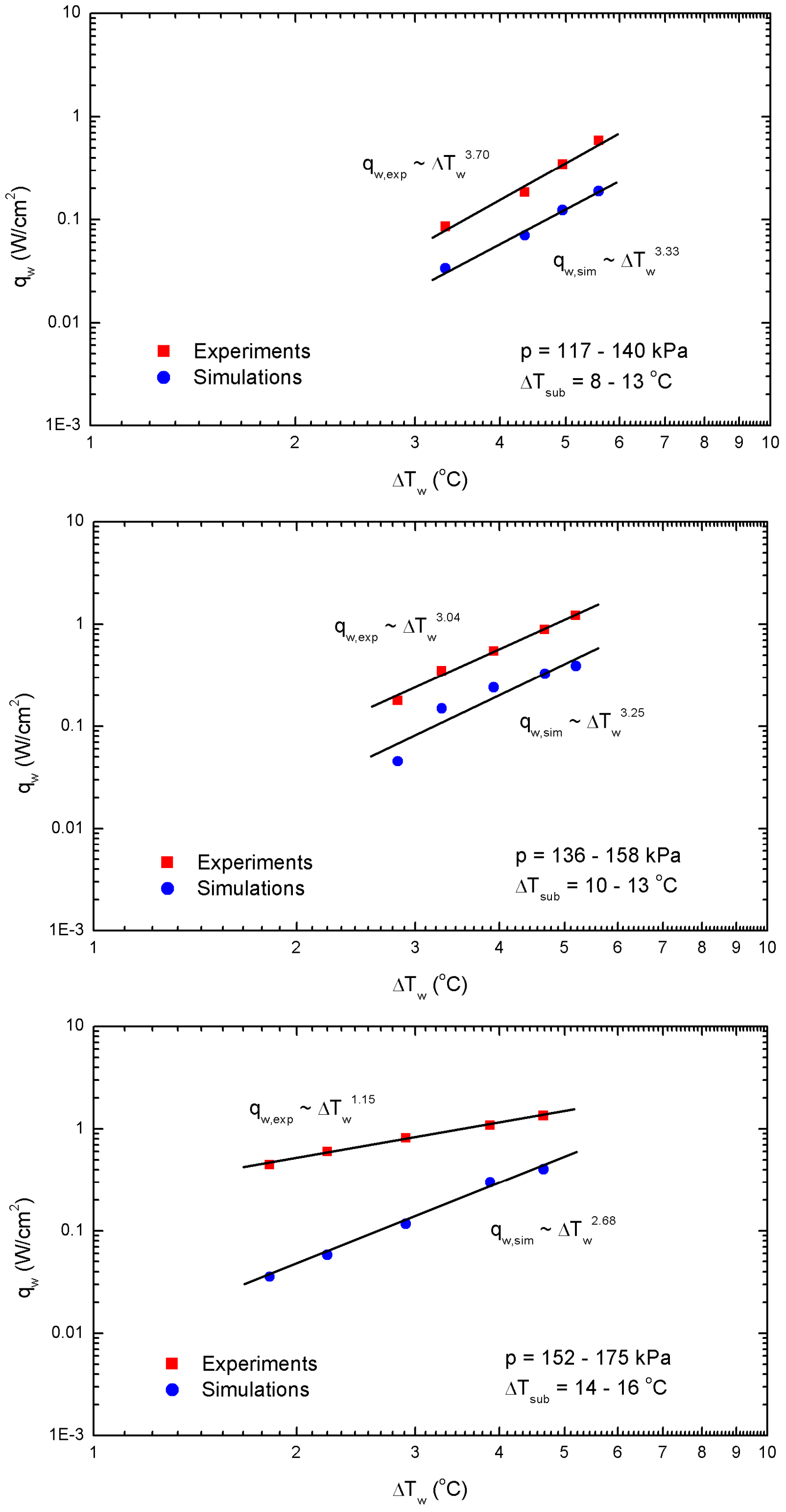

Figure 5.53 Boiling curves obtained from NPBX experiments and those predicted by numerical simulations at various pressures and liquid subcoolings.

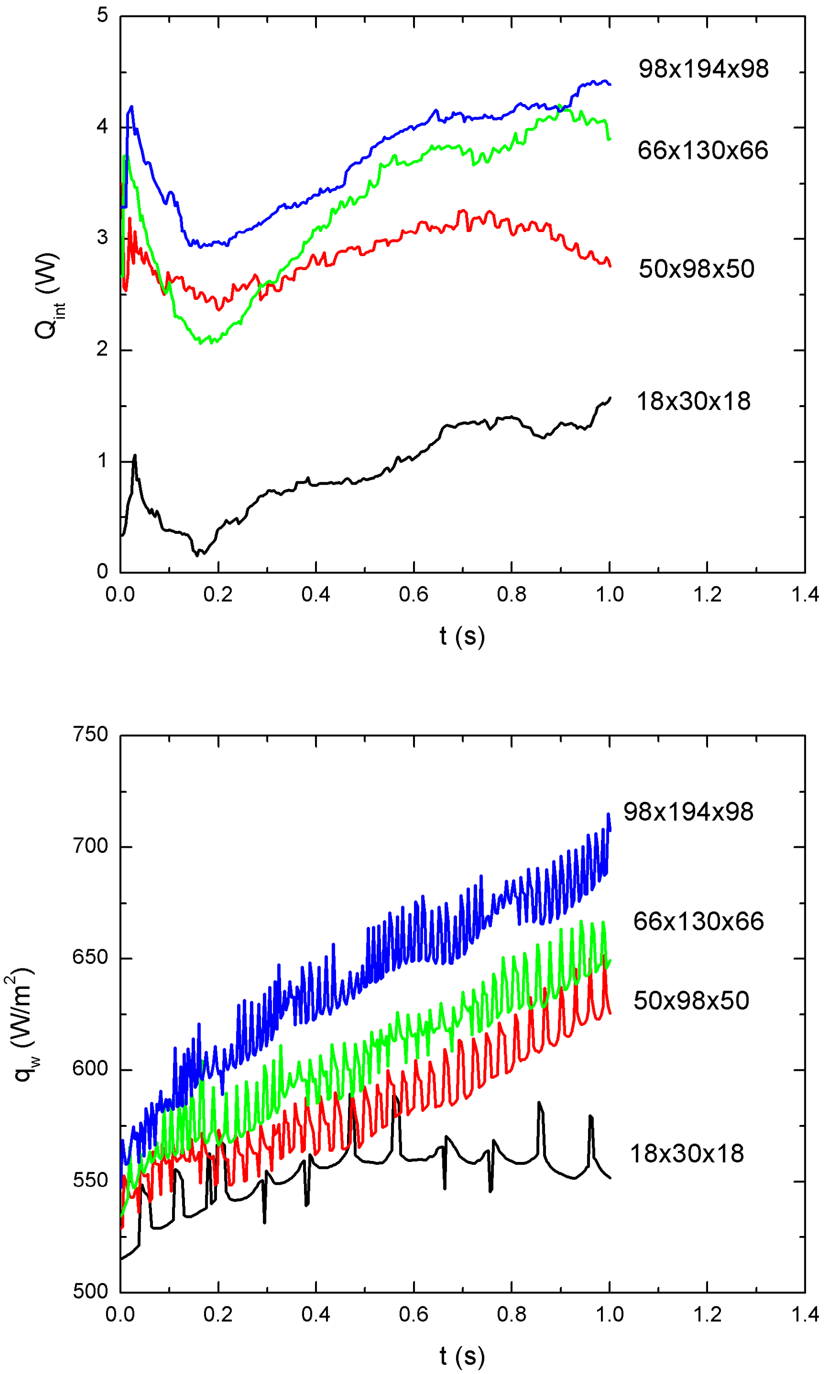

Figure 5.54 Effect of mesh size on numerical predictions of interface heat transfer rate and wall heat flux for three-dimensional simulations at microgravity.

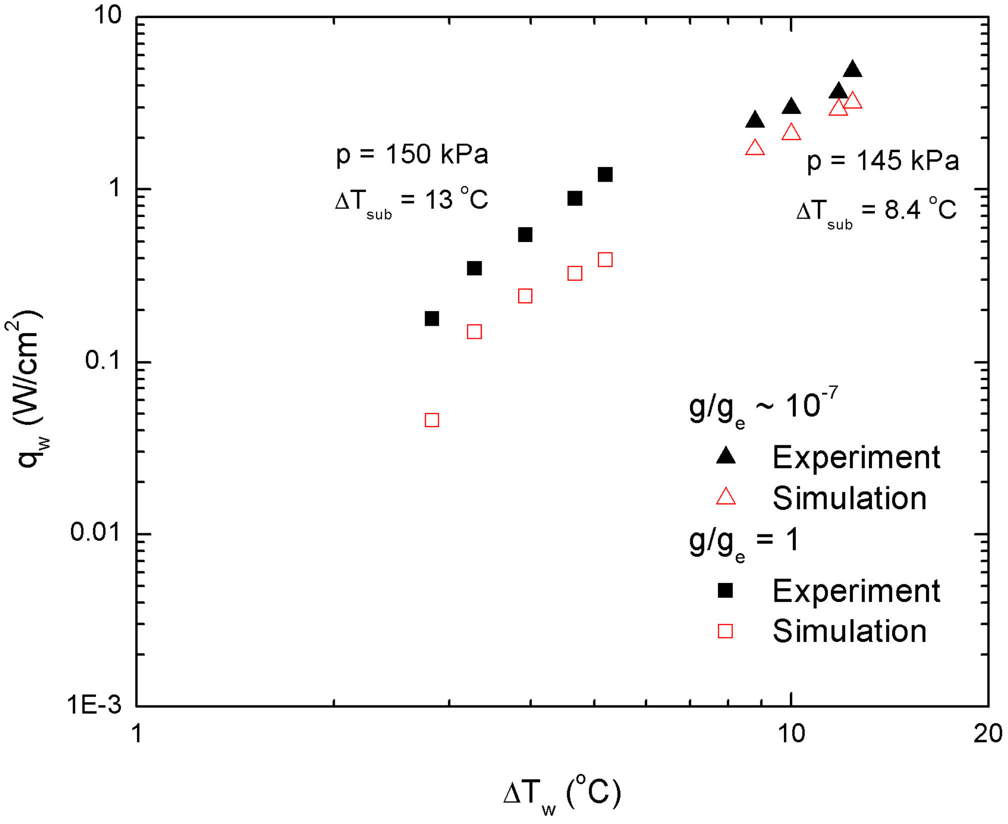

Figure 5.55 Comparison between experimental and numerical boiling curves obtained at microgravity and Earth normal gravity.

6 Conclusions

Complete numerical simulations of growing and departing bubbles on a horizontal surface have been carried out without any surface temperature or waiting time restrictions. The coupling of the solid thermal response to the simulation of nucleate pool boiling has provided for a more realistic description of the actual phenomena. Parametric studies have offered insight into the dependence of waiting time on wall superheat/heat flux, solid thickness, thermo-physical properties of the solid, and contact angle.

- The time dependent heat flux distribution along the surface of the wall is found to vary by up to four orders of magnitude during bubble growth. It is highest near the triple point where microlayer evaporation takes place, and lowest near the center of the bubble base where the surface is dry.
- Any given location on the solid surface that is traversed by the three-phase interline is seen to experience significant temperature fluctuations.
- The effects on bubble dynamics of applied heat flux, heater substrate properties and thickness, contact angle, and gravity level were determined. Waiting period dependencies were explained in detail by examining the thermal response of the heater substrate.
- Semi-empirical correlations for bubble release frequency which predict a simple inverse relationship between bubble departure diameter and bubble release frequency were shown to not to be applicable under low heat flux pool boiling.
- The dependence of boiling heat transfer coefficients on substrate properties, thickness, and contact angle were determined.

Calculations were also successfully carried out to simulate the process of a single bubble nucleating and growing on a flat plate under microgravity conditions and in the presence of dissolved gas in the liquid.

- Over the course of several hundred seconds of bubble growth and shrinkage, bubble sizes predicted by simulations were always within 20% of those obtained in the experiments.
- Wall heat transfer rates during bubble growth predicted by simulations were up to 40% lower than those obtained in the experiments. However, transient effects led to significant uncertainty in the calculation of heat losses in the experiments.
- Solution of the species conservation equation in the vapor region provided insight into local concentration of noncondensable gas in the bubble.
- It has been found that accumulation of noncondensable gas caused local drop in vapor pressure and reduced the effect of subcooling.
- Surface tension variation along the bubble interface was found to be small and the resulting capillary flow had only a second order effect on the overall flow field.
- Numerical simulations predicted bubble departure diameters much larger than what the boiling chamber would allow for. Accordingly, no single bubbles departed from the boiling surface during the experiments.

Preliminary three-dimensional calculations were performed to predict vapor removal patterns and nucleate pool boiling heat transfer in microgravity.

- The simulations provided predictions for the vapor removal pattern under microgravity conditions that matched well with experimental observations.

- The functional dependence of nucleate pool boiling heat flux on wall superheat was predicted well by the simulations.
- However, nucleate pool boiling heat transfer rates were under predicted by a factor of up to three in part due to the inability of coarse grids to properly calculate temperature gradients.

7 References

1. Abe, Y., & Iwasaki, A. (1999). “Observation of vapor bubble of non-azeotropic binary mixture in microgravity with a two-wavelength interferometer.” In Proceedings of the Fifth ASME/JSME Joint Thermal Engineering Conference.
2. Aktinol, E., & Dhir, V. K. (2012). “Numerical simulation of nucleate boiling phenomenon coupled with thermal response of the solid.” Microgravity Science and Technology, 24(4), 255-265.
3. Basu, N., Warrier, G. R., & Dhir, V. K. (2002). “Onset of nucleate boiling and active nucleation site density during subcooled flow boiling.” Journal of heat transfer, 124(4), 717-728.
4. Basu, N., Warrier, G. R., & Dhir, V. K. (2005). “Wall heat flux partitioning during subcooled flow boiling: Part 1—model development.” Journal of Heat Transfer, 127(2), 131-140.
5. Carey V.P. (2008). “Liquid-Vapor Phase-Change Phenomena.” Taylor & Francis Group, New York, NY.
6. Cole, R., & Shulman, H. L. (1966). “Bubble growth rates at high Jakob numbers.” International Journal of Heat and Mass Transfer, 9(12), 1377-1390.
7. Cooper, M. G., & Lloyd, A. J. P. (1969). “The microlayer in nucleate pool boiling.” International Journal of Heat and Mass Transfer, 12(8), 895-913.
8. Dhir, V. K. (2006). “Mechanistic prediction of nucleate boiling heat transfer–achievable or a hopeless task?” Journal of Heat Transfer, 128(1), 1-12.
9. Dhir, V. K., Warrier, G. R., & Aktinol, E. (2013). “Numerical Simulation of Pool Boiling: A Review.” Journal of Heat Transfer, 135(6), 061502.

10. Dhir, V. K., Warrier, G. R., Aktinol, E., Chao, D., Eggers, J., Sheredy, W., & Booth, W. (2012). “Nucleate Pool Boiling Experiments (NPBX) on the International Space Station.” Microgravity Science and Technology, 24(5), 307-325.
11. Douglas, J., & Gunn, J. E. (1964). “A general formulation of alternating direction methods.” Numerische Mathematik, 6(1), 428-453.
12. Fedkiw, R. P., Aslam, T., Merriman, B., & Osher, S. (1999). “A non-oscillatory Eulerian approach to interfaces in multimaterial flows (the ghost fluid method).” Journal of Computational Physics, 152(2), 457-492.
13. Forster, H. K., & Zuber, N. (1954). “Growth of a vapor bubble in a superheated liquid.” Journal of Applied Physics, 25(4), 474-478.
14. Fritz, W. (1935). “Maximum volume of vapor bubbles.” Physik Zeitschr, 36(11), 379-384.
15. Ghiaasiaan, S.M. (2008). “Two-Phase Flow, Boiling, and Condensation in Conventional and Miniature Systems.” Cambridge University Press, New York, NY.
16. Guo, Z., & El-Genk, M. S. (1994). “Liquid microlayer evaporation during nucleate boiling on the surface of a flat composite wall.” International Journal of Heat and Mass Transfer, 37(11), 1641-1655.
17. Han, C. Y., & Griffith, P. (1965). “The Mechanism of Heat Transfer in Nucleate Pool Boiling. Part I. Bubble Initiation, Growth, and Departure." International Journal of Heat and Mass Transfer, 8, 887-904.
18. Howell, J. R., & Siegel, R. (1967). “Activation, growth, and detachment of boiling bubbles in water from artificial nucleation sites of known geometry and size.” National Aeronautics and Space Administration.

19. Hsu, Y. Y., & Graham, R. W. (1961). “An analytical and experimental study of the thermal boundary layer and ebullition cycle in nucleate boiling.” National Aeronautics and Space Administration.
20. Hsu, Y. Y. (1962). “On the size range of active nucleation cavities on a heating surface.” Journal of Heat Transfer, 84(3), 207-213.
21. Hsu Y.Y., Graham R.W. (1986). “Transport Processes in Boiling and Two-Phase Systems.” American Nuclear Society, La Grange Park, IL.
22. Judd, R. L., & Chopra, A. (1993). “Interaction of the nucleation processes occurring at adjacent nucleation sites.” Journal of Heat Transfer, 115(4), 955-962.
23. Kannengieser, O., Colin, C., & Bergez, W. (2011). “Influence of gravity on pool boiling on a flat plate: Results of parabolic flights and ground experiments.” Experimental Thermal and Fluid Science, 35(5), 788-796.
24. Kim, J., Benton, J. F., & Wisniewski, D. (2002). “Pool boiling heat transfer on small heaters: effect of gravity and subcooling.” International Journal of Heat and Mass Transfer, 45(19), 3919-3932.
25. Kobus, C. J., & Wedekind, G. L. (2001). “An experimental investigation into natural convection heat transfer from horizontal isothermal circular disks.” International journal of heat and mass transfer, 44(17), 3381-3384.
26. Kunkelmann, C., & Stephan, P. (2010). “Numerical simulation of the transient heat transfer during nucleate boiling of refrigerant HFE-7100.” International Journal of Refrigeration, 33(7), 1221-1228.
27. Lay, J. H., & Dhir, V. K. (1995). “Shape of a vapor stem during nucleate boiling of saturated liquids.” Journal of Heat Transfer, 117(2), 394-401.

28. Lee, H. S., Jr, H. M., & Chiaramonte, F. (1997). “Pool boiling curve in microgravity.” Journal of Thermophysics and Heat Transfer, 11(2), 216-222.
29. Magrini, U., & Nannei, E. (1975). “On the influence of the thickness and thermal properties of heating walls on the heat transfer coefficients in nucleate pool boiling.” Journal of Heat Transfer, 97(2), 173-178.
30. Mann, M., Stephan, K., & Stephan, P. (2000). “Influence of heat conduction in the wall on nucleate boiling heat transfer.” International journal of heat and mass transfer, 43(12), 2193-2203.
31. McAdams, W. H. (1954). “Heat Transmission.” McGraw-Hill, New York, NY.
32. Mikic, B. B., & Rohsenow, W. M. (1969). “Bubble growth rates in non-uniform temperature field.” Progress in Heat and Mass Transfer, 2, 283-292.
33. Mikic, B. B., Rohsenow, W. M., & Griffith, P. (1970). “On bubble growth rates.” International Journal of Heat and Mass Transfer, 13(4), 657-666.
34. Mills, A.F. (1998). “Heat Transfer.” Prentice Hall, Upper Saddle River, NJ.
35. Minkowycz, W. J., & Sparrow, E. M. (1966). “Condensation heat transfer in the presence of noncondensables, interfacial resistance, superheating, variable properties, and diffusion.” International Journal of Heat and Mass Transfer, 9(10), 1125-1144.
36. Moghaddam, S., & Kiger, K. (2009). “Physical mechanisms of heat transfer during single bubble nucleate boiling of FC-72 under saturation conditions-I. Experimental investigation.” International Journal of Heat and Mass Transfer, 52(5), 1284-1294.
37. Moore, F. D., & Mesler, R. B. (1961). “The measurement of rapid surface temperature fluctuations during nucleate boiling of water.” AIChE Journal, 7(4), 620-624.

38. Mukherjee, A., & Dhir, V. K. (2004). “Study of lateral merger of vapor bubbles during nucleate pool boiling.” Journal of Heat Transfer, 126(6), 1023-1039.
39. Nam, Y., Aktinol, E., Dhir, V. K., & Ju, Y. S. (2011). “Single bubble dynamics on a superhydrophilic surface with artificial nucleation sites.” International Journal of Heat and Mass Transfer, 54(7), 1572-1577.
40. Nam, Y., Wu, J., Warrier, G., & Ju, Y. S. (2009). “Experimental and numerical study of single bubble dynamics on a hydrophobic surface.” Journal of Heat Transfer, 131(12), 121004.
41. Nukiyama, S. (1934). “The maximum and minimum values of the heat Q transmitted from metal to boiling water under atmospheric pressure.” Int. J. Heat Mass Transfer, 9, 1419-1433.
42. Ohta, H., Kawasaki, K., Okada, S., Azuma, H., Yoda, S., & Nakamura, T. (1999). “On the heat transfer mechanisms in microgravity nucleate boiling.” Advances in Space Research, 24(10), 1325-1330.
43. Oka, T., Abe, Y., Mori, Y. H., & Nagashima, A. (1995). “Pool boiling of n-pentane, CFC-113, and water under reduced gravity: parabolic flight experiments with a transparent heater.” Journal of heat transfer, 117(2), 408-417.
44. Othmer, D. F. (1929). “The condensation of steam.” Industrial & Engineering Chemistry, 21(6), 576-583.
45. Plesset, M. S., & Zwick, S. A. (2004). “The growth of vapor bubbles in superheated liquids.” Journal of Applied Physics, 25(4), 493-500.

46. Qiu, D. M., Dhir V. K., Hasan M. M., & Chao D. (2000). “Single Bubble Dynamics during Nucleate Boiling under Low Gravity Conditions.” Microgravity Fluid Physics and Heat Transfer, 62-71.
47. Rogers, T. F., & Mesler, R. B. (1964). “An experimental study of surface cooling by bubbles during nucleate boiling of water.” AIChE Journal, 10(5), 656-660.
48. Shoji, M., & Takagi, Y. (2001). “Bubbling features from a single artificial cavity.” International journal of heat and mass transfer, 44(14), 2763-2776.
49. Son, G., Dhir, V. K., & Ramanujapu, N. (1999). “Dynamics and heat transfer associated with a single bubble during nucleate boiling on a horizontal surface.” Journal of Heat Transfer, 121(3), 623-631.
50. Son, G., & Dhir, V. K. (1997). “Numerical simulation of saturated film boiling on a horizontal surface.” Journal of heat transfer, 119(3), 525-533.
51. Son, G., & Dhir, V. K. (1998). “Numerical simulation of film boiling near critical pressures with a level set method.” Journal of Heat Transfer, 120(1), 183-192.
52. Son, G., & Dhir, V. K. (2007). “A level set method for analysis of film boiling on an immersed solid surface.” Numerical Heat Transfer, Part B: Fundamentals, 52(2), 153-177.
53. Sparrow, E. M., Goldstein, R. J., & Jonsson, V. K. (1964). “Thermal instability in a horizontal fluid layer: effect of boundary conditions and non-linear temperature profile.” Journal of Fluid Mechanics, 18(04), 513-528.
54. Sparrow, E. M., Husar, R. B., & Goldstein, R. J. (1970). “Observations and other characteristics of thermals.” Journal of Fluid Mechanics, 41(04), 793-800.

55. Sparrow, E. M., & Lin, S. H. (1964). “Condensation heat transfer in the presence of a noncondensable gas.” Journal of Heat Transfer, 86(3), 430-436.
56. Stephan, K., & Abdelsalam, M. (1980). “Heat-transfer correlations for natural convection boiling.” International Journal of Heat and Mass Transfer, 23(1), 73-87.
57. Straub, J. (2001). “Boiling heat transfer and bubble dynamics in microgravity.” Advances in Heat Transfer, 35, 57-172.
58. Straub, J. (2002). “Origin and Effect of Thermocapillary Convection in Subcooled Boiling.” Annals of the New York Academy of Sciences, 974(1), 348-363.
59. Sultan, M., & Judd, R. L. (1983). “Interaction of the nucleation phenomena at adjacent sites in nucleate boiling.” Journal of Heat Transfer, 105(1), 3-9.
60. Sussman, M., Smereka, P., & Osher, S. (1994). “A level set approach for computing solutions to incompressible two-phase flow.” Journal of Computational physics, 114(1), 146-159.
61. Van Stralen, S. J. D., Cole, R., Sluyter, W. M., & Sohal, M. S. (1975). “Bubble growth rates in nucleate boiling of water at subatmospheric pressures.” International Journal of Heat and Mass Transfer, 18(5), 655-669.
62. Wang, C. H., & Dhir, V. K. (1993). “Effect of surface wettability on active nucleation site density during pool boiling of water on a vertical surface.” Journal of Heat Transfer, 115(3), 659-669.
63. Wang, C. H., & Dhir, V. K. (1993). “On the gas entrapment and nucleation site density during pool boiling of saturated water.” Journal of Heat Transfer, 115(3), 670-679.

64. Wayner Jr, P. C. (1992). "Evaporation and stress in the contact line region." In Proceedings of the Engineering Fundamentals Conference on Pool and Flow Boiling (pp. 251-256).
65. Wu, J., & Dhir, V. K. (2011). "Numerical simulation of dynamics and heat transfer associated with a single bubble in subcooled boiling and in the presence of noncondensables." Journal of Heat Transfer, 133(4), 041502.
66. Yoon, H. Y., Koshizuka, S., & Oka, Y. (2001). "Direct calculation of bubble growth, departure, and rise in nucleate pool boiling." International Journal of Multiphase Flow, 27(2), 277-298.
67. Zeng, H., & Zhu, J. (2002). "An efficient parallel ADI algorithm for solving 3-D convection diffusion equations with Neumann boundary conditions." International Conference on Parallel Processing Workshops, 320-326.
68. Zhao, J. F., Wan, S. X., Liu, G., Yan, N., & Hu, W. R. (2009). "Subcooled pool boiling on thin wire in microgravity." Acta Astronautica, 64(2), 188-194.
69. Zuber, N. (1963). "Nucleate boiling. The region of isolated bubbles and the similarity with natural convection." International Journal of Heat and Mass Transfer, 6(1), 53-78.